Distribution Categories:
Magnetic Fusion Energy (UC-20
plus UC-20a through -20g

ANL/FPP-79-3

master

ARGONNE NATIONAL LABORATORY
9700 South Cass Avenue
Argonne, Illinois 60439

FUSION POWER PROGRAM
BIANNUAL PROGRESS REPORT

April—September 1979

Charles C. Baker, Director

Mohamed A. Abdou, Associate Director

February 1980

FOREWORD

This bi-annual report describes fusion-related activities in research, development and reactor design, analysis and safety conducted within the Fusion Power Program and within other DOE-funded programs at Argonne National Laboratory.

The last seven quarterly reports issued were:

ANL/FPP-77-4	July-September 1977
ANL/FPP-77-7	October-December 1977
ANL/FPP-78-1	January-March 1978
ANL/FPP-78-2	April-June 1978
ANL/FPP-78-3	July-September 1978
ANL/FPP-78-4	October-December 1978
ANL/FPP-79-2	January-March 1979

ABSTRACT

This bi-annual report summarizes the Argonne National Laboratory work performed for the Office of Fusion Energy during the April-September 1979 quarter in the following research and development areas: materials; energy storage and transfer; tritium containment, recovery and control; advanced reactor design; atomic data; reactor safety; fusion-fission hybrid systems; alternate applications of fusion energy; and other work related to fusion power.

TABLE OF CONTENTS

TABLE OF CONTENTS (cont'd.)

TABLE OF CONTENTS (cont'd.)

LIST OF FIGURES

LIST OF FIGURES (cont'd.)

LIST OF FIGURES (cont'd.)

LIST OF FIGURES (cont'd.)

LIST OF FIGURES (cont'd.)

LIST OF TABLES

LIST OF TABLES (cont'd.)

1.0 FUSION REACTOR MATERIALS

1.1 Alloy Development for Irradiation Performance

1.1.1 Effects of Irradiation on Fusion Reactor Materials

1.1.1.1 Radiation Induced Segregation and Irradiation Creep

V. K. Sethi, F. Schulz, F. V. Nolfi, Jr. and A. P. L. Turner, Materials Science Division

During measurements of irradiation creep on solution annealed and aged Type 316 stainless steel (MFE Ht. #15813), it was found that displacement-producing radiation consistently caused the sample to creep against the applied stress[1]. This anomalous behavior is attributed to either modulus changes caused by irradiation-enhanced precipitation in the metastable solution annealed Type 316 stainless steel, or dimensional changes caused by precipitation and/or swelling. In addition, this alloy is known to exhibit considerable radiation-induced segregation (RIS) of both major and minor alloying elements during heavy-ion irradiation[2].

This report deals with experiments designed to determine the effect of RIS on creep deformation in a model system (Ni - 4 at. % Si), with a composition such that no second phase exists in the absence of irradiation. The alloy was chosen because it simulates the solution hardening present in stainless steel and because RIS and precipitation do occur in the alloy.

High purity nickel and nickel - 4 at. % silicon alloy were processed into *10-cm-long, 0.075-cm-diameter wires.* The nickel wires were annealed at 700°C for ten minutes, and the nickel - 4 at. % silicon wires were annealed at 815°C for two hours in an inert environment. The heat treatments were selected to give comparable grain sizes in the two materials. The creep specimens were fabricated from these wires by electropolishing a reduced section (~0.013 cm diameter and 0.65 cm long). A typical specimen fabricated in this fashion contains at least ten grains across the diameter.

Creep measurements were made in the Torsional Creep Apparatus[3] at 350°C. A 21-MeV deuteron beam was used for irradiation experiments at a dose rate of $\sim 2 \times 10^{-6}$ dpa $\cdot$ s^{-1}. Preirradiation and postirradiation measurements were made to assess whether irradiation produced significant changes in the structure of the material.

The preirradiation and postirradiation data for the two materials are shown in Figs. 1-1 through 1-5. The main features of the data are:

1. Comparison of the data illustrated in Fig. 1-1 reveals that in pure nickel, for the small doses involved in these tests (~0.075 dpa), there are no large-scale, irradiation-induced microstructural changes.

2. Figures 1-2 and 1-3 show the preirradiation and postirradiation deformation behavior of nickel - 4 at. % silicon alloy. The alloy exhibits considerable irradiation hardening. Since no such hardening is observed in pure nickel, it is likely that the effect is associated with RIS of silicon to internal immobile sinks, the hardening mechanism being precipitate decorated loop intersection.

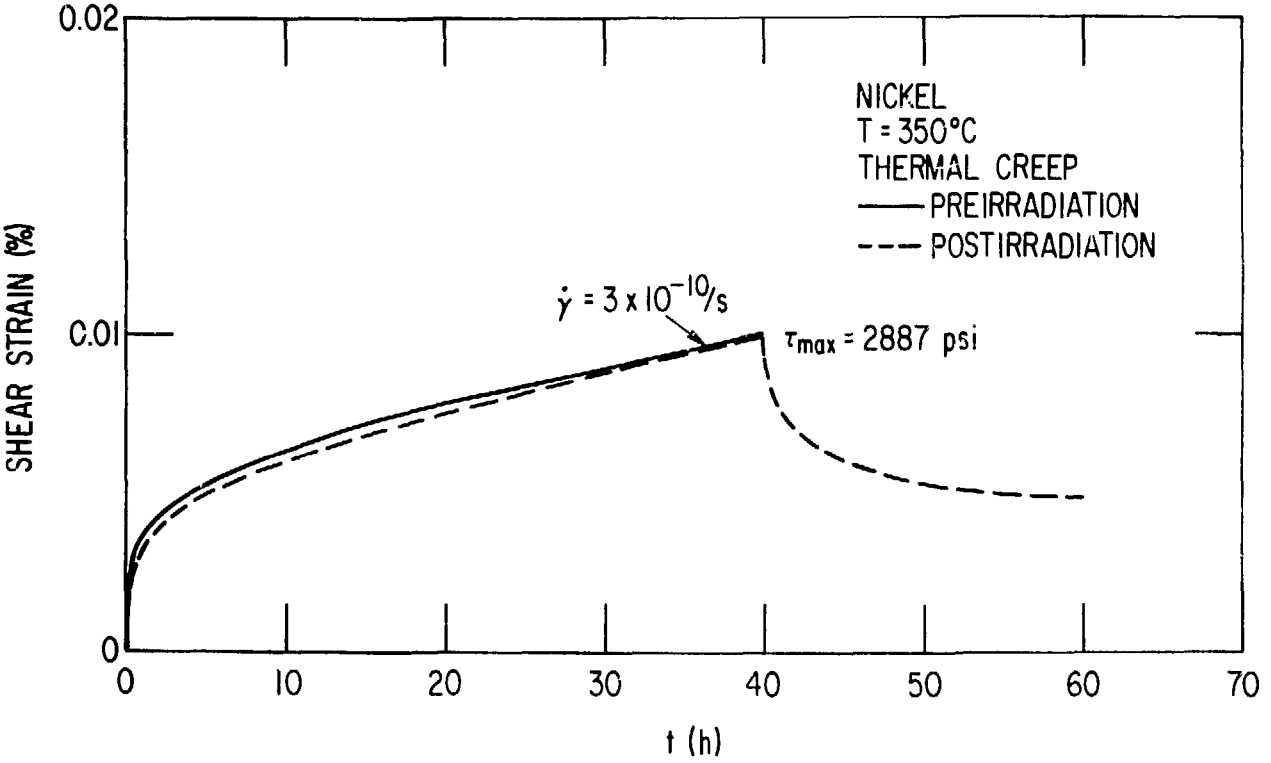

Figure 1-1. Comparison of the strain-time behavior of pure nickel in pre- and post-irradiation conditions.

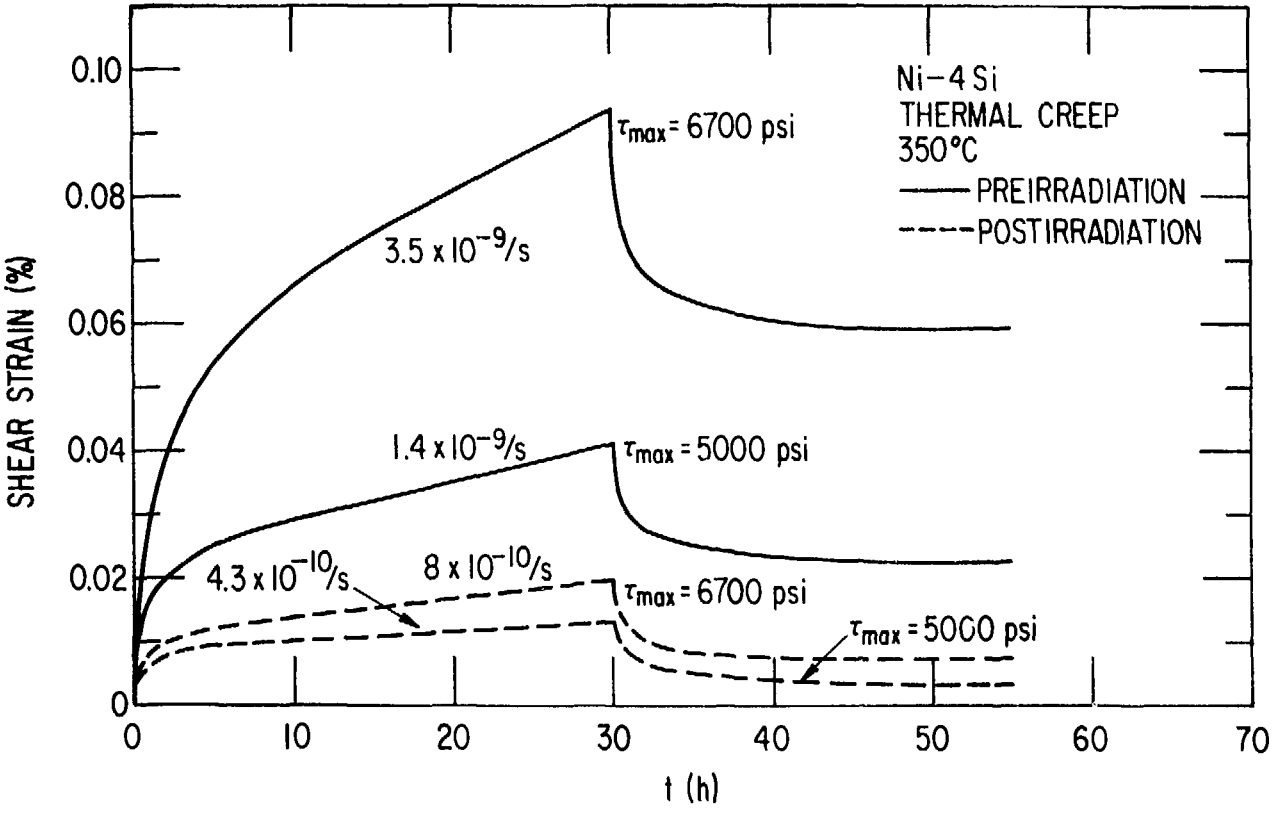

Figure 1-2. Strain-time behavior of nickel - 4 at. % silicon alloy in preirradiation and postirradiation conditions at 6700 and 5000 psi.

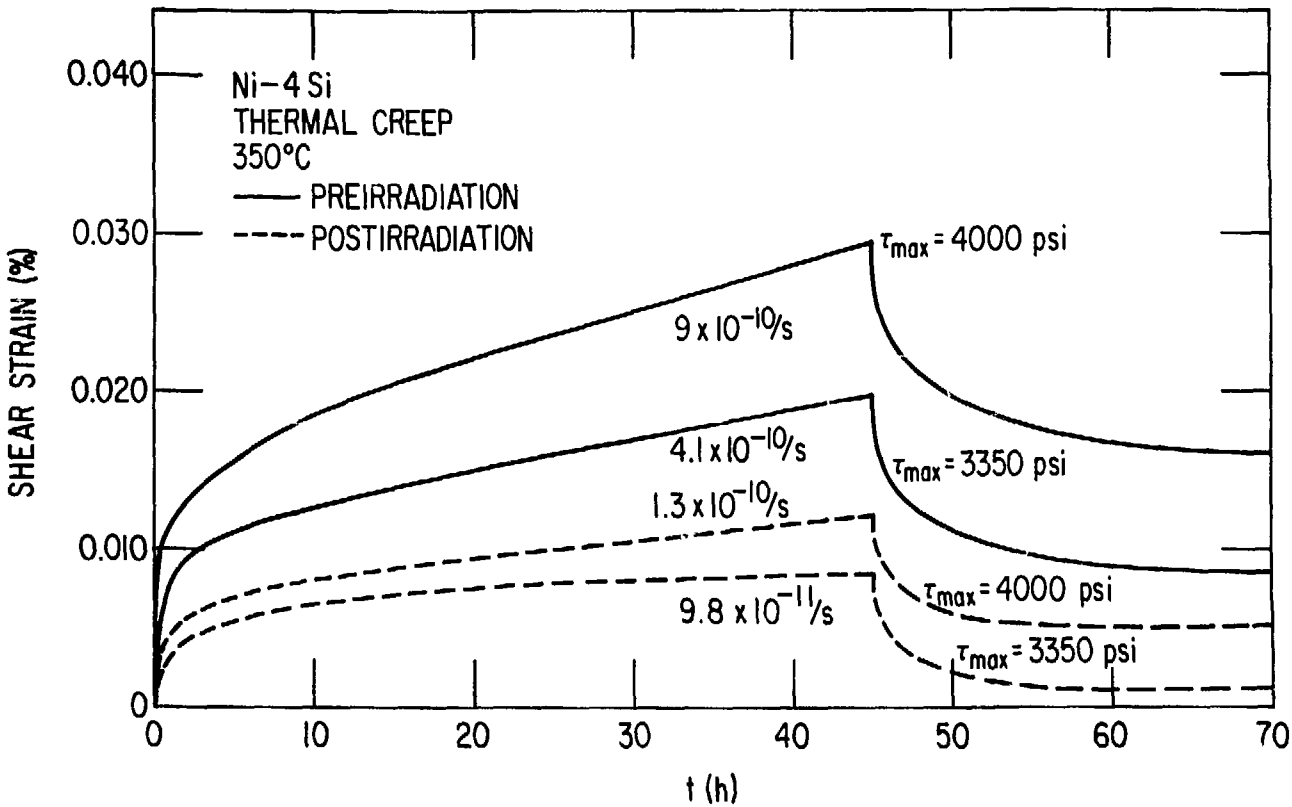

Figure 1-3. Strain-time behavior of nickel - 4 at. % silicon alloy in preirradiation and postirradiation conditions at 4000 and 3350 psi.

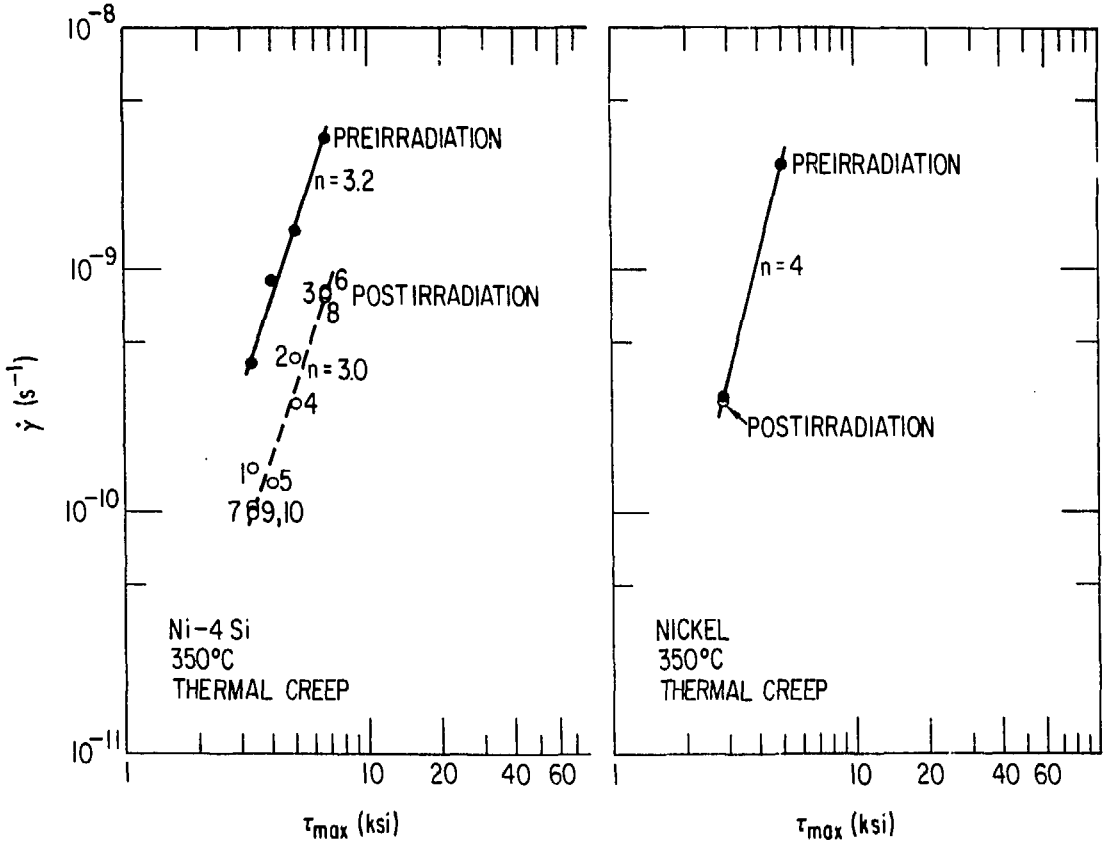

Figure 1-4. Stress dependence of the steady state creep rates for nickel and nickel - 4 at. % silicon alloy at 350°C in preirradiation and postirradiation conditions. Irradiation conditions - 21 MeV deuterons, 2 x 10^{-6} dpa·s^{-1}, 0.075 dpa at 350°C.

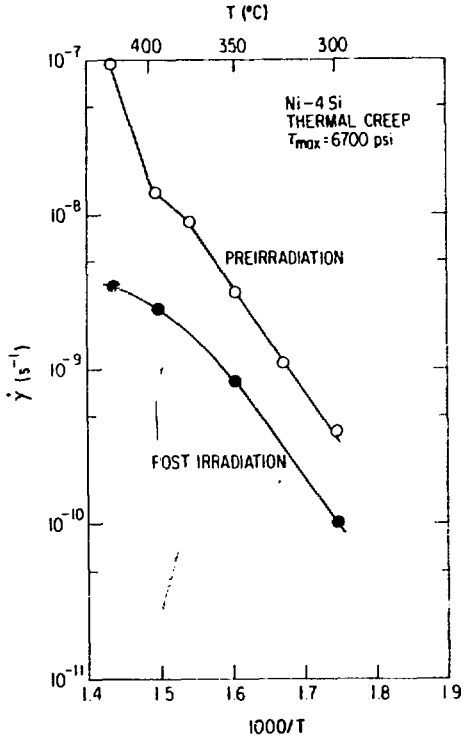

Figure 1-5. The temperature dependence of the steady state creep-rate of nickel - 4 at. % silicon alloy at 6700 psi maximum shear stress in preirradiation and postirradiation conditions. Irradiation conditions - 21-MeV deuterons, 2×10^{-6} dpa $\cdot$ s^{-1}, 0.075 dpa at 350°C.

3. The stress and temperature dependence of the creep-rate of nickel - 4 at. % silicon for preirradiation and postirradiation conditions are shown in Figs. 1-4 and 1-5, respectively. The stress exponent for creep of the alloy is essentially unchanged and, similarly, the activation energy is unaffected by irradiation at least at lower temperatures. This observation suggests that the thermally activated process is the same for preirradiation and postirradiation conditions below about 400°C. Thus, the irradiation-induced hardening is athermal in nature.

Figure 1-6 shows the strain-time curves for nickel and nickel - 4 at. % silicon during 21-MeV deuteron irradiation. As illustrated by the accompanying thermal creep curves, the stress levels for the two materials were chosen so as to approximately match the preirradiation thermal creep behavior. Some of the important features of the data are:

1. Irradiation enhancement of the creep-rate of pure nickel was by a factor $\sim$13, while the enhancement for nickel - 4 at. % silicon was $\sim$5 for the irradiated alloy, and $\sim$20 after the alloy was irradiated to $\sim$0.075 dpa at a dose rate of 2×10^{-6} dpa $\cdot$ s^{-1}. Thus, irradiation hardening reduced the thermal creep rate of the alloy by a factor of $\sim$4.

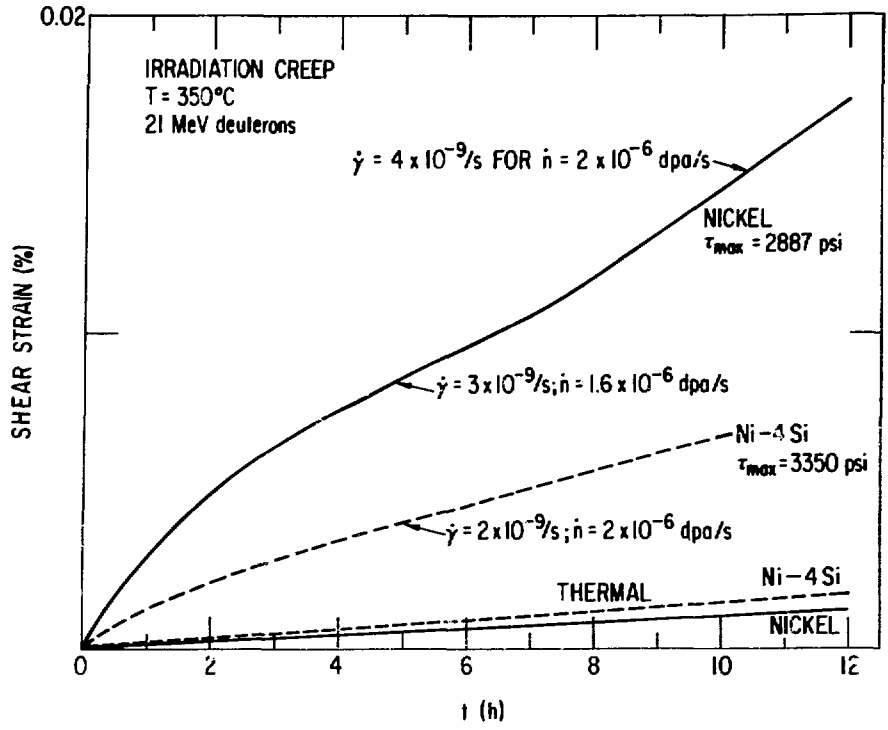

Figure 1-6. Irradiation enhanced creep deformation in pure nickel and nickel - 4 at. % silicon alloy during 21-MeV deuteron irradiation at 350°C at a dose rate of 2×10^{-6} dpa $\cdot$ s^{-1}.

2. Nickel appears to show a linear flux dependence, although this has to be explored further.

1.1.1.2 Temperature Dependence of Swelling in Single- and Dual-Ion Irradiated Stainless Steel

G. Ayrault, H. A. Hoff, F. V. Nolfi, Jr. and A. P. L. Turner, Materials Science Division

A major question in the irradiation response of candidate fusion reactor structural materials is the influence of concurrent displacement damage and helium production. Dual-ion irradiation, using heavy-ions for damage production and helium ions to simulate gas production by transmutation events provides a means of investigating such effects in the absence of a high energy neutron source.

This report presents preliminary results on the temperature dependence of swelling in single- and dual-ion irradiated 316 stainless steel. Dose and helium injection rate dependences of swelling will be determined in future stages of the program.

Irradiation Conditions - Type 316 stainless steel samples from the MFE heat were 50% cold-worked, then solution annealed at 1050°C for 0.5 h and aged at 800°C for 10 h. One set of samples was simultaneously irradiated with 3.0 MeV Ni^+ and 0.87 MeV degraded $^3He^+$ in the ANL Dual-Ion Irradiation Facility; the helium injection rate was 15:1 appm He:dpa. A second set of samples was preinjected at room temperature with 5 appm ^3He, and single-ion irradiated with 3.0 MeV Ni^+. For both sets the dose level was 12 dpa. The nominal irradiation temperatures were 550, 600, 625, 650 and 700°C; surface temperatures of all samples were measured with an infrared pyrometer during irradiation. After irradiation, the samples were electrochemically sectioned to a depth of 4500Å (peak damage is at 5500Å), and backthinned for TEM inspection.

Precipitates - Most of the irradiated samples contained both cavities and intragranular precipitates, which were not present in unirradiated control samples with the same thermal history. In addition, the cavities were coated with precipitates in all samples where cavities were found; examples of this are shown in Fig. 1-7.

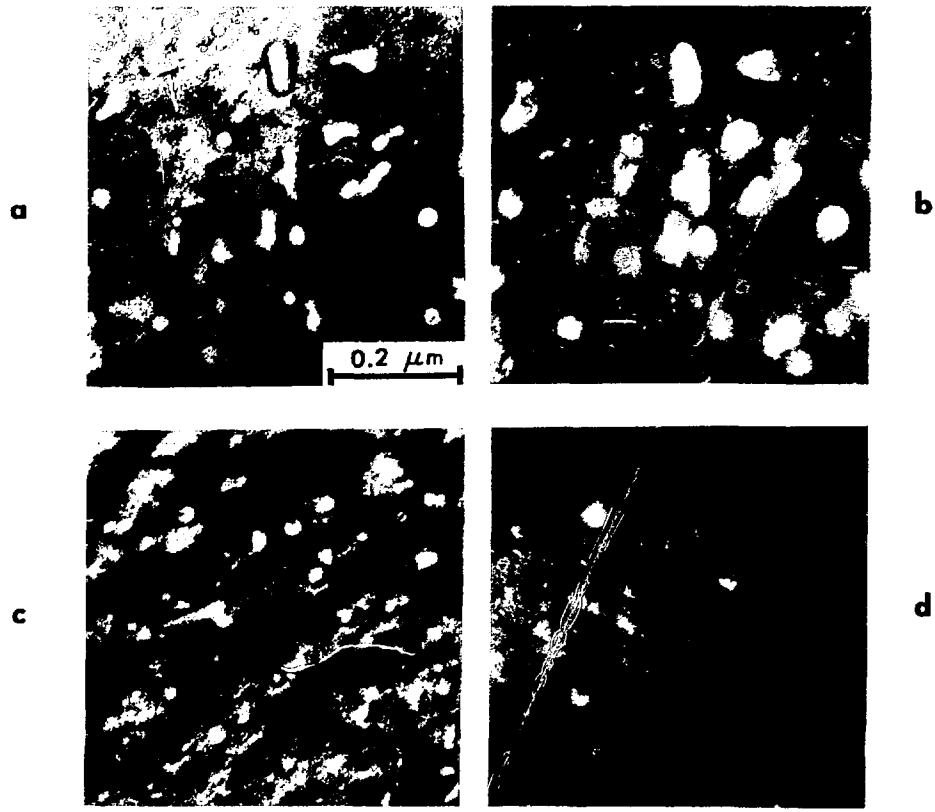

Figure 1-7. Bright-field dark-field pairs showing precipitate-coated cavities in preinjected single-ion and dual-ion irradiated 316 stainless steel (dose = 12 dpa, dose rate = 3 x 10^{-3} dpa•s^{-1}) (a) 603°C dual-ion, (b) dark-field of same region as (a), (c) 650°C preinjected single-ion, (d) dark-field of same region as (c).

Swelling in Dual-Ion Irradiated Samples - For dual-ion irradiation in the temperature range 550 to 650°C, a bimodal cavity-size distribution was found, Fig. 1-8a-e; at 700°C, only small cavities were observed, Fig. 1-8f. Large cavities were usually associated with the intragranular precipitates, while the small cavities were found on both precipitates and dislocations.

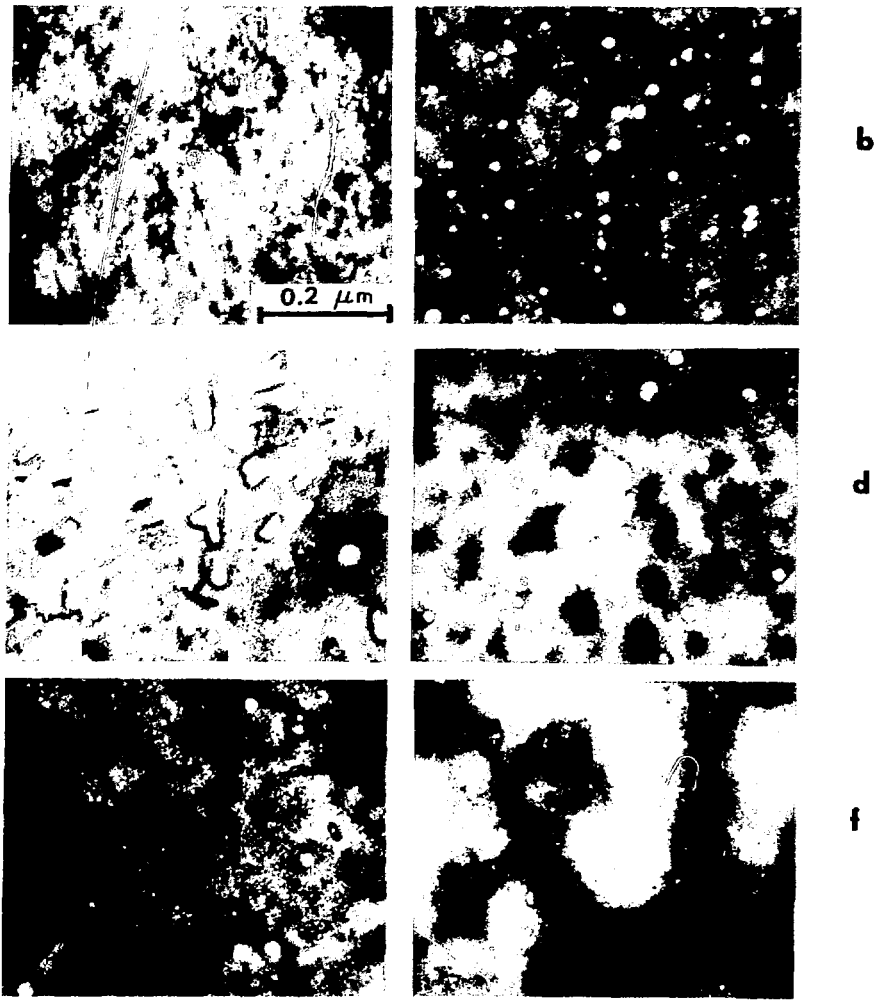

Figure 1-8. Absorption contrast micrographs of dual-ion irradiated 316 stainless steel (dose = 12 dpa, dose rate = 3 x 10^{-3} dpa·s^{-1}, helium injection rate = 15:1 appm He:dpa). (a) 540°C, (b) 595°C, (c) 603°C, (d) 633°C, (e) 650°C, and (f) 700°C.

Void number densities, mean void size and void volume were determined from the TEM micrographs. The data are presented in Figs. 1-9, 1-10, and 1-11. Each data point is based on observations in at least three different regions of the sample; the error bars reflect variations between these regions. In numerical data analyses, the small and large cavities in the bimodal distribution were treated separately, and the cavity number density and size are plotted separately in Figs. 1-9 and 1-10. For void volume, Fig. 1-11, the two contributions have been summed, but when large cavities are present, they account for nearly all of the volume.

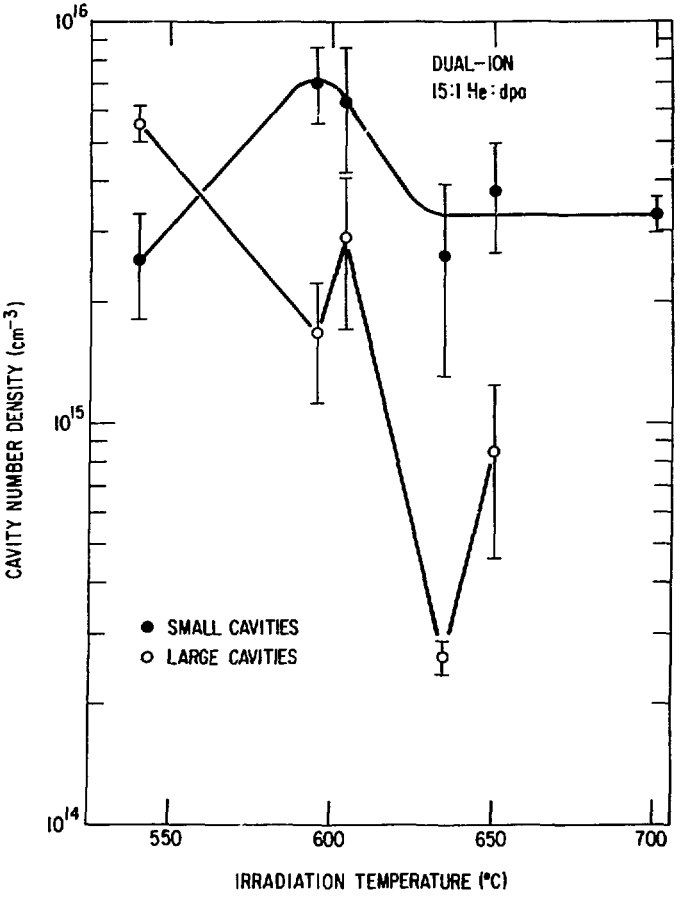

Figure 1-9. Temperature dependence of cavity number density in dual-ion irradiated 316 stainless steel (dose = 12 dpa, dose rate = 3×10^{-3} dpa·s^{-1}). The densities of small and large cavities in the bimodal size distributions are plotted separately.

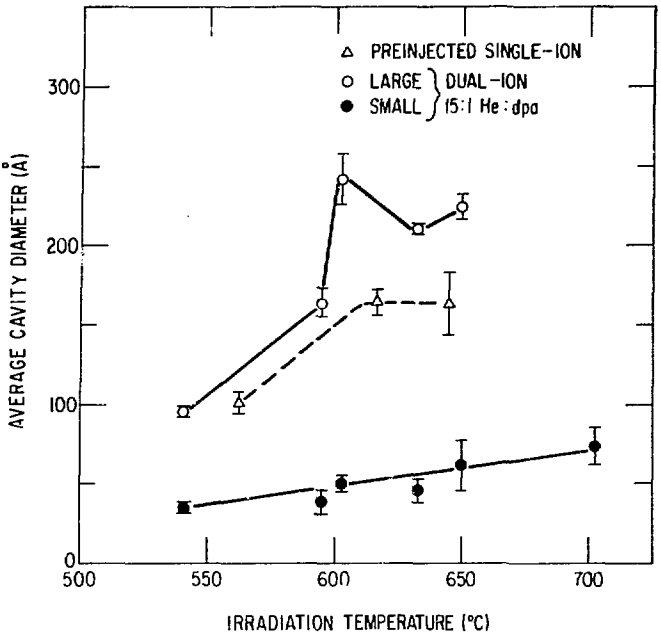

Figure 1-10. Temperature dependence of cavity size in dual-ion and preinjected single-ion irradiated 316 stainless steel (dose = 12 dpa, dose rate = 3 x 10^{-3} dpa·s^{-1}). Small and large cavity sizes are plotted separately for the bimodal size distributions found in dual-ion irradiated samples.

The most striking feature of these data is the sharp peak in swelling for the sample irradiated at 603°C. The large volume change was due to the large cavities of irregular shape shown in Fig. 1-8c. Stereo observations showed that many of these cavities were entirely contained in the foil, and dark-field images of the precipitate coating on cavity surfaces exactly reproduced the shapes seen in bright-field images (Fig. 1-7a,b) clearly indicating that they are truly voids and not etching artifacts associated with the surface. This swelling peak is, however, associated with considerable variations in $\Delta V/V$ from point to point in the sample. Four different areas gave volume changes ranging from 2-6%. The high swelling in this sample was not reproduced in a nominally identical sample, Fig. 1-8b, irradiated at 595°C. The reasons for these large regional and sample to sample variations are not clear at present.

A second peak in the swelling curve is found at 650°C. This peak is also out of the ordinary in that a swelling increase with temperature usually results from an increase in cavity size, but this peak is due primarily to a sharp rise in number density. Although duplicate dual-ion samples have not yet been inspected for this irradiation temperature, we have confidence that the behavior is reproducible because it was repeated even more dramatically in the preinjected single-ion irradiations.

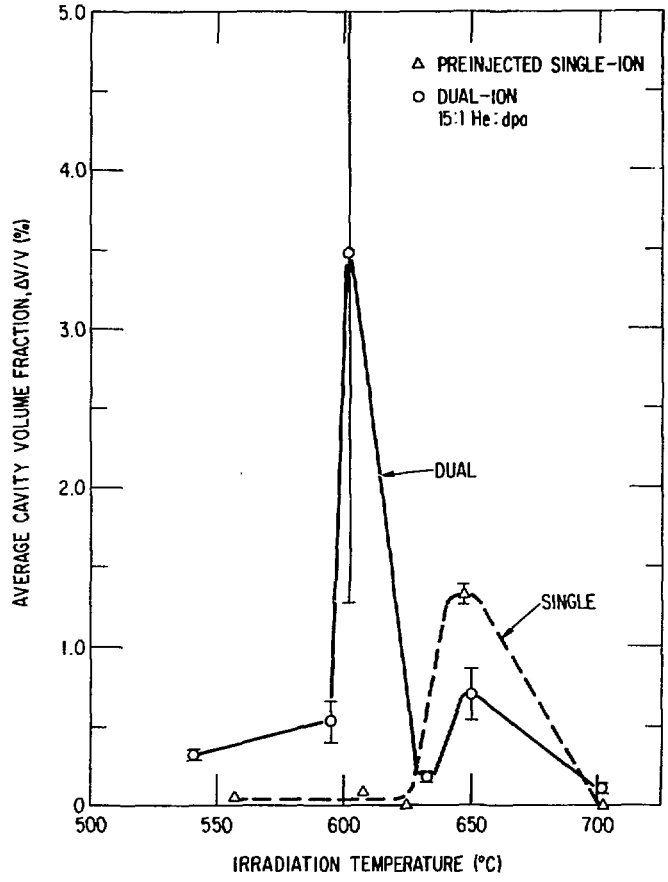

Figure 1-11. Temperature dependence of swelling in dual-ion and preinjected single-ion irradiated 316 stainless steel (dose = 12 dpa, dose rate = 3 x 10^{-3} dpa$\cdot s^{-1}$).

Swelling in Single-Ion Irradiated Samples - In the preinjected and single-ion irradiated samples, the cavity size distributions were not bimodal, and rapid swelling near 600°C was not observed. However, the swelling peak at 650°C resulting from a peak in void number density was also observed for the single-ion irradiations. No cavities were observed in the 625 and 700°C sample and it is interesting to note that unlike all other irradiated samples, no intragranular precipitates were observed either. This suggests a relationship between precipitation and cavity formation, but does not explain the absence of both.

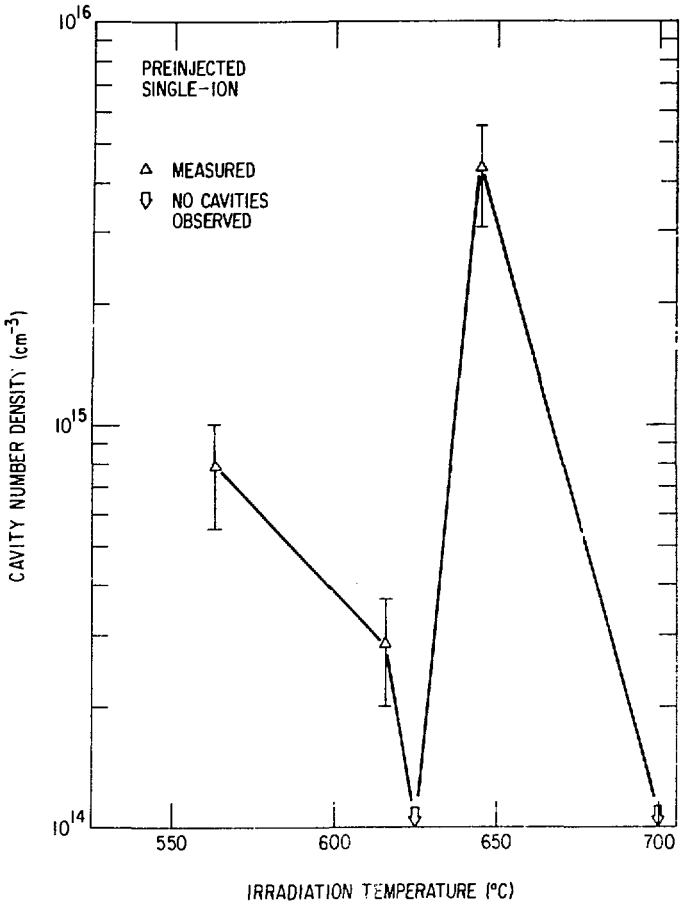

Figure 1-12. Temperature dependence of cavity number density in preinjected single-ion irradiated 316 stainless steel (dose = 12 dpa, dose rate = 3×10^{-3} dpa·s^{-1}).

1.1.2 Hydrogen Permeation and Materials Behavior in Alloys

Recent emphasis in this program has been directed towards (1) studies of hydrogen permeation in titanium-base alloys and (2) experiments with a small (~0.5-liter capacity) lithium loop fabricated with stainless-steel-clad vanadium alloy. Progress during the second half of calendar year 1979 is summarized below.

1.1.2.1 Hydrogen Permeation Studies

E. H. Van Deventer and V. A. Maroni, Chemical Engineering Division

The hydrogen permeation characteristics of a sample of Ti-6Al-4V that had been anodized on both surfaces (by McDonnell Douglas Astronautics Co.) were

measured from 450 to 665°C for hydrogen driving pressures in the range from 0.2 to 17 Pa. The permeability of the anodized sample (based on 25 data points) was found to be about the same as that of the ion-nitride-coated sample of Ti-6Al-4V studied previously, and about an order of magnitude lower than that of pure Ti-6Al-4V. The permeabilities of all of the Ti-base alloys (coated and uncoated) studied over the past year have ranged from being several hundred to being several thousand times greater than those of 300-series stainless steels.

A detailed mathematical study of all of the data obtained for the various modifications of Ti-6Al-4V investigated to date has been initiated and is beginning to produce results. A least-squares analysis was conducted on data for pure Ti-6Al-4V, ion-nitride-coated Ti-6Al-4V (one surface), and anodized Ti-6Al-4V (both surfaces) wherein the preexponential term and the activation energy were varied independently for each sample but a common refined value for the pressure exponent was sought. The results of this analysis are presented in Fig. 1-13. The shaded areas represent the overall uncertainties in both the raw data and the mathematical refinement procedure. The common pressure exponent was 0.64 with an uncertainty of less than ±10%. Accordingly, the results in Fig. 1-13 are plotted against a $(\text{pressure})^{0.64}$ factor which must be kept in mind when extrapolating these results to other pressures.

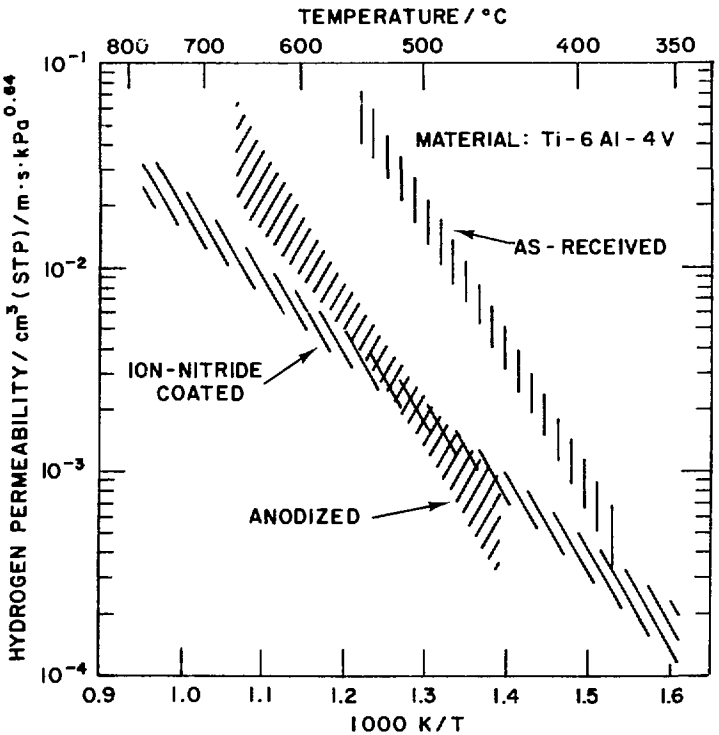

Figure 1-13. Hydrogen permeation data for as-received and treated Ti-6Al-4V samples.

It is clear from the results in Fig. 1-13 that the coating procedures caused a measurable, but far less than desirable, reduction in the permeability of Ti-6Al-4V. The optimized pressure exponent, being significantly greater than 0.5, suggests that the normally assumed bulk-diffusion-limited permeation mechanism is being affected or perhaps totally superseded by another mechanism which undoubtedly is taking place at the surfaces of the alloy. It is a fact that the product of the hydrogen solubility parameter and the true bulk diffusion parameter for Ti-6Al-4V at temperatures in the range shown in Fig. 1-13 yields a permeability significantly higher than the results shown in Fig. 1-13. Furthermore, the tendency of calculated permeation values based on the (solubility x diffusion) product is to increase with decreasing temperature, primarily because the decreasing diffusion parameter is more than offset by the increasing solubility parameter at progressively lower temperatures. The permeation mechanism observed for these titanium-based materials is certainly not classical and requires more study. Accordingly, a sample of high purity titanium has been readied for permeation study, to determine the characteristics of the unalloyed material.

1.1.2.2 Tests of Vanadium Alloy Performance in a Liquid Lithium Environment

D. L. Smith and R. H. Lee, Materials Science Division, and
R. M. Yonco and V. A. Maroni, Chemical Engineering Division

Investigations are continuing on (1) the distribution on non-metallic elements in lithium-Path C alloy systems and (2) effects of a lithium environment on the mechanical properties of selected reactive/refractory metals. Tests are being conducted in a small forced circulation stainless steel-clad vanadium alloy loop. The loop has been operating without interruption for over 10 Ms (>100 days). Initial operation was at 673 K for 2 Ms. Loop temperature was then raised to 873 K where it has since been maintained. Tests to date include the taking of four filtered lithium dip samples for determinations of the nitrogen concentration in lithium, two exposures of zirconium foil and two exposures of vanadium wire. The purpose of the zirconium exposures is to reduce the nitrogen concentration in lithium by gettering and to evaluate the hydrogen concentration in the system. The latter determination will be accomplished by analyzing the hydrogen concentration in zirconium and obtaining the equivalent hydrogen pressure at equilibrium from literature data. Analysis of the nitrogen pickup in the zirconium will provide a measure of the nitrogen in the system. Table 1-1 summarizes results of the nitrogen analyses of the lithium. The nitrogen concentration in the lithium has been reduced from an initial value of $\sim$1340 wppm to $\sim$36 wppm.

Exposure of zirconium foil at 673 K for 0.43 Ms resulted in a gold tarnish indicative of ZrN on the surface. The zirconium foil exposed at 873 K for 0.60 Ms resulted in a heavier gold film on the sample. Electron microprobe analysis of this film indicated a strong nitrogen count. These results are in qualitative agreement with calculated trends for nitrogen transfer. Quantitative analyses of the zirconium samples are in progress.

Table 1-1. Nitrogen Analyses of Lithium from the Vanadium Alloy Test Loop

Sample No.	Operation Time (Ms)	Lithium Temperature (K)	Nitrogen Concentration (appm)	Comments
VL-1	1.10	673	1342 ± 25	Represents initial concentration
VL-2	1.11	673	1325 ± 25	Duplicate sample
VL-4	5.00	871	95 ± 25	After exposure of Zr foil for 0.43 Ms at 673 K and operation at 873 K for 2.60 Ms
VL-5	6.80	873	36	After exposure of Zr foil for 0.60 Ms at 873 K

1.2 Plasma Materials Interaction

1.2.1 Carbon Coatings for Fusion Applications

S. K. Das, M. Kaminsky, Physics Division, and L. H. Rovner, J. Chin, and K. Y. Chen, General Atomic Company.

A carbon coating process for fusion reactor first-wall components, adaptable to application in-situ, would have special advantage by eliminating any need for reactor disassembly to repair or refurbish the coating. The deposition process investigated in these studies was the discharge-activated deposition of carbon from methane at about 1 Pa pressure. The coating chamber was a 76-mm-diameter quartz tube. Either dc or rf (13.56 MHz) discharges were excited by 25-mm-diameter electrodes spaced 0.15 m apart. Coatings were deposited on the interior surface of an independently biased cylindrical substrate (50 mm in diameter and 0.15 m long) which surrounded the discharge.

Gross variations in coating morphology are related to the energy density of the discharge and the negative bias applied to the substrate. With increasing values of these parameters, both dc and rf deposits varied from sooty non-coherent agglomerates (Fig. 1-14a), through columnar coatings with rounded surface deposition features, to the smooth, pore-free, nearly featureless material shown in Fig. 1-14b. This last type was obtained for substrate current densities of 40 A/m^2, bias of 600 V, and temperatures of 700 K. Polarized light and X-ray examinations of coatings cross sections showed them to have an unusual crystallographic orientation with the c-axes primarily parallel to the plane of deposition.

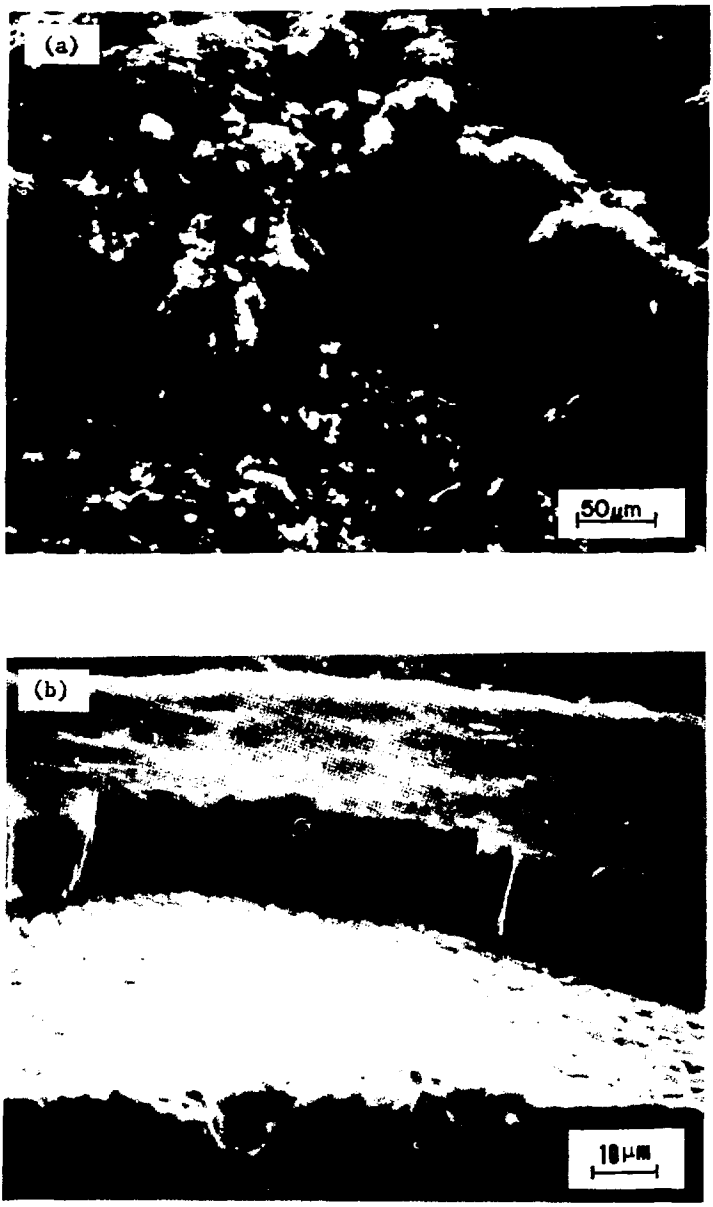

Figure 1-14. Scanning electron micrographs (SEMs) of fractured edges of (a) a sooty deposit on a graphite substrate, and (b) a dense adherent coating on a stainless steel substrate.

The ATJ and highly oriented pyrolytic graphite samples used in these studies were obtained from Union Carbide. Two sets of pyrolytic graphite samples were used, one having the c-axis nearly normal to the surface and the other having the c-axis parallel to the surface to be bombarded. Both the ATJ and the pyrolytic graphite samples were mechanically polished prior to irradiation. The carbon coatings investigated were deposited on copper or stainless steel and were well-consolidated adherent deposits obtained at high bias voltages. They had a density of about 1.7 Mg/m^3, were about 10 μm thick, and were used in the "as deposited" condition. Thermal shock testing was carried out at the Princeton Plasma Physics Laboratory using a 10-keV electron beam having a 100-mm^2 cross section. The particle irradiations were carried out at Argonne National Laboratory. The beams were mass analyzed D^+ from a dc accelerator in a vacuum of $\sim 1.3 \times 10^{-6}$ Pa. The ion fluxes during the irradiation were in the range $1 \times 10^{19} - 1 \times 10^{20}$ ions m^{-2} sec^{-1}.

1.2.1.1 Results

Thermal Loading - Carbon coated on a 12-mm-thick copper block did not sustain gross damage for 0.5-sec electron pulse heating powers less than 65 MW/m^2. At this power, the copper at the interface was melted, and even though the coating was mostly spalled off, a thin residual layer of carbon did remain over most of the surface. The performance of this coating was significantly better than for an ion-plated carbon coating having the normal crystallite orientation with c-axes predominantly perpendicular to the deposition surface.

A similar sample has been heated cyclically at a lower power level of 37.5 MW/m^2. Maximum surface temperatures reached were about 1100 K. After 1000 cycles of 0.5-sec duration, the coating was cracked but for the most part remained adherent (Fig. 1-15). Even in the few areas where portions of the coating flaked off, bare copper generally was not exposed. The pattern of cracks is two-dimensional with a cell size apparently not correlated with the as-deposited features.

D^+ and $^4He^+$ Irradiation Effects - Figures 1-16a through 1-16c show surfaces of carbon coatings on stainless steel irradiated at ambient temperatures with D^+ ions having energies of 40-, 60-, and 120-keV. The total doses, 4×10^{22}, 8.1×10^{22}, and 2.2×10^{23} ions m^{-2}, respectively, were chosen to make a direct comparison with our earlier results on ATJ graphite.[4] The as-deposited surfaces of the coatings have rounded concave depressions (Fig. 1-16d), and no detectable change in the surface topography could be seen for irradiations with 40- and 60-keV D^+ (Figs. 1-16a and 1-16b).

For the 120-keV D^+ irradiation surface, damage in the form of ridges surrounding concave depressions could be observed (Fig. 1-16c). The amplified vertical scale of these features compared with the as-deposited surface suggests that the surface has been expanded outward along preferred directions, due to the ion bombardment. The average height of the ridges is about 1.9 μm compared with the average projected range for 120-keV D^+ in the coatings of 1.3 μm. The lateral extent of the features does not appear to be correlated with the unirradiated surface. The occurrence of these ridges for the 120-keV irradiation is flux dependent since no surface damage could be detected at a reduced beam intensity, 77 kW/m^2 compared with 1200 kW/m^2 for the sample in

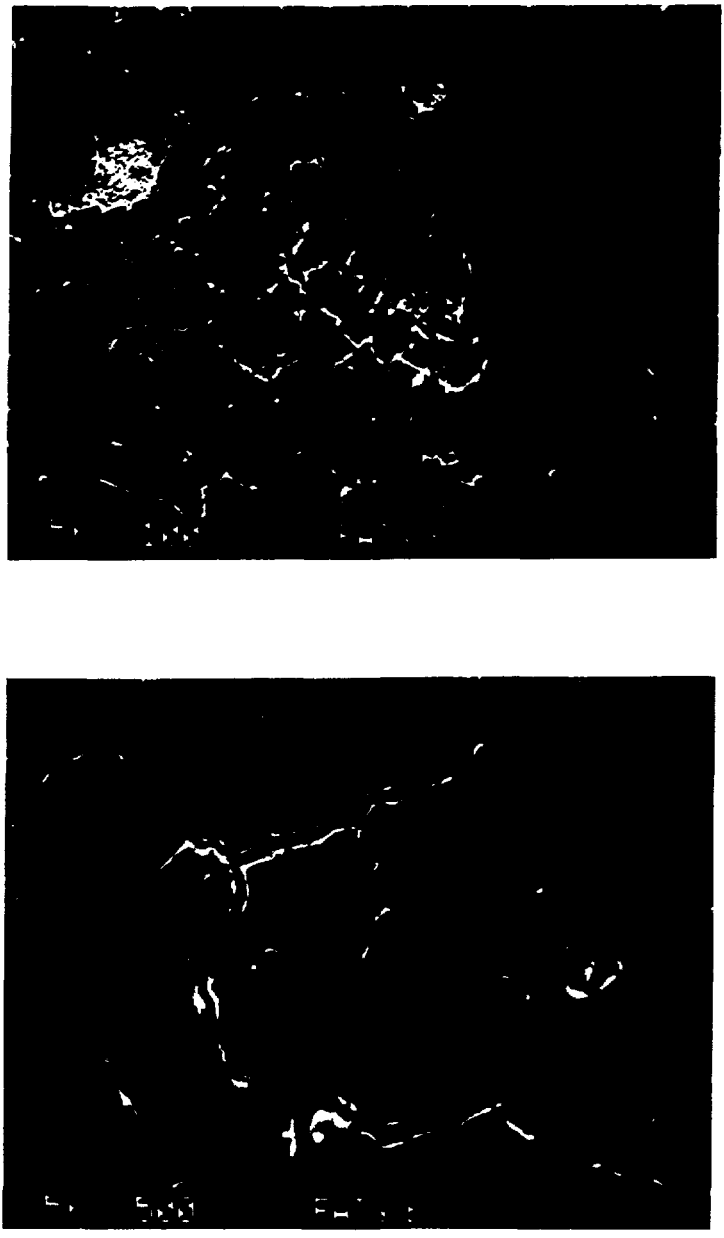

Figure 1-15. SEM of carbon coated on stainless steel subjected to 1000 cycles of 0.5-second pulse, 10-keV electron bombardment at a power level of 37.5 MW/m^2.

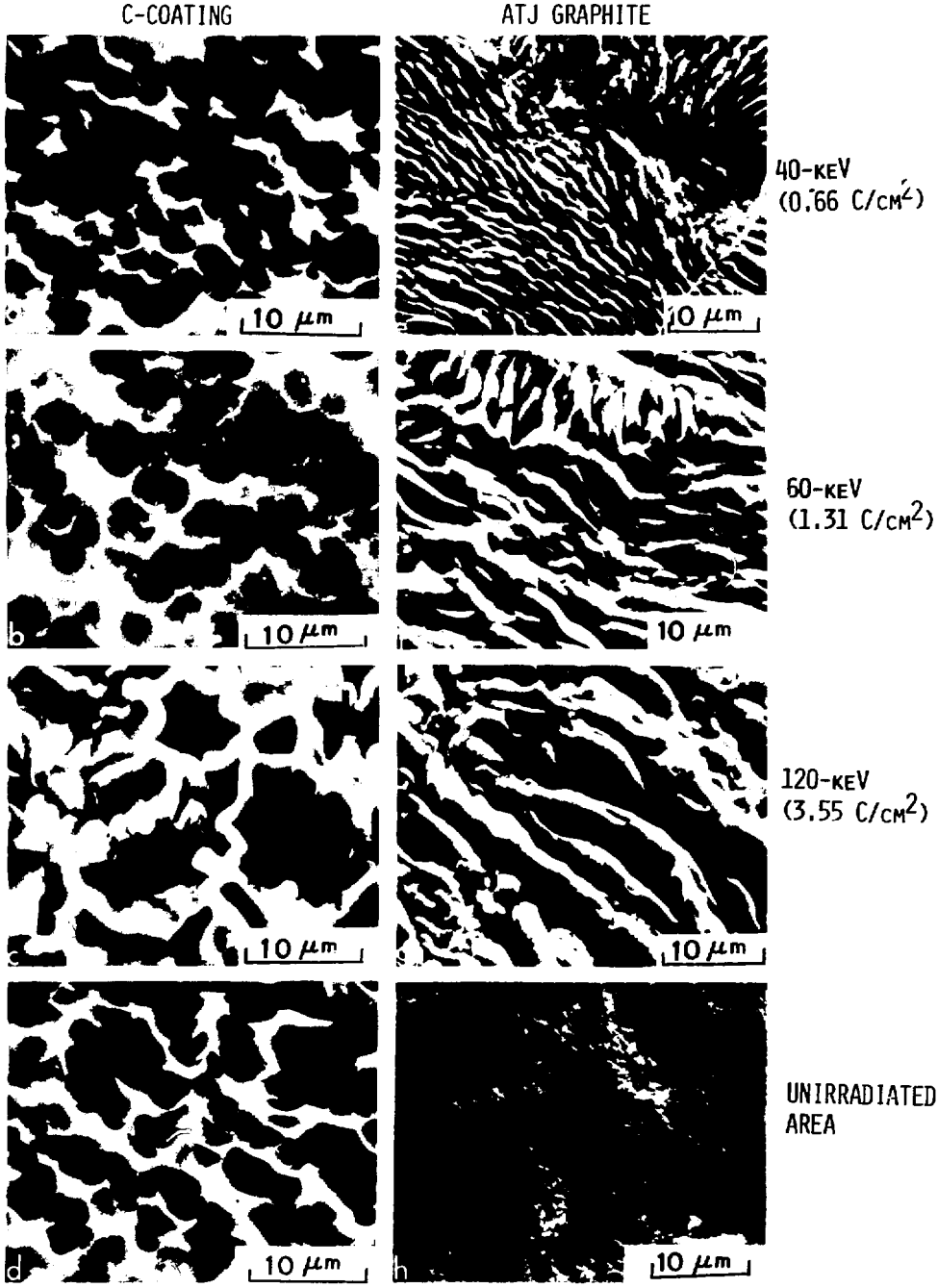

Figure 1-16. SEM of carbon coated on stainless steel and ATJ graphite irradiated at ambient temperatures with D^+ ions.

Fig. 1-16c (and 64 and 240 kW/m^2 for the 40- and 60-keV irradiations, respectively). Possible explanations for this flux dependence may relate to the increased power deposition and the slightly elevated surface temperature ($\sim$500 K), or to the sample microstructure and the mobility of the implanted ions.

Ridge formations have also been observed[4] for ATJ graphite, not only for 120-keV D^+ irradiation under similar conditions (shown for comparison in Fig. 1-16g) but also for the 40- and 60-keV D^+ irradiations (Fig. 1-16e and 1-16f). The ratio of the average height to average width of the ridges for the 120-keV D^+ irradiations is only about 1.3 for the carbon coating as compared to a ratio of 2.2 - 3.4 for ATJ graphite. Figures 1-16e through 1-16g show that the size of the ridges is clearly dependent on the beam energy. The ridges observed on the coated samples are thought to be growth features of the kind reported previously for ATJ graphite[4] and for pyrocarbon[5].

It was suspected that the surface features developed under bombardment were characteristic of the sample crystalline structure and orientation. In order to study these dependences, highly oriented pyrolytic graphite samples were irradiated. Figures 1-17a and 1-17b show highly oriented pyrolytic graphite samples, with the c-axis parallel to the surface, which have been irradiated with 40- and 60-keV D^+ ions to a dose of 3.1×10^{22} ions m^{-2}. Surface ridges and grooves have formed that were not present before irradiation (Fig. 1-17c). The ridges within each grain are predominantly aligned in one direction (Fig. 1-17a). Irradiation of surfaces which had their c-axis normal to the surface (i.e., present basal planes to the ion beam) showed the formation of domes instead of ridges for both 40- and 60-keV D^+ irradiations (see Figs. 1-17d and 1-17e) to the same dose of 3.1×10^{22} ions m^{-2}. These dome-shaped features were not present before irradiation, as seen from Fig. 1-17f. The nature of the surface features developed is clearly determined by crystallographic orientation, whereas the size of the features is determined by the ion energy and its depth of penetration. The coatings shown in Fig. 1-16 are less well oriented than these samples, but the surface features developed display the ridges expected for their preferred orientation, which is with the c-axes parallel to the surface.

The nature of the surface damage due to irradiation by D^+ on the highly oriented pyrolytic graphite and carbon coatings show that the damage is strongly orientation and microstructure dependent; ridge formation occurs on surface planes which have c-axes parallel to the surface, whereas domes are observed on planes with the c-axes being normal to the irradiates surface (basal planes exposed). Similar dome formation has been reported[6] on basal planes of thin (50-100 nm) pyrolytic graphite samples irradiated at 600-800 K with 70-100 keV He^+ ions for total doses of 5×10^{21} to 1×10^{22} ions m^{-2}. These authors concluded that the domes were not blisters formed by excess helium gas pressure. Furthermore, we have reported earlier[4] that the ridges observed on ATJ graphite are solid, and not hollow (unlike surface blistering) and also that a general surface uplifting has been produced in pyrocarbon[5] by 0.6 and 3.5 MeV He^+. It can also be pointed out that Veprek, et al.[4] observed convolutions to the basal planes of pyrolytic graphite irradiated with 2 MeV He^+ ions at 725 K for a dose of 4.5×10^{21} ions m^{-2}. They attributed this surface deformation to the depth dependence of lattice stresses induced by radiation damage. Thus, it appears that both the formation of ridges and of domes in the present observations is due to growth phenomena or lattice expansion and is not associated with the surface deformation due to excess pressure in gas bubbles.

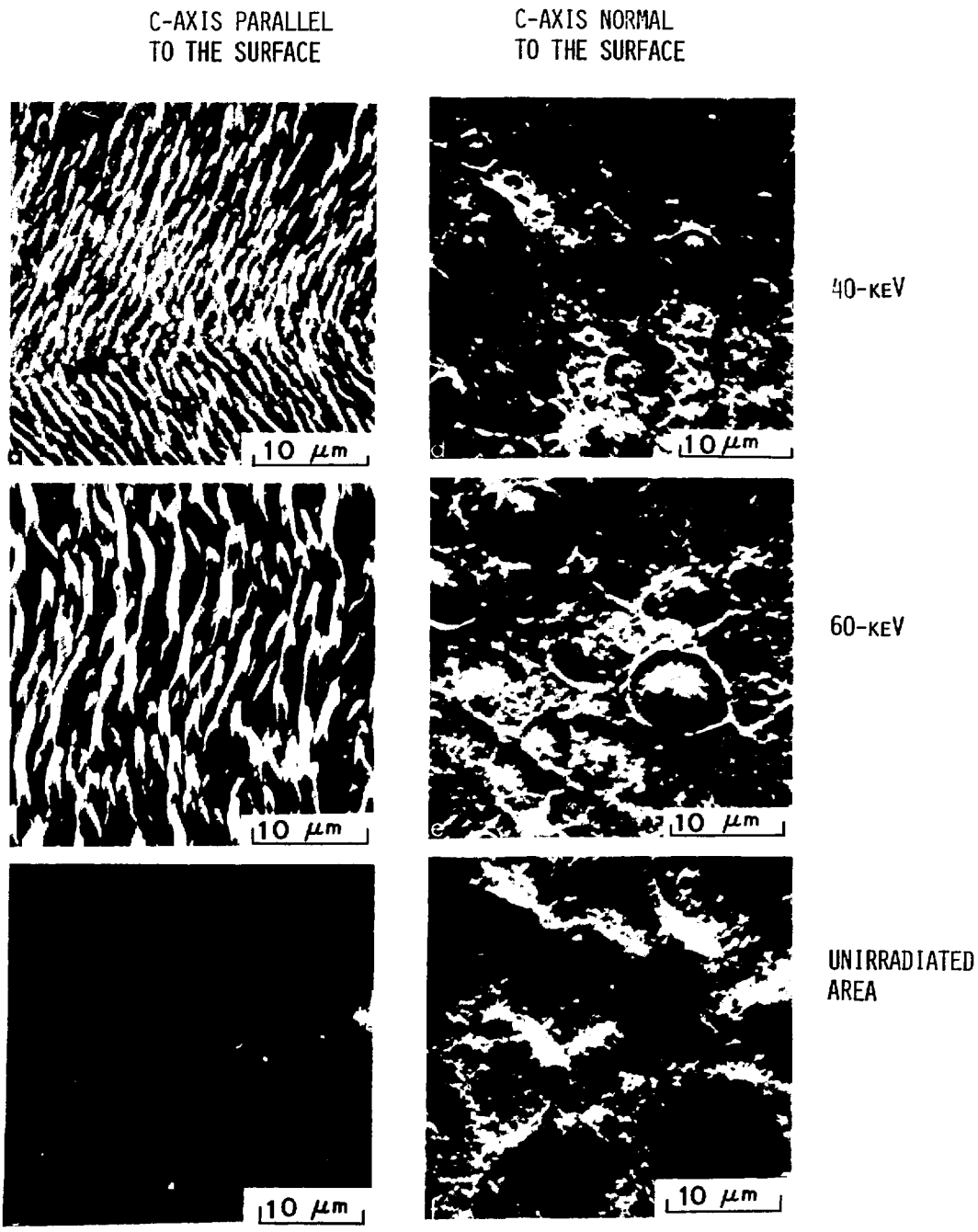

Figure 1-17. SEM of highly oriented pyrolytic graphite irradiated at ambient temperature with D^+ ions to a dose of 0.5 C/cm^2.

The surface damage under D^+ irradiations show that the surface damage of discharge vapor deposited carbon coatings is less than that of ATJ graphite or highly oriented pyrolytic graphite, for similar irradiation conditions. The good adherence of these coatings and their relative stability under high energy ion bombardment reflects favorably on their potential use on various components in the plasma chamber of a fusion reactor. Their overall merit will depend on the total erosion rate produced by the complex plasma-wall interactions to be encountered during actual service, including chemical effects of sputtering and stability under neutron irradiation.

1.2.2 Surface Damage of TiB_2 Coatings Under Energetic D^+ and $^4He^+$ Irradiations

M. Kaminsky and S. K. Das, Physics Division

Studies of the surface damage and erosion of chemically vapor deposited (CVD) TiB_2 coatings on metallic substrates have been conducted for irradiation with 5 ± to 120 keV D^+ and $^4He^+$ ions for different doses at room temperature. Furthermore, D^+ and He^+ irradiations of commercial grade Ti were conducted to study the difference in surface damage and erosion between the TiB_2 coatings and Ti metal.

The TiB_2 coatings were obtained from D. Mattox, Sandia Laboratory. The thickness of the TiB_2 coatings ranged from 15 to 25 μm. The coating surfaces were characterized by scanning electron microscopy (SEM) and scanning Auger microscopy (SAM) both prior to and after the irradiations. SEM analysis of the "as received" coatings reveal that the TiB_2 coatings are quite rough. SAM analysis of the "as received" TiB_2 coatings revealed the presence of C, O, Si and Cl impurities which could be subsequently reduced or eliminated by sputter cleaning prior to D^+ or He^+ irradiation. One set of TiB_2 coatings were mechanically polished with μm alumina powder whereas another set was left in the "as deposited" condition. The commercial grade Ti (99.5% pure obtained from Roc-Ric, Belleville, NJ) was given a fine metallographic polish prior to irradiation. The irradiations were carried out with mass analyzed D^+ and $^4He^+$ ions from a dc accelerator in a vacuum of $\sim 1.3 \times 10^{-6}$ Pa. The incident ion flux during both the D^+ and He^+ irradiation was $\sim 1 \times 10^{14}$ ions/(cm^2-sec).

Irradiation of TiB_2 Coatings - Figure 1-18 shows scanning electron micrographs of polished TiB_2 surfaces irradiated with 5-, 10-, 15-, 20- and 100-keV He^+ (Figs. 1-18a through 1-18e) and D^+ ions (Figs. 1-18f through 1-18k). Here, one notices that the average blister diameter for both D^+ and $^4He^+$ with energies in the range 10-20 keV increases with increasing projectile energy (see Figs. 1-18b, 1-18d and 1-18g through 1-18i). Furthermore, for a given energy in this energy range, the blister diameter for D^+ irradiation is larger than for $^4He^+$ irradiation. This is quantitatively illustrated in Fig. 1-19, which shows the histograms of the distribution of blister diameters for 15-keV $^4He^+$ and D^+ irradiations. The most probable blister diameter, D_{mp}, and the average blister diameter, D_{av} for the 15-keV $^4He^+$ irradiation are 0.93 μm and 0.86 μm, respectively, whereas for 15-keV D^+ irradiation, the value for D_{mp} is 1.51 μm and for D_{av} is 1.48 μm. The observation that the blister diameter increases with increasing projectile energy is similar to our earlier on various metals. The latter result, that for a given energy the blisters formed by D^+ irradiation are larger than those formed by $^4He^+$ irradiation is similar to our earlier observations made on D^+ and He^+ irradiated ceramic coatings.[8] This is related in part to the greater depth of penetration of deuterons and more importantly, to the lower permeation rate for deuterium than for helium in such coatings. This observation may be related to the fact that

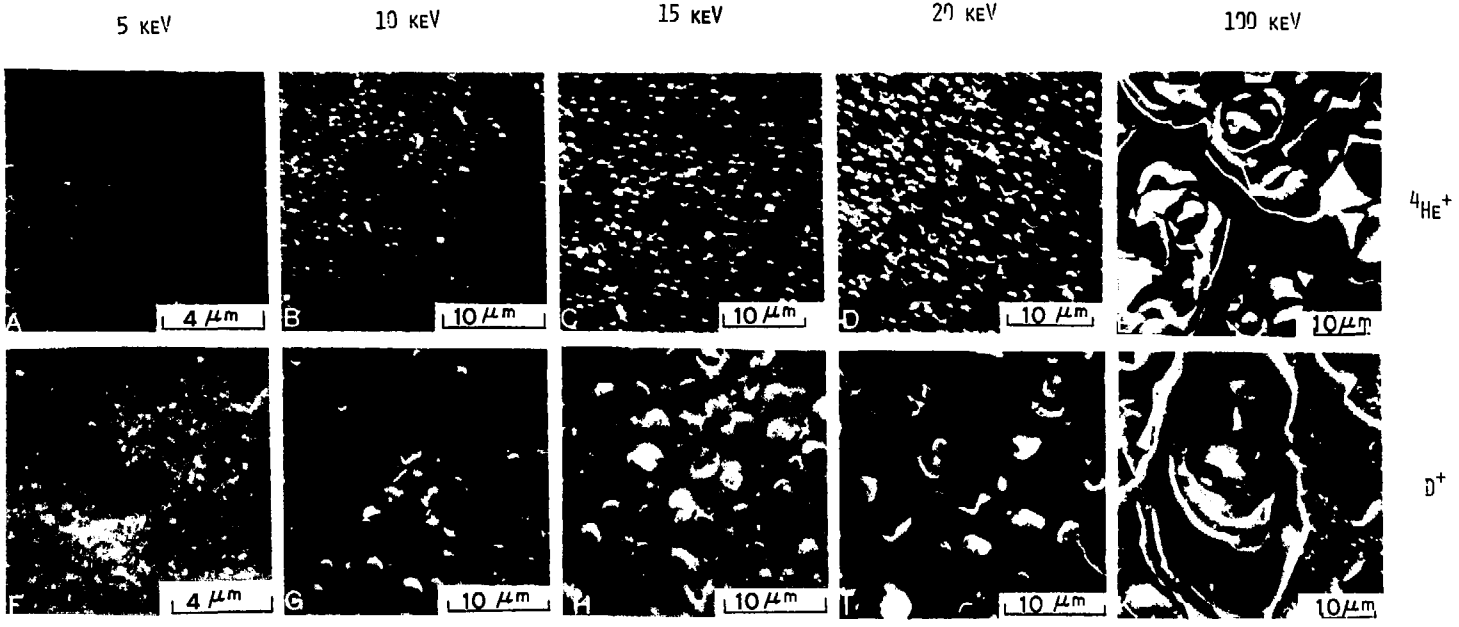

Figure 1-18. Scanning electron micrographs (SEMs) of polished TiB_2 coatings irradiated at room temperature for a dose of 3.1×10^{18} ions/cm^2 with $^4He^+$ (see A-E), and D^+ ions (F-K) for the energies indicated.

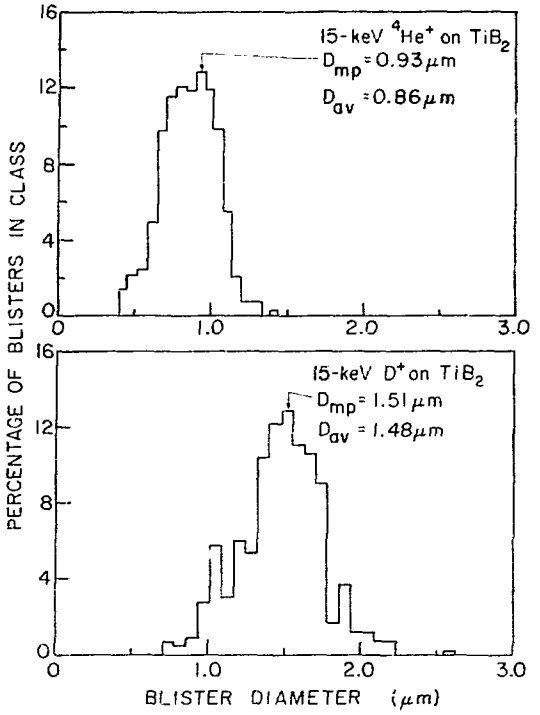

Figure 1-19. Histograms of the distribution of blister diameters for polished TiB_2 coatings irradiated at room temperature with 15-keV $^4He^+$ and D^+ to a dose of 3.1 x 10^{18} ions/cm^2.

the blister skin thickness is larger and the sputtering yield is lower for the D^+ irradiation than for He^+ irradiation of TiB_2 under otherwise identical irradiation conditions.

Quantitative estimates of the erosion yield due to blistering were made from measurements of blister skin thickness and the area lost due to blister exfoliation. These data are summarized in Table 1-2, for room temperature irradiation of polished TiB_2 coatings with D^+ and He^+ ions for a dose of 3.1 x 10^{18} ions/cm^2. The erosion yields for the 100-keV irradiation are much larger than the yields for the low-energy (10-20 keV) irradiations. It may be noted that for irradiations with D^+ and $^4He^+$ ions at 100-keV, the blister skin thickness values (0.7 μm and 0.42 μm, respectively) agree well with the projected range calculated (R_p=0.64 μm and 0.40 μm, respectively), according to LSS, but for energies < 20 keV, the blister skin thicnessses are larger than the calculated projected ranges. For example, for the 10-, 15-, and 20-keV D^+ irradiations the measured skin thickness values appear to be about a factor of two larger than the values calculated according to LSS. This can be due in part to the swelling of the blister skin and to the inaccuracies in the electronic stopping power used in the range calculation.

Table 1-2. Estimated Erosion Yields Due to Blistering of Polished TiB_2 Coatings Irradiated at Room Temperature with D^+ and He^+ Ions for a Dose of 3.1×10^{18} ions/cm^2

Projectile	Erosion Yield (number of TiB_2 molecules per incident ion).	
10	$(0.6\text{-}1.4)\times10^{-2}$	$(0.17\text{-}0.35)\times10^{-2}$
15	$(0.34\text{-}0.75)\times10^{-2}$	$(0.44\text{-}1.5)\times10^{-2}$
20	$(0.24\text{-}3)\times10^{-2}$	$(0.8\text{-}1.4)\times10^{-2}$
100	0.5 ± 0.2	0.35 ± 0.1

The results described so far are for mechanically polished surfaces, but in a fusion device the coating will most likely be used in the "as deposited" condition. The surfaces of "as deposited" TiB_2, polished TiB_2, and polished Ti before irradiation are shown in Figs. 1-20a, 1-20b, and 1-20c, respectively. Figure 1-20d shows a typical result for an "as deposited" TiB_2 surface irradiated at room temperature with 100-keV $^4He^+$ to a dose of 3.1×10^{18} ions/cm^2. For the sake of comparison, polished TiB_2 and Ti surfaces irradiated under identical conditions are also shown in Figs. 1-20e and 1-20f, respectively. Even though the "as deposited" TiB_2 surface is very rough, the blisters can be clearly seen in the irradiated area (marked by arrows in Fig. 1-20a). The estimated erosion yield for the "as deposited" TiB_2 for 100-keV $^4He^+$ irradiation at room temperature for a dose of 3.1×10^{18} ions/cm^2 is $(4\text{-}8) \times 10^{-3}$ TiB_2 molecules per incident ion, a value which is about two orders of magnitude smaller than for polished TiB_2. This difference in yield values between the "as deposited" (rough) and the polished TiB_2 samples is similar to a trend which had been observed earlier for rough and polished surfaces of Mo under He ion irradiation[9].

The estimated erosion yields due to blister exfoliation for polished TiB_2 coatings irradiated with D^+ and He^+ are plotted in Fig. 1-21 as a function of projectile energy. It is interesting to note that for both D^+ and $^4He^+$ irradiations, the erosion yield increases with increasing projectile energy for the dose studied, and at a given energy the yields are higher for D^+ irradiation than for $^4He^+$ irradiation. The former result may in part be due to the increased power deposition with increased projectile energy. For example, for 40-keV D^+ irradiation the power deposition was only 2.5 W cm^{2}as compared with 76.2 W cm^{-2} for the 120-keV D^+ irradiation. This in turn causes a moderate increase in surface temperature (up to about 250°C for the 120-keV irradiation) which aids in increased blister exfoliation at higher projectile energies.

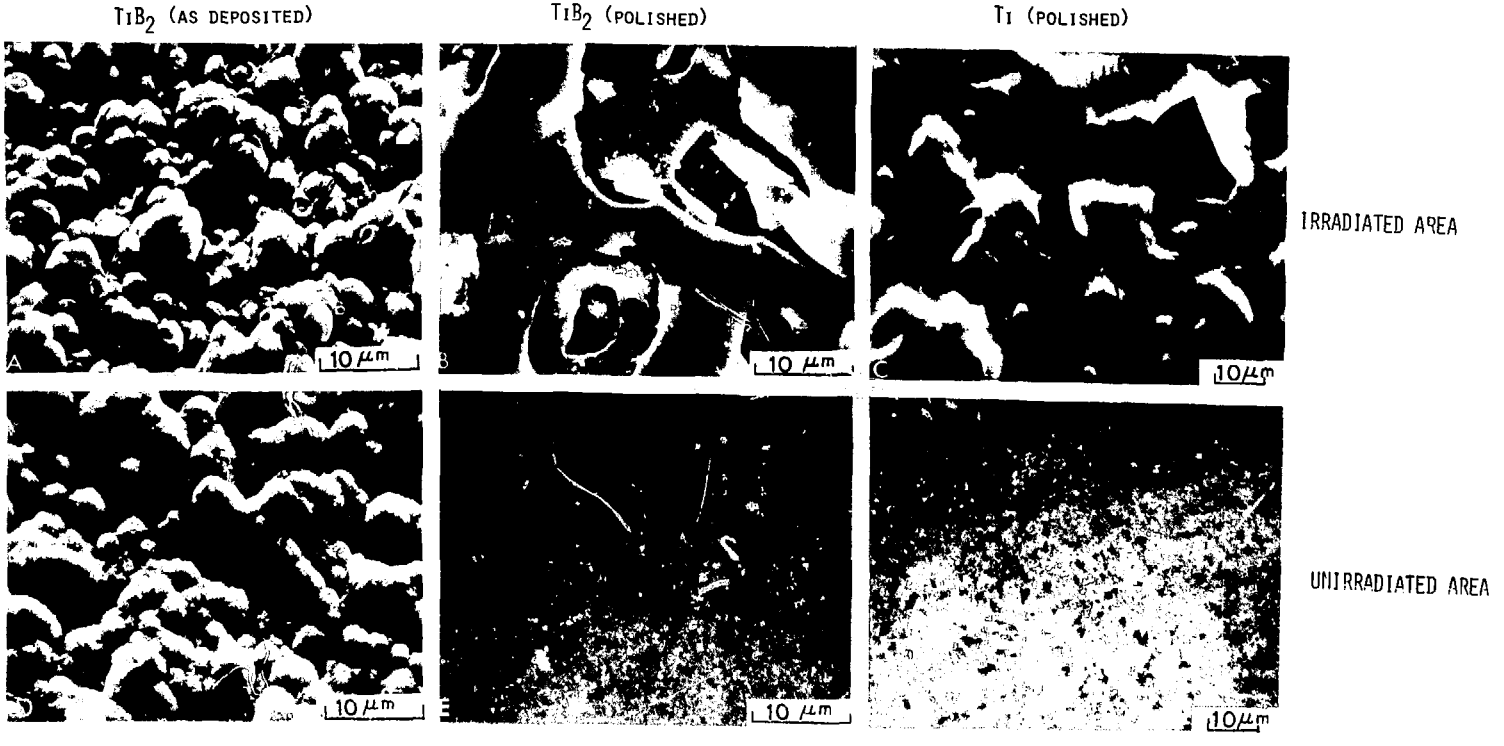

Figure 1-20. (A)-(C) SEMs of surfaces of (A) "as deposited" TiB_2 coating, (B) polished TiB_2 coating, (C) polished Ti before irradiation. (D)-(F) SEMs of similar surfaces after irradiation at room temperature with 100-keV $^4He^+$ to a dose of 3.1×10^{18} ions/cm^2, (D) "as deposited" TiB_2 coating, (E) polished TiB_2 coating and (F) polished Ti.

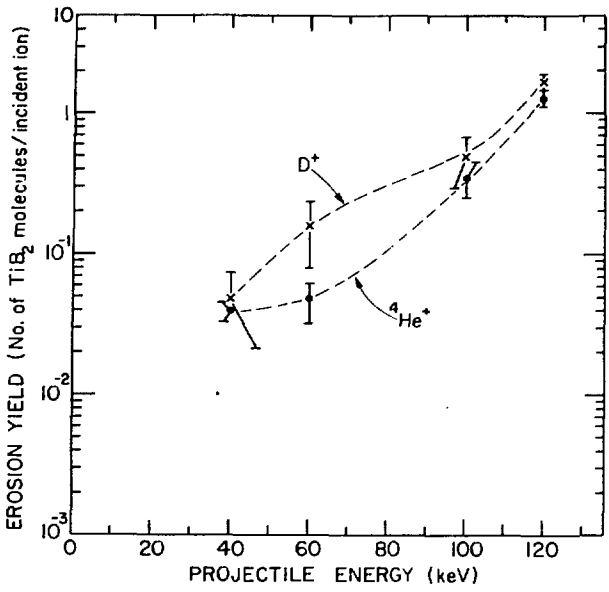

Figure 1-21. Semi-logarithmic plot of erosion yields vs. projectile energy for polished TiB_2 coatings irradiated at ambient temperatures with D^+ and $^4He^+$ ions for a dose of 3.1×10^{18} ions cm^{-2}.

For the 40- and 60-keV D^+ and He^+ irradiations of the "as deposited" TiB_2, no surface damage due to blistering could be detected, while the polished coating surfaces showed significant blister exfoliation. For the 120-keV D^+ and He^+ irradiations, the observed blister exfoliation of the "as-deposited" TiB_2 coatings is about two orders of magnitude smaller than that for the polished TiB_2 coatings.

1.2.3 Suppression of Sputter Induced Erosion Rate from Alkali Metal Covered Surfaces

A. R. Krauss and D. M. Gruen, Chemistry Division

Sputtering is one of the principal mechanisms for the introduction of impurities into the plasma of magnetic-confinement fusion devices. Under the expected conditions of low energy light particle bombardment, the sputtered atoms originate almost entirely in the first monolayer of material facing the plasma. It is therefore important to optimize the properties of (at least) the first monolayer so that the sputtered surface introduces the least possible amount of high Z impurity into the plasma. It is desirable to have surfaces which have a low sputtering-induced erosion rate and which produce sputtered particles with high secondary ion fraction, low kinetic energy and low

atomic number. The surface must also be stable and compatible with the fusion reactor environment. Because of the sheath potential and magnetic fields encountered in a tokamak, sputtered ions are not expected to contribute to plasma contamination. However, the low secondary ion yield of most materials has prevented the use of this effect to reduce the impurity influx.

We have succeeded in producing very thin (monolayer) films of lithium on a molybdenum substrate in which the first four criteria have been met, resulting in a reduction in the sputtering-induced erosion rate in the presence of an electrostatic field, such as would be produced by the sheath potential in a magnetic-confinement fusion device. Other alkali metal-substrate combinations are expected to produce an even greater suppression of the erosion rate. The phenomenon of surface segregation in alloys is expected both experimentally and theoretically to be a means of obtaining stable, uniform and chemically pure alkali metal monolayers in a tokamak environment while satisfying the sixth requirement of chemical and thermodynamic compatibility with the fusion reactor.

In order to understand the conditions leading to high secondary ion yields, we have begun preliminary experiments on the secondary ion emission of alkali metal alloys and adsorbed alkali metal overlayers. The principle of the experiment is illustrated in Fig. 1-22. If the alkali metal (eg., Li) is in the form of an adsorbed monolayer (Fig. 1-22a) the bond between Li and a high work function substrate is largely ionic[10] and there is a high probability that the

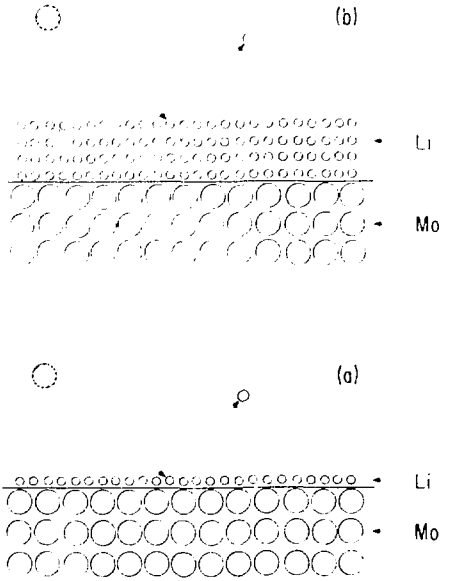

Figure 1-22. Ejection of surface Li atom bonded (a) to the Mo substrate and (b) to a multilayer Li film. In the first case the bond is polar-ionic and in the second it is (delocalized) metallic. The metallic bond corresponds to a low binding energy and zero net equilibrium charge transfer.

alkali metal is sputtered as an ion. If, however, the alkali metal is sputtered from a multi-layer film (Fig. 1-22b) ionic bonding is not possible and other mechanisms are responsible for secondary ion production. If ionic bond breaking during sputtering is an important ionization process, the secondary ion yield of the alkali monolayer should be much higher than that of the multilayer. If a negative bias such as that produced by the sheath potential of a tokamak is placed on the sample during sputtering, the positive secondary ions will be returned to the surface, thereby reducing the sputter-induced erosion rate. Because of the ionic nature of the bond, the adsorbed monolayer has a much higher binding energy[11] and consequently lower sputtering yield and vapor pressure than the bulk alkali metal.

We have used Auger electron spectroscopy to monitor the erosion rate of multi-layer and mono-layer Li films on a Mo substrate. The lithium was deposited by a lithium aluminosilicate ion source. Auger measurements were then made while sputtering with and without sample bias. Representative results are shown in Fig. 1-23. The data plotted represent the Auger peak-peak signal height for the Li (40 eV), Mo (28 eV) and Mo (186 eV) transitions. The escape depth of these electrons is only 2-3 monolayers. The slight step in the Mo (186) signal at 108 minutes appears to correspond to a 2 monolayer film, while the rapid change in all signal intensities starting at 130 minutes corresponds to removal of the last monolayer.

By comparing the erosion times of the first and second alkali metal layers with and without sample bias, we hope to be able to specify the ionization mechanism for sputtered alkali metals. Preliminary results indicate that the first monolayer has a longer sputtering lifetime than the second, regardless of bias, and that sample bias reduces the erosion rate of the first monolayer. It is expected that in the near future, SIMS and XPS measurements will indicate more accurately the secondary ion fraction of these alkali metal monolayers.

A Li monolayer with a high secondary ion fraction would satisfy the first four of the stated requirements (low erosion rate, low secondary ion kinetic energy and atomic number, and high ion fraction). We have previously proposed[12] a means of producing such a surface in a self-replenishing manner suitable to a tokamak environment by the use of alloys containing small alkali metal components. Such materials are air stable and in the case of at least one such system[13] (Si-Li) have been shown to produce stable Li surface monolayers when heated to temperatures comparable to those expected for a tokamak first wall. A number of candidate alloys will be examined in future experiments.

1.2.4 Sputter-Induced Modification of Near-Surface Alloy Composition

L. E. Rehn and H. Wiedersich, Materials Science Division, and
S. Danyluk, University of Illinois

Many properties of the first wall are known to depend upon its near-surface chemical composition, e.g., sputtering rate, corrosion resistance, and susceptibility to radiation blistering. An understanding of sputter-induced compositional changes at alloy surfaces is therefore important for the design of advanced fusion devices. Under the sponsorship of the Basic

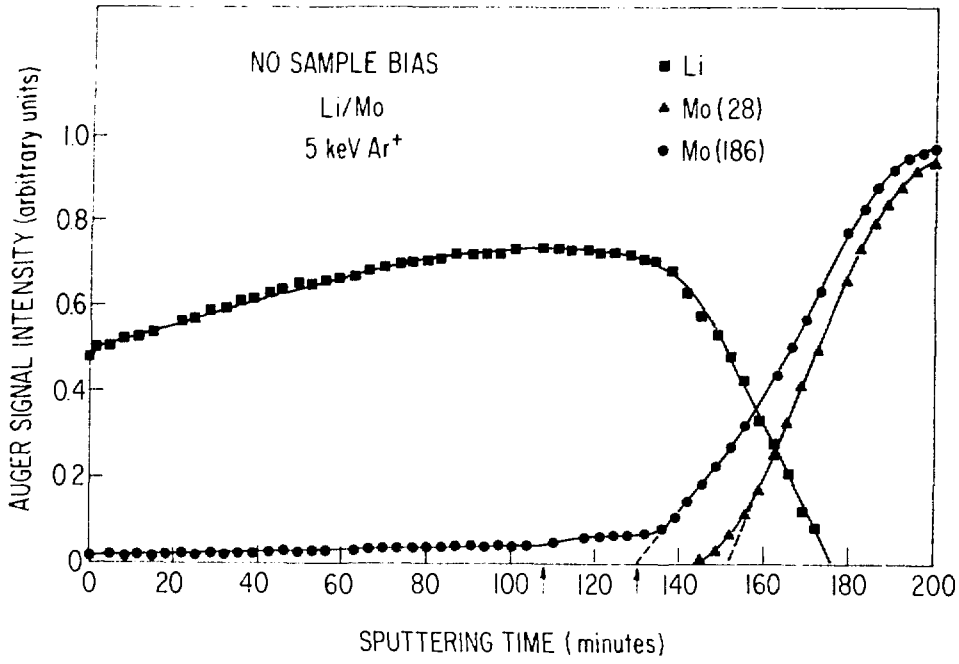

Figure 1-23. Time dependence of Li and Mo Auger peak-peak signal intensity during sputtering of a multilayer Li film on a Mo substrate. The arrows indicate the first and second monolayer.

Energy Sciences (BES) Program of DOE, we have studied surface and subsurface compositional changes induced in a Cu-Ni(40 at. %) alloy during ion sputtering at temperatures between 50 and 600°C.

Sputtering of Cu-Ni alloys at room temperature is known to preferentially remove Cu. However, only very limited information exists on elevated-temperature sputtering effects and no direct experimental information is available on subsurface changes. We have used Auger electron spectroscopy (AES) to investigate near-surface compositional changes in a Cu-40 at. % Ni alloy in situ; that is, at temperature during sputtering. Four Auger peaks were monitored: Ni transitions at 102 and 716 eV and Cu transitions at 106 and 920 eV. The escape depths of Auger electrons vary with energy. Electrons from the low-energy ($\sim$100 eV) transitions have a mean free path of $\sim$4 Å, while those from the high-energy transitions (700-1000 eV) have a mean free path of $\sim$15 Å.[14] The low-energy transitions are therefore more sensitive to the composition of the first few atom layers; the high-energy transitions average the composition over several additional atom layers.

The results of our in-situ measurements can be summarized as follows: At temperatures below 300°C, measurements of the low-energy Auger transitions show that the Ni concentration in the top few atom layers rises quickly to

∿60 at. % Ni during sputtering, then remains constant during further sputtering. Above 300°C, increasingly longer times are required before the Ni concentration becomes constant within experimental error. However, the measurements show that the composition of the top few atom layers eventually approaches ∿60 at. % Ni regardless of temperature. The results from the high-energy transitions (Fig. 1-24) reflect the average composition of a considerably thicker surface layer. They reveal that above 300°C, the subsurface is enriched in Ni considerably more than the 60 at. % found for the uppermost atom layers, that the subsurface Ni enrichment is still increasing after two hours of sputtering, and that the degree of subsurface Ni enrichment increases markedly with temperature. Subsequent measurements at room temperature show that after two hours of sputtering at 500 and 600°C, the subsurface Ni enrichment extends to a depth of ∿1 and 3 μm, respectively (Fig. 1-25). Such large depths indicate that appreciable diffusion occurs at temperatures above 300°C owing to mobile point defects created by the sputtering process.

Our results lead to the following description of compositional changes which occur in the Cu-Ni alloy during sputtering. Both the low- and high-energy Auger transitions, which sample depths of a few and several atom layers, respectively, yield the same degree of Ni enrichment after sputtering for short periods of time at temperatures up to 300°C. This implies that sputtering below 300°C quickly produces a steady-state altered layer whose composition is constant over a depth which is greater than the ∿15 Å escape

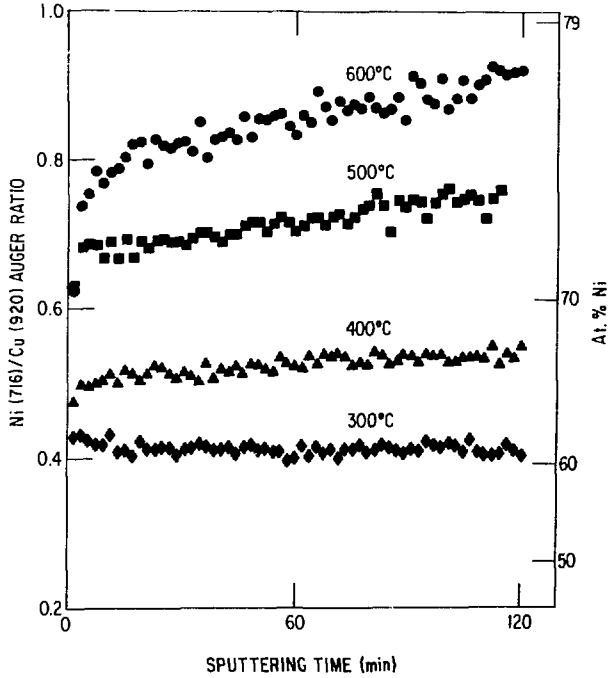

Figure 1-24. Peak-to-peak ratios of the higher-energy Auger transitions, Ni(716 eV) and Cu(920 eV), as function of sputtering time at different temperatures. Corresponding Ni concentrations are indicated on the right. A 195 μA/cm^2 beam of 5 kV Ar^+ ions was used for sputtering.

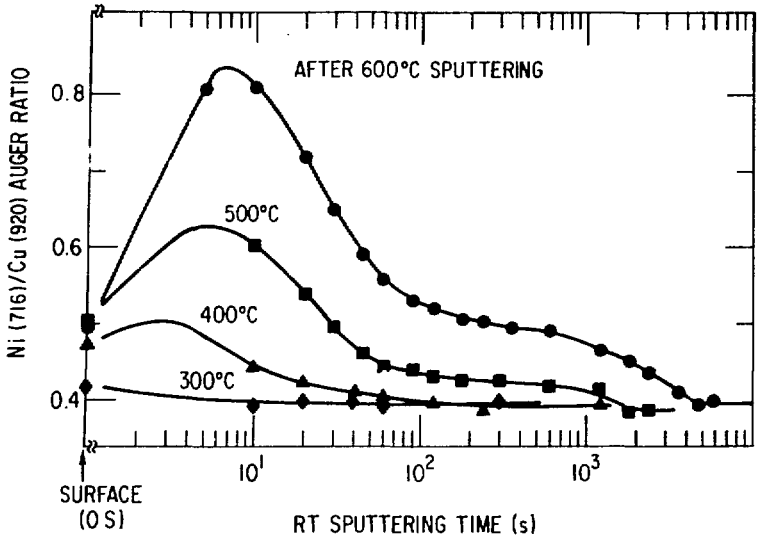

Figure 1-25. AES measurements during sputtering at room temperature at a rate of $\sim$ 6 Å/s. Each specimen was quickly cooled to room temperature after two hours of sputtering at the indicated temperature. Above 300°C, an increase in the sputtering temperature increases the depth of Ni enrichment.

depth of the high-energy transitions. Although the surface concentration eventually approaches a value of $\sim$60 at. % Ni regardless of temperature, Ni enrichment in the subsurface region exceeds that of the surface during sputtering above 300°C. To our knowledge, sputter-induced subsurface segregation in excess of that found at the surface has not been observed or predicted previously. We believe that the subsurface Ni enrichment peak results from Gibbsian segregation of Cu toward the alloy surface.

Substantial surface enrichment of copper is known to occur at equilibrium in Cu-Ni alloys. At temperatures where atomic mobility is sufficient to compete with the rate of surface recession during sputtering, Gibbsian segregation will tend to enrich the outermost atom layer in Cu. The excess Cu which is driven to the surface at elevated temperatures via the Gibbsian adsorption driving force is continually removed by preferential sputtering. Eventually, sufficient Cu depletion (Ni enrichment) occurs in the subsurface region so that the rate at which additional Cu is supplied to the surface is reduced, and the composition of the outermost layer approaches the same value for all temperatures. At equilibrium, the Gibbsian adsorption layer is extremely narrow,[15] extending only one or two atom layers into the specimen.

As Cu depletion occurs in the atom layers immediately beneath the surface layer, a concentration gradient begins to build toward the interior of the specimen. This gradient provides a long-range driving force for Cu diffusion toward the near-surface, Cu-depleted zone. Sputter-induced point defects enhance the diffusion. The result is a subsurface maximum in the Ni enrichment followed by a long Ni-enriched tail which penetrates deep into the specimen.

We have shown that sputtering can induce compositional changes beneath the surface of an alloy which are significantly larger than the changes produced directly at the surface by preferential sputtering. In addition, changes in alloy composition have been observed far beyond the range of the bombarding ions. These discoveries provide new insight into compositional changes that should occur at the plasma-first wall interface during operation of future fusion reactors. They also may lead to useful methods for modification of near-surface properties of alloys.

1.3 Dosimetry and Damage Analysis

1.3.1 Neutron Dosimetry

L. R. Greenwood, Chemical Engineering Division

1.3.1.1 Fission Reactor Dosimetry at ORR - Low Power Spectral Measurement

Analysis has been completed for the low power spectral measurement in the Oak Ridge Research Reactor. Four 24" long aluminum capsules were irradiated in core position E7 during January 1979 at a power level of 1 MW (61.53 MWH). Spectral sets of 10 dosimetry wires were placed at eight locations giving a total of 28 separate activation measurements at each location. Four wires (Ni, Co-Al, Fe, and Ti) were also placed in each capsule to measure the flux gradients.

Figure 1-26 shows the measured flux-spectrum at the maximum flux position, about 3" below midplane. Table 1-3 summarizes the measured flux-spectra as well as neutronics calculations. Whereas our fast flux (>1 MeV) agrees very well with calculations, our measurements indicate substantially fewer neutrons below 1 MeV than predicted by calculation. Three possible explanations for the difference have been formulated, as follows. First, the calculations did not include a large graphite cylinder in a nearly core location which would indeed moderate the spectrum. Secondly, the measurement was at a reduced power level of 1 MW whereas calculations were at 30 MW. Finally, the neutronics calculations (7 group, 3D) may not represent the ORR configuration adequately. Hopefully, these effects can be sorted out by later comparisons to experiments in the same location at full power (ORR-MFE2) and at other locations (ORR-MFE1) Helium accumulation fluence monitors were also included and are being analyzed at Rockwell International (RI) by H. Farrar IV and D. Kneff. More complete results of the spectral analysis have been forwarded to E. Bloom (ORNL) and many DAFS and ADIP Task Group members. Copies are available on request. Table 1-4 lists damage parameters for a year-long irradiation in ORR, similar to the MFE experiments now in progress.

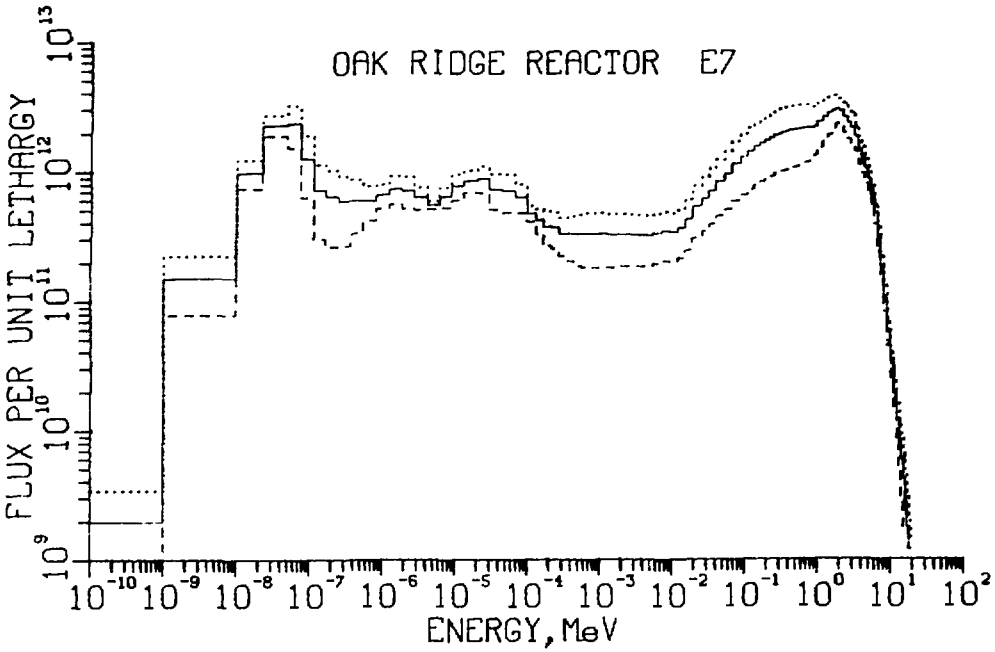

Figure 1-26. STAYSL results for the Oak Ridge Research Reactor. Twenty-one reactions were measured in core location E7 at a reduced power of 1 MW. Differential flux times neutron energy is plotted. The dashed lines represent one standard deviation errors.

Table 1-3. ORR-LP-MFE2A-E7. Comparison of ANL Group Fluxes with Neutronics Calculations (results normalized to 30 MW)

Lower Energy MeV	Group Flux (10^{13} n/cm^2-s)					
	Row 22			Row 9		
	ANL	Calc.*	Ratio ANL/Calc.	ANL	Calc.*	Ratio ANL/Calc.
1×10^{-10}	16.1	28.5	0.56 ± .03	7.3	10.9	0.67 ± .03
5.5×10^{-7}	5.4	6.9	0.78 ± .08	2.4	2.8	0.86 ± .09
9.2×10^{-6}	8.3	11.3	0.73 ± .11	3.8	4.7	0.81 ± .12
1.3×10^{-3}	2.1	5.7	0.37 ± .22	0.93	2.4	0.39 ± .23
1.2×10^{-2}	6.4	9.4	0.68 ± .41	2.7	3.9	0.69 ± .41
0.19	8.7	11.7	0.74 ± .19	3.6	4.9	0.73 ± .18
>0.92	13.2	14.7	0.90 ± .07	6.1	6.2	0.98 ± .07
Total	60.3	88.0	0.69 ± .10	27.0	35.8	0.75 ± .11

* Seven group, 3D calculations provided by T. Gabriel, ORNL (1979).

Table 1-4. Damage Parameters for ORR Calculated with STAYSL Flux Covariances

(The spectrum is shown in Fig. 1-26, although the power is renormalized to 30 MW)

Material	Damage (DPA/yr)	Helium (ppm/yr)
Ni	5.7 ± 0.6	22.6 ± 2.5[a]
Cu	5.5 ± 0.6	1.4 ± 0.2
Nb	5.4 ± 0.6	0.31 ± 0.04
Au	4.4 ± 0.4	0.0030 ± 0.0005

[a] $^{58}Ni(n,\gamma)^{59}Ni(n,\alpha)$ process not included.

1.3.1.2 Fission Reactor Dosimetry at ORR-MFE 1 Experiment

Preliminary results are available for the ORR-MFE 1 experiment. The irradiation was conducted in core position C7 between February 13, 1978 and June 28, 1978. The average power level was 22.52 MW over the total time of 134.7 days; however, the reactor was down for about 25 days during this period. Gamma heating problems early in the run necessitated some changes in the core configuration producing steep fast flux gradients across the experimental package.

Four dosimetry wires (Ni, Co-Al, Ti, and Fe) were placed in four aluminum tubes at the four corners of the 24" long irradiation capsule. One of the four aluminum tubes also contained 107 small helium accumulation fluence monitors (HAFM) which are now being analyzed by H. Farrar IV, of Rockwell International.

Six dosimetry reactions were analyzed at twelve locations for each group of four wires by cutting each wire into one inch long segments and Ge(Li) counting every other piece. The reactions which were analyzed included $^{54}Fe(n,p)^{54}Mn$, $^{58}Fe(n,\gamma)^{59}Fe$, $^{58}Ni(n,p)^{58}Co$, $^{60}Ni(n,p)^{60}Co$, $^{59}Co(n,\gamma)^{60}Co$, and $^{46}Ti(n,p)^{46}Sc$. Calculations show that thermal burn-up corrections are severe for ^{58}Co; measurements indicate a 60% reduction in ^{58}Co in the highest flux regions. The $^{60}Ni(n,p)^{60}Co$ reaction also cannot be used for flux determinations due to the $^{58}Ni(n,p)^{58}Co$ (n,γ) $^{59}Co(n,\gamma)^{60}Co$ reaction mechanism.

The fluence results for the highest flux region ($\sim$ 3" below midplane) are listed in Table 1-5. As can be seen, the results are distinctly different from the low-power, spectral irradiation reported previously. In particular, the following measurements should be noted:

1. The fast flux (> .92 MeV) decreases sharply ($\sim$ 40%) from South (towards core center) to North! Only a 10% change was measured in core position E7.

Table 1-5. Flux Measurements for ORR-MFE 1

Flux × 10^{14} n/cm^2/s
Average Power Level = 22.5 MW
For fluence, multiply by 1.164 × 10^7 s
Core Location C7.

Energy Region	Core Position[a]				Neutronics[b] Calculation	
	SW	SE	NE	NW	S	N
Thermal	1.60	1.68	1.60	1.64	1.8	1.8
> .92 MeV	0.66	0.62	0.39	0.39	0.80	0.52
Total (estimated)	4.3	4.2	3.4	3.5	4.9	4.0

[a]SW stands for Southwest; the South side is closest to the center of the core.

[b]Values scaled to 22.5 MW from calculations by T. Gabriel, ORNL (1979).

2. The thermal flux is nearly isotropic, differing by less than 5% among the four corners of the capsule at each row.

3. The thermal-to-fast flux ratio changes from about 2.4 on the South side to about 4.0 on the North side, whereas the low-power results gave a ratio of only 1.2! Neutronics calculations predict a ratio of 4.2 for the center of C7.

4. The total flux is about 15% lower than neutronics calculations, although the spectrum is reasonably similar.

5. Neutronics calculations appear to seriously overpredict the flux below midplane, probably due to streaming effects.

These results have some serious implications for materials studies in the MFE 1 experiment. First of all, the steep flux gradient from South-to-North was not anticipated and was not seen in core position E7 or neutronics calculations. This gradient increases the uncertainty of damage calculations since the exact specimen location is now very important. The spectrum also appears to change with position and does not agree with our low-power spectral measurement. Since part of the spectrum ($\sim$ 1-500 keV) cannot be easily measured on long irradiations, an additional uncertainty will be added to damage parameters. Reasons for these differences are now being explored and complete flux and damage maps will be available shortly.

Analysis of the dosimetry results for ORR-MFE 1 will be completed during the next quarter. The foil measurements will be integrated with helium measurements now being done by H. Farrar IV (Rockwell International). Fluence and damage maps will be generated covering all experimental locations.

A paper including our work in the Oak Ridge Research Reactor will be presented at the Third ASTM-EURATOM Symposium on Reactor Dosimetry, October 1-5, 1979 in Ispra, Italy. The paper is entitled, "Status of Current, Routine Dosimetry at Existing Irradiation Facilities: Flux-Spectrum Mapping at ORR, RTNSII, and U. C. Davis Facilities."

1.3.1.3 Development of the STAYSL Computer Code

The STAYSL code written by F. G. Perey (ORNL) is now operational at Argonne. We have developed procedures for adding covariance errors for routine dosimetric applications. In order to take advantage of our previously developed cross-section and associated error files, as well as cadmium cover and neutron self-shielding programs, the input to STAYSL has been modified to be compatible with our Monte Carlo code SANDANL.

There are three types of uncertainty in the input data used for flux-spectral analysis, namely, activation errors, nuclear cross-section errors, and input flux errors. In addition to this, covariance errors must be specified for all related parameters. The STAYSL code then uses a least-squares technique to find the minimum value of χ^2 for the output flux-spectrum which best fits the input data. At present, only activation errors can be treated rigorously. Errors due to counting uncertainties, detector calibration, and nuclear data are typically less than 2% and covariance effects are negligible.

Nuclear cross-section errors and covariances can in principle be deduced from the available experimental data and such files will be published in ENDF/B-V. In the meantime, we will continue to use our cross-section error files derived from W. N. McElroy *et al*, extended to 44 MeV as required for high energy dosimetry. Table 1-6 compares our cross-section error estimates with the results of integral testing in Be(d,n) fields. As can be seen, our error estimates tend to be conservatively large.

Input flux errors are unfortunately the most difficult to define. For example, the reactor neutronics calculations used as input generally have no error estimates available. Consequently, we have somewhat arbitrarily assigned flux errors on the basis of integral data testing and our past experience. Sensitivity studies have been done to assess the importance of these error assignments. In regions of good, overlapping foil coverage, increasing the input flux errors will only increase the output flux errors up to a point where no further effect is seen. This procedure can be used to determine maximum error limits if no other guidance is available. However, in regions of poor foil coverage, this procedure will fail and one must rely on past experience.

Flux and cross-section self-covariances have been estimated using a Gaussian function with a full width of several energy groups. In other words, we are saying that nearby groups must be very strongly correlated; however, widely spaced groups are almost entirely independent. This statement is analogous to smoothing the iteration in SAND II and also avoids the problem of discontinuities in the output flux spectrum, especially at sharp resonances in the cross-section, which are not physical. Covariances between different cross-sections must be determined from experimental data and we must wait for their publication in ENDF/B-V.

Table 1-6 Comparison of Estimated Cross Section Errors with Integral Test Results for Be(d,n), E_d = 14 - 40 MeV.

The 90% energy sensitivity limits are given.

Reaction	Energy Range (MeV)	Estimated Range of Errors (±%)	Measured Integral Errors (±%)
$^{115}In(n,n')^{115m}In$	2 - 23	8 - 20	3
$^{238}U(n,f)$	2 - 30	6 - 15	4
$Ti(n,p)^{46}Sc$	5 - 33	15 - 50	14
$Ti(n,p)^{47}Sc$	3 - 33	15 - 50	15
$^{48}Ti(n,p)^{48}Sc$	7 - 27	15 - 50	7
$Fe(n,p)^{54}Mn$	4 - 33	10 - 40	6
$^{56}Fe(n,p)^{56}Mn$	6 - 23	10 - 30	4
$^{59}Co(n,p)^{59}Fe$	5 - 24	10 - 40	8
$^{58}Ni(n,p)^{58}Co$	4 - 23	6 - 30	9
$^{60}Ni(n,p)^{60}Co$	6 - 23	10 - 40	14
$^{27}Al(n,\alpha)^{24}Na$	7 - 21	6 - 15	3
$^{54}Fe(n,\alpha)^{51}Cr$	6 - 28	15 - 40	36
$^{59}Co(n,\alpha)^{56}Mn$	7 - 24	10 - 40	4
$^{45}Sc(n,2n)^{44m}Sc$	13 - 27	10 - 20	14
$^{58}Ni(n,2n)^{57}Ni$	14 - 28	20 - 30	14
$^{59}Co(n,2n)^{58}Co$	12 - 27	10 - 20	9
$^{59}Co(n,3n)^{57}Co$	22 - 36	20 - 40	28
$Zr(n,2n)^{89}Zr$	13 - 28	15 - 30	13
$^{93}Nb(n,2n)^{92m}Nb$	10 - 22	10 - 20	7
$^{169}Tm(n,2n)^{168}Tm$	10 - 23	10 - 20	7
$^{169}Tm(n,3n)^{167}Tm$	18 - 30	10 - 30	9
$^{197}Au(n,2n)^{196}Au$	9 - 24	10 - 20	9
$^{197}Au(n,3n)^{195}Au$	18 - 29	10 - 30	6
$^{197}Au(n,4n)^{194}Au$	27 - 40	15 - 30	11
$^{238}U(n,2n)^{237}U$	7 - 16	20 - 40	11

So far, our experience with STAYSL is generally similar to the results obtained with SANDANL. In both cases, the input flux uncertainties strongly dominate the output flux uncertainties. The STAYSL code treats input flux errors more realistically since our perturbation procedures in SANDANL produce non-physical, long-term correlations. Output flux errors thus appear to be more physically reasonable in STAYSL.

Figure 1-26 shows a flux spectrum determined at the Oak Ridge Research Reactor (ORR) at a reduced power of 1 MW. The output flux covariance file from STAYSL has also been interfaced with our damage parameter codes and Table 1-4 lists calculated damage rates and errors for the ORR spectrum shown in Fig. 1-26.

We intend to use the STAYSL code for most routine fusion dosimetry. As new cross-section variance-covariance files are published in ENDF/B-V, they will be tested and incorporated into the code. A paper has been written concerning this work entitled "Uncertainties and Covariances of Spectra Derived from Integral Measurements" for presentation at the Third ASTM-EURATOM Symposium on Reactor Dosimetry, Ispra, Italy, October 1-5, 1979.

1.3.2 Damage Analysis

L. R. Greenwood, Chemical Engineering Division

A meeting of the Damage and Fundamental Studies Subtask Group B was held at Lawrence Livermore Laboratory on June 7-8, 1979. Our program to calculate displacement damage parameters was presented and compared to other existing codes at HEDL, ORNL, BNL, LLL, and LASL. All codes were found to generally agree within nuclear cross section uncertainties. Since our files are the most complete (21 elements) and are the only calculations above 20 MeV for 6 elements, it was recommended that our data files and programs be adopted for routine dosimetry applications. We have already been providing this service upon request from OFE experimenters.

Our displacement damage files and spectral averaging computer program SPECTER have been sent to Lawrence Livermore Laboratory for inclusion on the National MFE Computer Network. The data is now being compared to other existing damage libraries.

1.3.3 Cross Section Measurements, Evaluation and Techniques

P. T. Guenther, A. B. Smith, D. L. Smith and J. F. Whalen, Applied Physics Division and R. Howerton*

Neutron total and scattering cross sections of elemental bismuth were measured to energies of approximately 4.5 MeV. The experimental results were used to deduce an optical-statistical model that is quantitatively descriptive of the measured values and of higher-energy results reported in the literature. The measured and calculated values, together with the body of information available in the literature, were utilized to derive a comprehensive evaluated nuclear-data file in the ENDF format. This evaluation extended from 10^{-5} eV to 20 MeV, addressed neutron induced and photon-emission processes and was oriented toward the needs of fusion-fission-hybrid and electro-nuclear breeding applications.

---

*Lawrence Livermore Laboratory, Livermore, California

1.3.4 Radiation Damage in Diagnostic Windows for the TFTR*

William Primak, Solid State Science Division

Tasks in progress during this period have been the determination of the luminescence of sapphire suitable for windows, the effect of 14-MeV neutrons on the density of vitreous silica, the determination of the effect of intense ionization in thin layers on internal stress of vitreous silica, and the examination of vitreous silica exposed in PLT.

A sample of vitreous silica exposed in PLT was examined for strain birefringence. The birefringence observed corresponded to several hours exposure to X-rays from a commercial soft X-ray tube. The effect could not be accounted for by the radiation which we were advised had been present in PLT during this period. A second sample was to have been exposed, but apparently this has not yet been accomplished. Fragments of a broken diagnostic window from PLT have been received for examination, but information for handling this task has not yet been received.

Samples of vitreous silica for exposure in RTNS-II (14-MeV neutrons) were packaged in December 1978 and sent for irradiation. These were to have been irradiated in January, 1979 and returned to us for measurement in February, 1979. Operating difficulties at RTNS-II delayed the irradiation. The irradiated package was received in late October, 1979, in a damaged condition; it had been permitted to come in contact with the rotor and at least one of the samples had been abraided by the rotor.

An electron bombardment machine capable of providing the high ionization doses to be encountered in the TFTR in reasonably short times (10^{13} R in a few hours or a few days depending on the current densities desired) was assembled. In the first test, a plate of vitreous silica was bombarded with 11-KeV electrons and the strain birefringence was measured after various doses up to 2×10^5 megaR. The negative dilation calculated from the strain birefringence corresponded closely to the dilation calculated from the formula which we had developed many years ago in similar experiments with 0.6- and 0.3-MeV electrons.[16] In the second test, a 0.6 cm^2 area of a 1.973 cm^2 disc of commercial vitreous silica was bombarded with 18-keV electrons. The original disc showed a weak strain birefringence pattern, (this is typical for commercial vitreous silica) and this was modified slightly, particularly near the edge of the bombarded area. The plate had been coated with silver prior to bombardment to provide a path to ground for the incident charge. The thickness of the coating was 483 A. The residual energy was 17.6 keV corresponding to a residual range in vitreous silica of 1.38 μ. A scratch and a few spots were visible by schlieren after bombardment, but it is not certain that they may not have been caused by handling. In the interferometer, a deformation of 0.1 to 0.2 fringes (a fringe is 0.273 μ) was seen. This corresponds to a 3% vertical collapse.

* The luminescence study was done in collaboration with P. Yuster and C. Delbecq. Emmet Monahan assisted in the electron bombardment studies.

Since the radiation-induced negative dilation is about 3%, this corresponds to a plastic flow stress relaxation in which the whole dilation is experienced perpendicularly to the surface. This phenomenon has been observed in ion bombardment of silica,[17] but it is the first time it has been reported for electron bombardment. The problem now is to observe the effects when thicker layers are irradiated; in ion bombardment they exhibit a surface crazing.

Determination of the luminescence of sapphire had been scheduled for June, 1979, but the samples from one of the vendors did not arrive until late September, 1979. Two samples, one from Crystal Systems (CS) and the other from Union Carbide (UC), were subjected to x-irradiation; and the luminescence spectra were determined with scanning nonochromators. The samples were then transferred to the electron bombardment machine and the luminescent output was measured in significant parts of the spectra with a photodetector and filters. The arrangements were then calibrated with photometric sources to obtain the absolute intensity of the luminescence and the luminescent efficiency. Vitreous silica was run for comparison. The results are summarized in Table 1-7. The two materials were quite different. The CS material had a strong band at 0.41 μ while the UC material had a much weaker band below 0.3 μ. Both materials luminesced at the ruby line, 0.7 μ, and both showed side bands in this region. The ruby line was much more intense in the UC material. In the CS material the intensity in the ruby line was much less relative to the side bands. After this work was completed, a sapphire sample from Meller was lent to us and examined visually under X-ray irradiation. Its behavior was quite different from either of the other samples examined. The CS material appeared blue, the UC material appeared red, the Meller material appeared bluish-red and, in addition, displayed a long after-glow. Since the luminescence is caused by impurity or imperfections in the crystal, it is recommended that the particular plate to be used be inspected prior to fabrication.

Table 1-7. Luminescence

Sample Nos. Material Source	4047,4054 Sapphire (UCC)	4048 Sapphire (CS)	4049 Silica (Suprasil)
Absorbed X-rays (w/cm^2)	5.16×10^{-4}	5.16×10^{-4}	4.98×10^{-4}
X-ray luminescence[a] (w/cm^2)			
Ruby line	1.14×10^{-8}		
Side bands	1.05×10^{-8}	1.02×10^{-9}	
Total	2.19×10^{-8}	1.02×10^{-9}	
LE (w_{light}/w_{ioniz})	4.24×10^{-5}	1.97×10^{-6}	
F-band (w/cm^2)		1.14×10^{-7}	
LE (w/w)		2.21×10^{-4}	
UV peaks (w/cm^2)			
0.251 μ	8.9×10^{-9}		
0.34 μ (tail to 0.6 μ)			1.2×10^{-11}
0.6 to 0.72 μ			1.37×10^{-11}
Absorbed electrons, low current (w/cm^2)	3.54×10^{-2}	0.35	2
Red light (w/cm^2)	5.71×10^{-7}	4.49×10^{-8}	
LE (w/w)	1.61×10^{-5}	1.27×10^{-7}	
Blue light (w/cm^2)		1.9×10^{-6}	
LE (w/w)		[b] 1.12×10^{-6}	
No filter (0.3 μ- ?)(w/cm^2)			6×10^{-10}
LE (w/w)			2.9×10^{-10}
Red filter (w/cm^2)			2.5×10^{-11}
LE (w/w)			1.3×10^{-11}

[a] Corrected for increase caused by silvering

[b] Luminescent Efficiency (LE) is reduced by over an order of magnitude by an exposure of several minutes at 400 megaR/sec (i.e., $\sim 10^5$ megaR).

REFERENCES

1. V. K. Sethi and F. V. Nolfi, Jr., DAFS Quarterly Progress Report for Period Ending December 31, 1978, p. 202.

2. V. K. Sethi and F. V. Nolfi, Jr., DAFS Quarterly Progress Report for Period Ending December 31, 1978, p. 103.

3. V. K. Sethi, A. P. L. Turner, and F. V. Nolfi, Jr., DAFS Quarterly Progress Report for Period Ending September 30, 1978, p. 192.

4. S. K. Das, M. Kaminsky, R. Tishler, and J. Lecchi, J. Nucl. Mat. (1979).

5. L. H. Rovner and K. Y. Chen, J. Nucl. Mat. 63, 307 (1976).

6. A. S. Rao and D. J. Bacon, Electron Microscopy and Analysis, Int. Phys. Conf. Series No. 36, p. 215 (1977).

7. S. Veprek, A. Portmann, A. P. Webb, and H. Steussi, Rad. Effects 34, p. 183 (1977).

8. T. Rossing, M. Kaminsky, and S. K. Das, J. Nucl. Mat. 63, 325 (1976).

9. K. Sone, M. Suidoh, R. Yamada, and H. Ohtsuda, J. Nucl. Mat. 76, pp. 2-10, (1978).

10. J. W. Gadzuk, Surf. Sci. 6 (1967) 133.

11. R. L. Gerlach and T. N. Rhodin, Surf. Sci. 19 (1970) 403.

12. A. R. Krauss and D. M. Gruen, Proc. First Top. Conf. Fusion Reactor Materials, Miami Beach, Florida, January 1979. To be pub. J. Nucl. Mat.

13. M. Lagues, Surf. Sci. 45 (1974) 432.

14. C. R. Helms and K. Y. Yu, J. Vac. Sci, Technol. 12, 276 (1975).

15. Yee S. Ngi, T. T. Tsong, and S. B. McClane, Jr., Phys. Rev. Lett. 42, 588 (1979).

16. W. Primak and R. Kampwirth, J. Appl. Physics, 39, 5651 (1968); W. Primak, J. Appl. Physics, 49, 2572 (1978).

17. W. Primak, Phys. Rev. B14, 4579 (1976).

2.0 STARFIRE - A COMMERCIAL TOKAMAK REACTOR DESIGN STUDY

2.1 Introduction

STARFIRE Design Group

The basic objective of the STARFIRE project is to develop a design concept for a commercial tokamak fusion electric power plant based on the deuterium/tritium/lithium fuel cycle. The key technical objective is to develop the best embodiment of the tokamak as a power reactor consistent with credible engineering solutions to design problems. Another key goal of the project is to give careful attention to the safety and environmental features of a commercial fusion reactor.

This project was initiated in May, 1979, with the goal of completing the design study by October, 1980. The major emphasis of activities during FY 1979 has been to develop and compare options for key reactor design features. The plan is to select a set of reference parameters and major design features early in FY 1980 to provide a basis for an in-depth reactor and plant design during the rest of FY 1980.

Advisory committees for STARFIRE have been established in two key areas. The first is a Utility Advisory Committee whose purpose is to provide input from the utility perspective on commercial fusion power plants and to provide a mechanism for utility review of the design as it develops. Because of the importance of carefully considering the safety and environmental aspects of STARFIRE, a safety review committee has been established. This committee's primary purpose is to provide review and recommendations for the development of the reactor and plant conceptual design.

The basic design guidelines for STARFIRE assume the successful operation of a tokamak engineering test facility (ETF) and a demonstration power plant. STARFIRE is considered to be the tenth plant in a series of commercial reactors. It is, therefore, assumed that a well established vendor industry exists and that utilities have gained experience with the operation of fusion plants.

The major areas of design emphasis in FY 1979 include developing plasma engineering characteristics of STARFIRE and selecting a reference blanket concept. The basic size of the reactor is determined by selecting the net power output and the first wall power loading. The net electric power output has been selected to be about 1150 MW(e). The first wall loading depends on the particular blanket concept and is in the range of 2-4 MW/m^2. This results in reactor major radii in the range of 8 to 6 m. The toroidal magnetic field requirements are established by considering the plasma β and any toroidal field margin required for impurity and alpha particle control. The β limits have been taken to be generally consistent with those being adopted for ETF and INTOR.

A major feature under consideration for STARFIRE is a steady-state operating mode based on a continuous plasma current drive. At this point, an rf lower hybrid current drive option has received the most attention. The potential advantages of steady-state reactor operation are numerous.

In particular, such an operating mode is expected to greatly improve the overall reliability of the reactor. Based on the current theory, it is believed that a steady-state operating mode is possible, but there is at present very little experimental verification.

Availability goals have been established as 85% for the reactor and 75% for the complete plant including the reactor. These goals provide a basis for design of maintenance equipment. The maintenance scenario incorporates the current utility practice of shutting down annually for one month and a four month shutdown approximately every 5-10 years.

An important design consideration is the choice of the plasma impurity and alpha particle removal concept. Several schemes have been considered including a limiter/vacuum pumping system, various types of divertors, gas puffing and plasma boundary flows, and additional margin in the toroidal magnetic field. Initial investigations indicate that modest pumping of helium with a limiter pumping system ($\sim$ 15% of the alpha particle flux) coupled with about a 1.5 T margin in the maximum toroidal field may eliminate the need for a divertor, providing that a significant portion of the alpha particle energy can be radiated to the first wall rather than be deposited on the limiter. With respect to divertor options, particular attention is being given to developments for INTOR and ETF. In general, a nondivertor option is greatly preferred from an overall reactor engineering point of view.

Another key design consideration is the location of the equilibrium field (EF) coils. The basic design approach is to locate almost all the EF coils outside of the toroidal field (TF) coils; all such EF coils would be superconducting. A limited number of segmented coils would be located inside the TF coils, but outside of the blanket and shield.

Safety has played a major role in considering various blanket options. In particular, efforts are being made to minimize the tritium inventory and the radioactivity induced in the materials in the reactor.

2.2 Overview of the Reference Design

A preliminary reference design has been identified for STARFIRE to serve as a focal point for the design trade studies. The design is modified as new requirements or trade study results are defined. The selection of the major parameters for the preliminary reference design point evolved from extensive system and trade-off studies as summarized below.

2.2.1 Design Point Selection

Previous fusion reactor design and systems studies have demonstrated the presence of a wide range of design parameters and a diversity of design concepts. A primary goal of the STARFIRE study is to select, based on present knowledge, the most attractive set of design parameters and concepts that make tokamaks economically competitive and environmentally acceptable. In addition to experience gained from design and systems studies in the United

States and worldwide, extensive tradeoff analyses were carried out to guide the selection process for STARFIRE. A primary tool for these tradeoff studies is a comprehensive systems computer program that is capable of predicting the performance characteristics and economics of the entire tokamak power plant.

The major design parameters that characterize a tokamak reactor are the reactor power, the neutron wall load, aspect ratio, plasma elongation, major radius, plasma beta, magnetic field, scrape-off region thickness, and blanket/shield thickness. A brief review of the considerations that were factored into selection of these major parameters is presented below.

Reactor Power

It has been shown that tokamak reactors exhibit an economy of scale; i.e. larger power reactors have lower cost of energy. However, three considerations important to the utilities limit the desirable power rating of a plant. The first is the difficulty of raising the capital for larger power plants. The second relates to the cost of reserve electric power capacity that the utility must provide to compensate for scheduled and unscheduled outages. The cost of reserve capacity increases with the size of the individual power plant. The third is the maximum capacity of a single turbine generator. Based on recommendations by the Utility Advisory Committee for STARFIRE, the most desirable power rating at present is in the range of 3000-4000 MW for thermal power and $\sim$ 1250 MW for electrical power. Therefore, the fusion power for STARFIRE was selected as 3200 MW. This corresponds to a nominal thermal power of $\sim$ 3800 MW, based on a 21 MeV per fusion reaction, and a net electric power of $\sim$ 1150 MW. The recoverable thermal power will be modified by the addition of rf power for current drive and the loss of low temperature heat such as that in the limiter system.

Neutron Wall Load and Structure Life

A key parameter that has a substantial impact on the physical size of the reactor is the neutron wall load (P_{MW}). For the same fusion power, a higher P_{nw} results in a smaller surface area, higher power density, smaller reactor volume and potentially lower cost. This underlines the motivation for developing designs with higher wall loads.

There are limitations, however, on the ability to produce and use high wall loads. The upper limits on the use of high wall loads are dictated primarily by the first-wall cooling capability and the structure lifetime. Constraints such as the maximum operating temperature and thermal stresses place an upper-bound on the allowable wall load. For typical structural materials such as ferritic steels in pulsed reactor systems, the neutron wall load should be limited to $\sim$ 2.5 MW/m^2 for helium coolant. Higher wall loads are possible with water and lithium coolants. In general, the maximum allowable wall load is higher for steady-state reactors.

For a given fluence lifetime, the neutron wall load should be limited so that the frequency of structure replacement is not excessive. In order to limit the fractional increase in the cost of energy due to the plant downtime

for replacement of the structural material to δ, the structure lifetime must be sufficiently long to satisfy the following inequality:[1]

$$t_w > \frac{t_d}{365\delta} ,$$

where t_w is the structure lifetime in years and t_d is the total cumulative downtime in days for replacement of the structural material. For example, in order to limit the increase in the cost of energy to 10% (i.e. $\delta = 0.1$) when the downtime is 125 days the structure lifetime must be greater than 3.4 yr.

For a given structural material and a fluence lifetime, the loss of energy production resulting from choosing high P_{nw} and short t_w must be weighed against the economic gain realized by designing a small size reactor. Figure 2-1 shows the cost of energy as a function of the neutron wall load at two values of the integral neutron wall load, I_w, of 5 and 20 MW-yr/m^2 and at two different values for the total cumulative downtime, t_d, for replacement of the structural material. For I_w = 5 MW-yr/m^2 and downtime

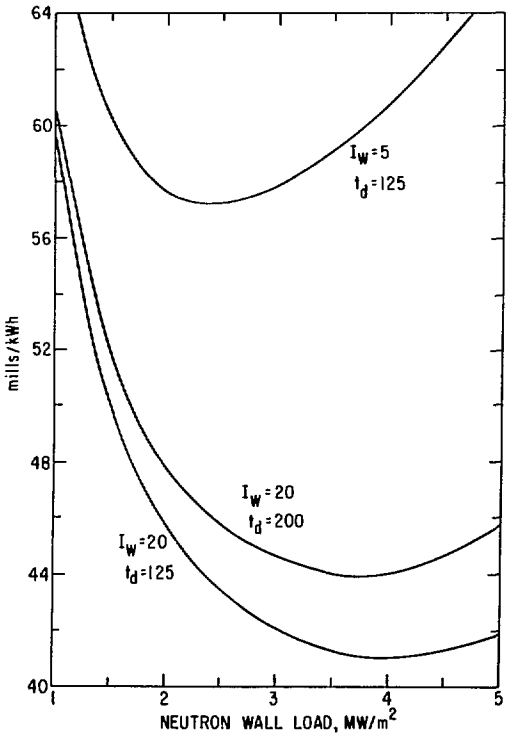

Figure 2-1. Cost of energy as a function of neutron wall load. I_w is the integral neutron wall load in MW-yr/m^2 and t_d is the total downtime in days for replacement of the structural material. Results are based on fusion power of 3200 MW, aspect ratio of 3.6, plasma elongation of 1.6 and β_t = 0.067.

of 125 days the neutron wall load should be kept in the range 2-2.5 MW/m^2. For $L_w \sim 20$ MW-yr/m^2 the cost of energy decreases significantly as the neutron wall load is increased from 1 to 2 MW/m^2. A smaller, but significant saving in the cost of energy (COE) is realizable by increasing P_{nw} from 2 to 3 MW/m^2. A slight change in COE is noticeable in the range $P_{nw} \sim 3$-4 MW/m^2. The reasons for the modest increase in COE as P_{nw} is increased beyond ~ 4 MW/m^2 will become evident from discussions later in this section.

It is clear that the achievable lifetime of the structural material has a significant impact on the cost of energy. By eliminating short plasma pulses and designing STARFIRE for steady-state operation, it is anticipated that a fluence lifetime of 20 MW-yr/m^2 or greater is obtainable with selected candidate structural materials. There are several important advantages for such a long life: (a) the cost of energy is substantially reduced because of less frequent replacement and higher availability factor; (b) when the frequency of replacement is substantially reduced, the cost of energy becomes less sensitive to moderate variations in the downtime. This is quite important as it permits flexibility in the reactor design not available otherwise for designs driven primarily by the need for achieving very short downtime; (c) a less frequent replacement of the structural material results in a lower inventory of radioactive materials for which storage has to be provided. (It should be noted that even for the candidate structural materials with no long-term activation, adequate radioactive storage is necessary for two to five decades); and (d) the demand on material resources is less with longer life.

For a given fusion power, plasma elongation and aspect ratio, a higher wall load implies a higher plasma density, P_p. This varies as $P_p \sim \beta^2 B^4$. Since the plasma β is limited by stability considerations, a higher P_{nw} is obtainable only by providing a higher magnetic field. For $P_{nw} > 2$ MW/m^2 there is ~ 1 T increase in the required B_m for every 1 MW/m^2 increase in P_{nw}. The economically attractive range for P_{nw} of 3-4 MW/m^2 requires a maximum toroidal field in the range 10-12 T which is considered acceptable for STARFIRE design.

In light of the above considerations, a neutron wall load of 3.5 MW/m^2 has been selected for STARFIRE. This moderately high wall load appears to be a reasonable choice that makes it possible to design a relatively small size reactor without excessive requirements on first-wall cooling capability, maximum toroidal magnetic field, and frequency of structural material replacement.

Plasma Beta

Previous systems studies[2] have indicated significant economic benefits for operating at high average plasma toroidal beta, β_t. However, the maximum realizable β_t is limited by plasma stability considerations. Based on recent theoretical analysis, the relationship $\beta_t = 0.24/A$, where A is the aspect ratio, has been assumed for the STARFIRE study.

Plasma Elongation

The elongation ($\kappa = b/a$) of a D-shaped plasma has a significant impact on the plasma performance, the reactor design characteristics, and economics. In particular, at higher κ the achievable β_t is higher but the required EF

coil system becomes more complex and costly. Based on previous work, a value of $\kappa = 1.6$ was selected for STARFIRE. This is believed to be nearly the upper limit on elongation if the important design goal of locating most of the EF coils external to the TF coils is to be achievable.

Power Requirements for Current Drive

Since STARFIRE will operate in a steady-state mode, a particularly important aspect of the design is the mechanism for plasma current drive. Lower-hybrid rf is the selected option for current drive. An important impact of the current drive system on the reactor performance and economics is the electrical power requirements for this system. The dependence of the magnitude of this power for the rf system on key plasma and reactor design parameters is discussed below.

The theory of lower-hybrid wave-drive currents[3,4] indicates the ratio of rf power density to current density is proportional to the electron density. Thus, rf power is reduced by operating at higher plasma temperatures (lower densities for a fixed beta). However, as the plasma temperature increases above $\sim$ 10 keV, the fusion power density starts to decrease and the ratio of rf power to fusion power is a minimum in the range 15-18 keV. In surveying reactor operation at various temperatures, the desire to minimize rf power calls for considering temperatures above 10 keV, but larger toroidal fields needed to keep the total fusion power at 3200 MW must also be acknowledged at these higher temperatures.

In determining the dependence of reactor design on aspect ratio (A), for a fixed total power and wall load and for $\beta_t \propto A^{-1}$, the total current increases going to lower aspect ratio, while the major radius and plasma density decrease. Based on the analytic formula[4]

$$P_{rf} = C\, R\, \bar{n}_e I ,$$

the rf power required to drive reactors for a series of equilibria in the range $3 \leq A \leq 4$ was computed. The coefficient C is a function of the plasma profiles, spectral width, and degree of current penetration; for typical reactor parameters, and for both centrally peaked and surface current density profiles, the rf power increases by 30-50% if the aspect ratio is reduced from 4.0 to 3.0. Hence, large values of A are preferred from the rf power point of view.

Major Radius and Aspect Ratio

With the fusion power and neutron wall load selected, the surface area of the plasma is defined. For a given κ, the aspect ratio (A) or the major radius (R) should be selected in order to fully define the plasma geometry. At $P_{nw} = 3.5$ MW/m^2, the major radius increases from 6 m to $\sim$ 7.3 m if A is increased from 2.6 to 4.0.

The size of the reactor building, length of piping, etc. are strongly affected by the size of the reactor, in particular, by the value of R + a,

where a is the plasma minor radius. Notice that the variation of R + a as the aspect ratio is changed is less than the variation in R alone. Despite the reduction in the capital cost of several items sensitive to size when R is smaller, economic optimization does not necessarily favor the selection of minimum R. This is true for both pulsed and steady-state reactors although for different reasons.

For pulsed reactors, the optimum size is significantly affected by the central core radius, r_v. For a given magnetic field for the OH coil, decreasing r_v reduces the available volt-seconds and shortens the burn time resulting in a lower reactor electrical output.

For steady state reactors with no or very limited OH coils, the problem of the central core radius disappears. In this case, the plasma current has to be driven by external means. If the electrical power requirement for the current driver were negligibly small, then the smallest aspect ratio should be chosen so that the major radius is minimum, provided of course that there is adequate space on the inner side of the torus to accommodate the TF coils and support cylinder. This is illustrated by the case $P_{rf} = 0$ in Fig. 2-2 which displays the cost of energy as a function of the aspect ratio.

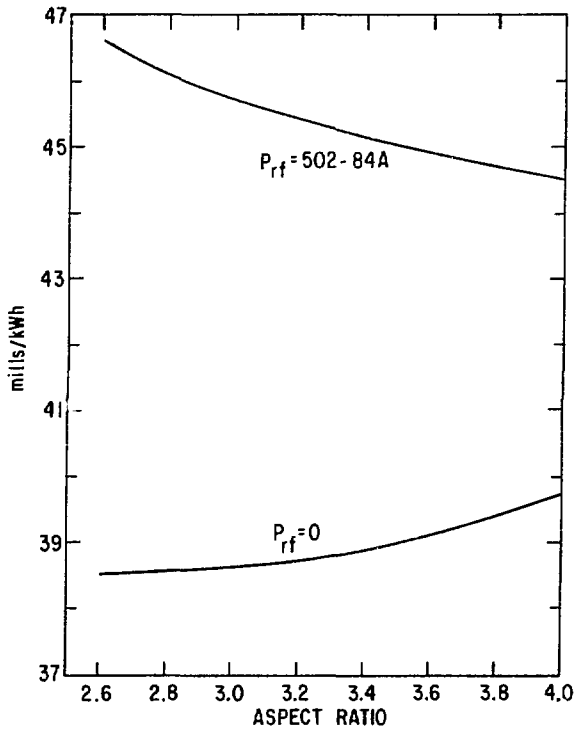

Figure 2-2. Cost of energy as a function of aspect ratio for a steady-state reactor in two cases for the electrical power, P_{rf}, required for the current-drive system: $P_{rf} = 0$ and $P_{rf} = 502-84A$ where A is the aspect ratio.

As discussed earlier in this section, the electrical power requirement, P_{rf}, for the rf current drive system appears to be relatively large and increases with lower aspect ratio. Figure 2-2 shows the dependence of the cost of energy on aspect ratio for the case where $P_{rf} = 502\text{-}84A$, with P_{rf} in MW electric. In this case the cost of energy decreases as A increases up to $A \sim 4$. It is anticipated, however, that as a result of further work the rf power requirements will be reduced significantly. This would reduce the optimum aspect ratio somewhat below A = 4. Therefore, A = 3.6 was adopted for STARFIRE. This results in a major radius R = 7 m. The maximum magnetic field required is nearly minimum at A = 3.6.

Inner Blanket/Shield Thickness

The thickness, Δ^i_{BS}, of the blanket and shield on the inner side of the torus, or more precisely the distance in midplane from the plasma side of the first wall to the location of the maximum toroidal magnetic field, has a substantial impact on the reactor size, the required strength of the magnetic field and reactor economics. A comprehensive investigation of the optimum value for Δ^i_{BS} has been carried out previously.[5] The details of this previous work will not be repeated here, but the results are briefly stated.

For a given P_f, P_{nw}, β_t, and major radius, the advantages of a smaller Δ^i_{BS} are 1) lower maximum magnetic field and 2) larger central core (OH) radius, r_v. In pulsed tokamaks, the impact of the value of Δ^i_{BS} on r_v is large and becomes critical for low P_f high P_{nw} designs. In a steady state tokamak with no OH solenoid, the primary incentive for reducing Δ^i_{BS} is to reduce the maximum magnetic field required.

On the other-hand, there are several penalties for making Δ^i_{BS} too small. The increase in the radiation field when Δ^i_{BS} is decreased results in a) increase in the resistivity of the stabilizer material and a need for increasing the amount of the stabilizer to satisfy the cryogenic stability requirements, b) a decrease in the critical current density of the superconductor necessitating the use of more superconductor, and c) an increase in the heat generation rate in the TF coil since the increase in the power requirements for the TF coil cryogenic system can be so large that the reactor net electrical power output is seriously reduced.

For the preliminary reference design of STARFIRE a value of $\Delta^i_{BS} = 1.2$ m was selected based on careful considerations of the above trade-offs. This value includes $\sim$ 25% void to account for the vacuum gap in the TF coil and the use of helium coolant in a portion of the inner blanket, if necessary. The shield consists of a combination of tungsten, boron carbide, lead and a structural material.

Outer Leg of the TF Coils

For a given major radius (R), plasma inner radius (a) and inner blanket/shield thickness (Δ^i_{BS}) the position of the inner leg of the TF coil is defined. In order to fully define the D-shape of the TF coil, the size of the vertical or horizontal bore must be selected. We will discuss this choice in terms of R_2, the major radius of the midpoint of the outer leg of the TF coil. R_2 is the sum of the major radius, first wall minor radius, outer

blanket/shield thickness (Δ^o_{BS}), clearance (Δ_c) in the midplane from the outer edge of the shield to the TF coil and half of the TF coil thickness. The choice of R_2 has a significant impact on many of the reactor characteristics and cost as discussed below.

With the reactor parameters previously defined in this section (R, a, Δ_v, B_m, Δ^i_{BS}) the only remaining parameters that affect R_2 are Δ^o_{BS} and Δ_c. The necessary value of Δ^o_{BS} varies with blanket and shield material and coolant choices. As a goal, the materials in the shield should be chosen to have inherently low long-lived radioactivity even if they are less efficient in radiation attenuation. For typical material choices, the required Δ^o_{BS} is $\sim$ 1.3 m and $\sim$ 1.8 m for blanket with water (or lithium) and helium coolants, respectively. The clearance from the outer edge of the shield to the TF coils is required for several engineering reasons; the most dominant of which is to accommodate the coolant manifolds. The required R_2 is $\sim$ 12 m for water or lithium coolants compared to $\sim$ 13 m necessary for helium coolants.

The economics analysis shows a substantial penalty for increasing R_2. The cost of energy increases by $\sim$ 3% for each additional meter increase in the value of R_2 beyond 12 m. The cause of this penalty is that the value of R_2 directly influences the size and weight of the TF coils and their support structure, the size of the reactor building, the length of the piping for the heat transport system, and the size of the externally located EF coils. For example, by increasing R_2 from 12 to 14 m, the ampere-turns and stored energy in the EF coils nearly double.

It sould be noted that in order to keep the field ripple at the plasma to an acceptable level, the value of R_2 should be greater than a certain minimum. The minimum value for R_2 is larger for a smaller number of TF coils. A relatively small number, 12, of TF coils has been chosen for STARFIRE to enhance reactor maintainability. This makes extending the TF coils as a means of satisfying the field ripple criteria economically unattractive. Therefore, the alternative of an imposed field-ripple correction system (e.g. saddle coils[6] or iron blocks[7] will be provided if necessary.

2.2.2 Reference Design Description

The reactor cross section is shown in Fig. 2-3 and the design and operating parameters are given in Tables 2-1 through 2-3.

The reactor magnet system design includes twelve 11 Tesla TF coils. The EF coil system includes 4 segmented copper coils inside the TF coils for plasma stability control, but most of the EF coils are superconducting and located outside the TF coils for plasma equilibrium. The plasma startup, heating and current drive is accomplished by a lower hybrid rf system. This system reduces the need for ohmic heating coils and minimizes the need for dielectric breaks in toroidal conductors. The shield incorporates dielectric breaks to prevent toroidal current flow and permit the EF coils that are located inside the TF coil to have adequate response time for plasma stability control.

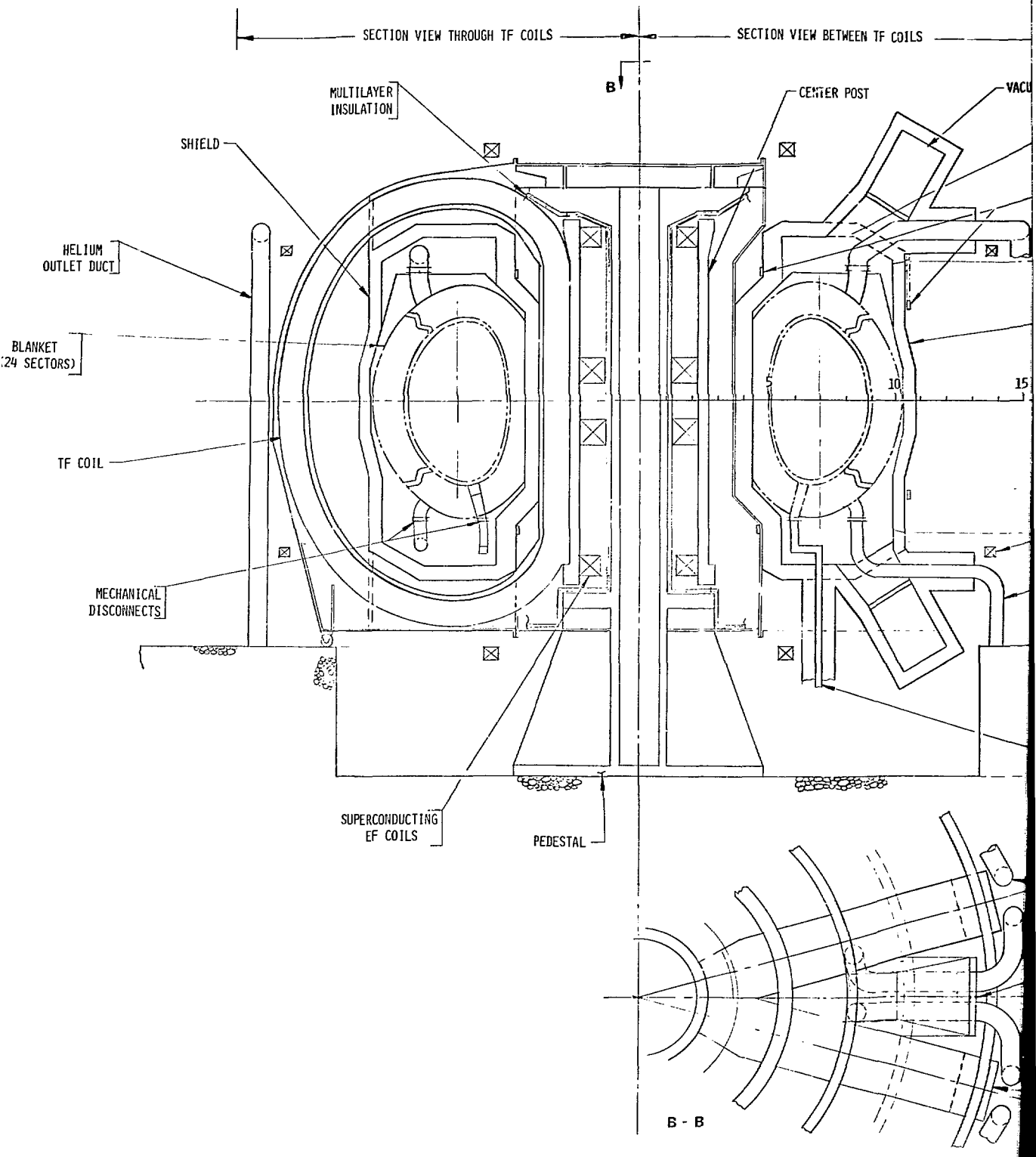
SECTION VIEW THROUGH TF COILS
SECTION VIEW BETWEEN TF COILS
B
MULTILAYER INSULATION
SHIELD
CENTER POST
VACU
HELIUM OUTLET DUCT
BLANKET (24 SECTORS)
10
15
TF COIL
MECHANICAL DISCONNECTS
SUPERCONDUCTING EF COILS
PEDESTAL
B - B

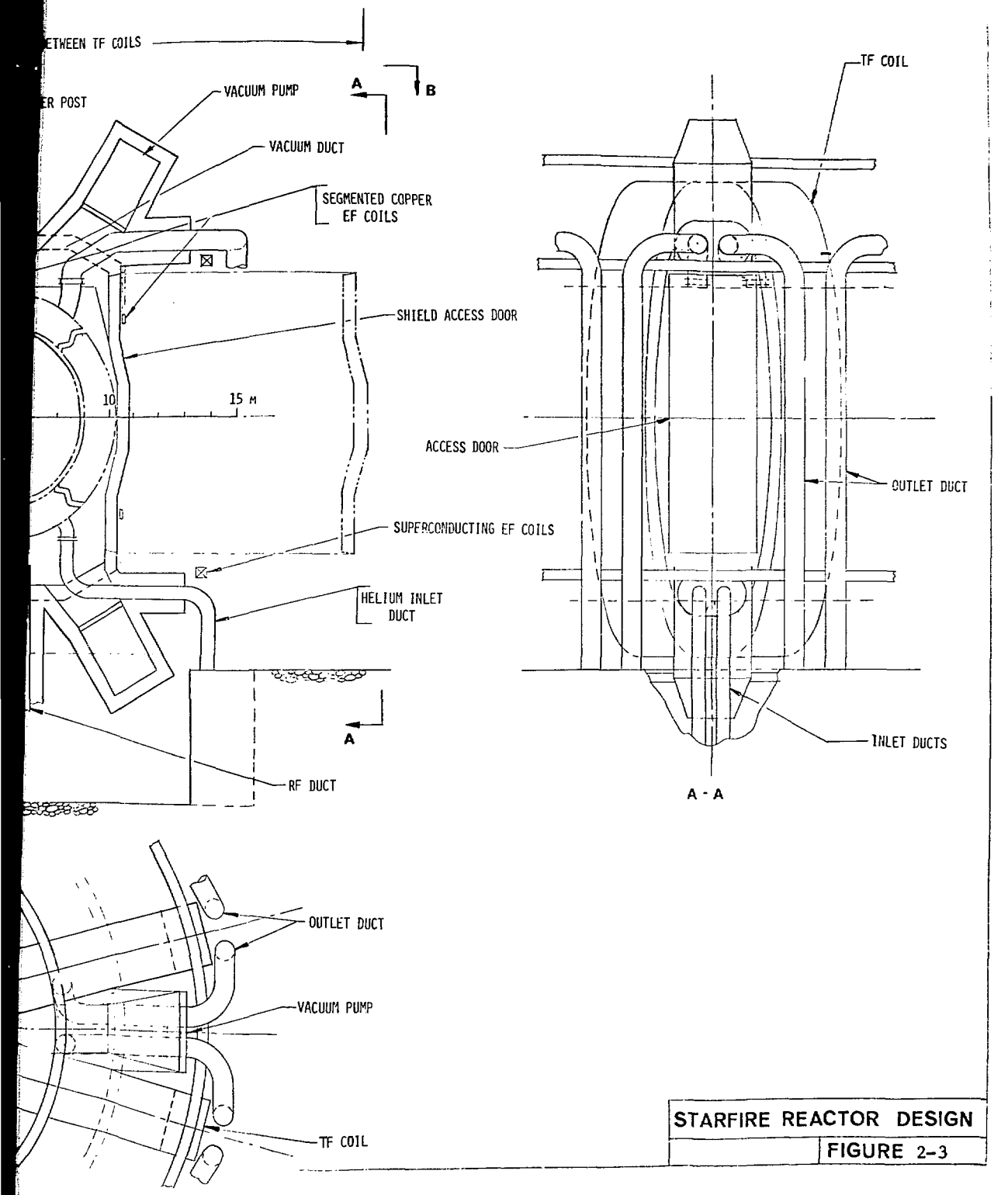

STARFIRE REACTOR DESIGN

FIGURE 2-3

Table 2-1. STARFIRE Major Design Features

Net electrical power	1150 MW
Gross electrical power	1600 MW
Fusion power	3200 MW
Thermal power (nominal)	3800 MW
Thermodynamic efficiency (gross)	41%
Thermodynamic efficiency (net)	30%
Overall availability	75%
Average neutron wall load	3.5 MW/m^2
Major radius	7.0 m
Plasma half-width	1.94 m
Plasma elongation (b/a)	1.6
Maximum toroidal field (nominal)	11.0 T
No. of TF coils	12
Plasma burn mode	Continuous
Current drive method	rf
Plasma heating method	rf
TF coils material	Nb_3Sn/NbTi/Cu/SS
Wall structural material	Ferritic steel
Blanket structural material	Ferritic steel
Wall coolant	D_2O
Tritium breeding medium	Li_2O
Blanket coolant	Helium
Plasma impurity control	Low-Z coating + limiter and vacuum system + enhanced radiation + field margin
Primary vacuum boundary	At inner edge of shield

Table 2-2. STARFIRE Impurity Control

Primary System
Low-Z coating
Limiter and vacuum system
TF margin to permit higher α and sputtered impurity concentrations
Enhanced radiation to reduce heat transport to limiter
Backup Option
Bundle divertor
(+ low-Z coating and enhanced radiation)
Major Parameters
Equilibrium impurity concentrations:
$N_\alpha/N_{DT} = 0.10$
$N_{Be}/N_{DT} = 0.04$
Effective reflection coefficient for He $\approx$ 0.70
Surface area of the limiter = $\lesssim$ 5% of first wall area
Heat transport power to limiter = 115 MW
Maximum power density to limiter $\lesssim$ 4 MW/m^2
Limiter coolant = water
TF field margin $\approx$ 1.5 T
Enhanced radiation material = Kr or Xe
Radiated power to first wall $\approx$ 650 MW

Table 2-3. STARFIRE Plasma Current Drive and Heating

Heating method	rf lower hybrid
Current drive method	rf lower hybrid
rf power to plasma	120 MW
Overall power efficiency	60%
Electrical power for rf	200 MW
Frequency, f	1.7
Index of refraction, $n_{\parallel}$	1.3-1.6
Waveguide area	35.9
rf intensity	0.3

The reactor shield is designed for life-of-plant and is not removed for normal maintenance operations. The shield concept is shown in Fig. 2-4. The reactor shield is water cooled and serves as the primary vacuum chamber. The shield protrudes between the TF coils at the top and bottom of the reactor to provide a vacuum duct to 24 cryosorption pumps. The vacuum duct opening through the shield is oversized to permit routing of coolant lines through the opening without significantly restricting pumping capacity. Each helium coolant line is shielded at the penetration through the shield by a bed of rods in a staggered pattern that limits neutron leakage. The shield contains poloidal dielectric breaks under every third TF coil. The dielectric joint, which is at the outside of the shield and completes the vacuum barrier, is exposed to about 10^{10} rads irradiation. The dielectric break will also be redundant and incorporate intermediate pumping. The shield pieces are designed to keep all seal welds between shield pieces in a single plane without welded corners, in order to improve reliability and simplify the installation operation. The shield doors utilize redundant Buna-N seals to provide the vacuum barrier. The seals are located near the outside of the shield; however, degradation by exposure to tritium and neutrons is expected to result in the need for seal replacement each time the door is removed during maintenance.

Impurity control is achieved by toroidal limiters located in front of the vacuum slots. High-Z gas puffing is used to enhance thermal radiation from the plasma which reduces the limiter heat load to 4 MW/m^2. As the plasma particles strike the limiter approximately 30% are directed to vacuum slots in the blanket where approximately all of those entering are pumped by the cryosorption pumps. The system extracts helium from the plasma at a rate which permits a continuous plasma burn. The limiter will be made of a high thermal conductivity material and will incorporate low temperature water cooling.

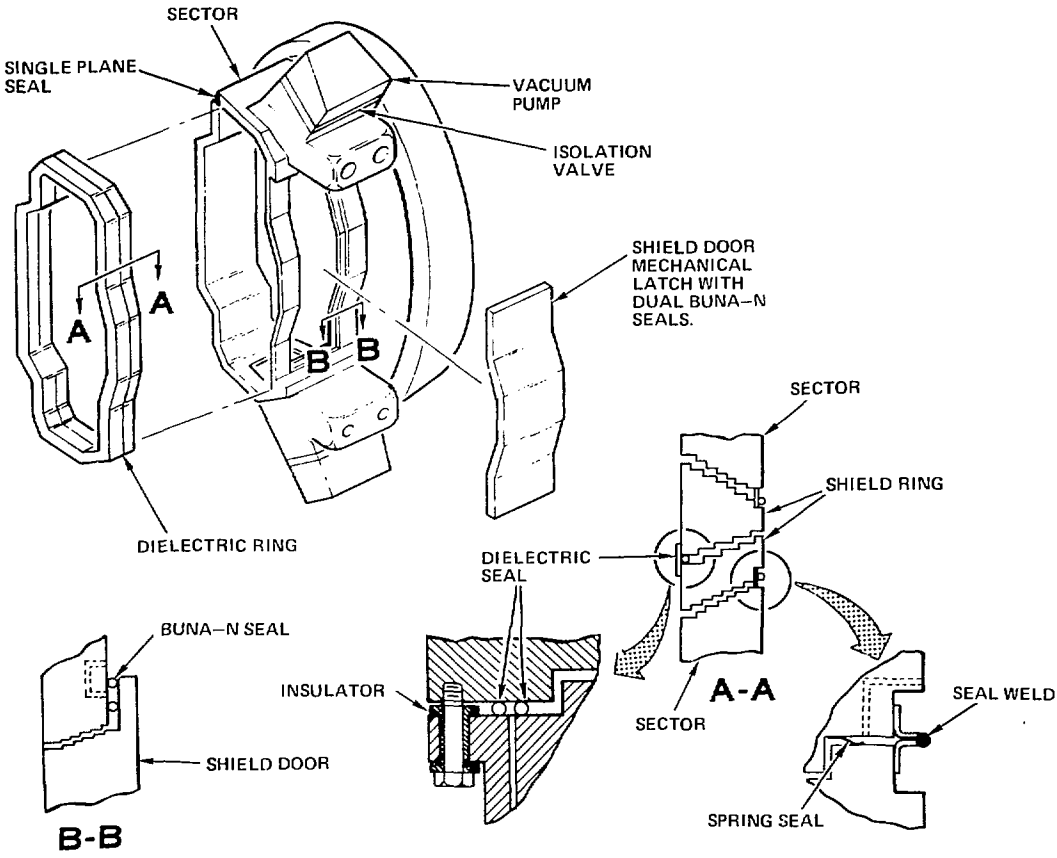

Figure 2-4. Shield design.

The blanket system is divided into 24 wedge shaped sectors to obtain a size that permits removal of sectors between TF coils. Each blanket sector incorporates an rf waveguide, two limiter segments, and two stepped toroidal slots 20 cm wide for vacuum pumping. Each sector is mounted on an air bearing pad to permit removal and replacement.

2.3 First-Wall/Blanket Considerations for STARFIRE

The technological and design aspects of various first-wall/blanket concepts have been considered in the selection of potentially viable designs for STARFIRE. The objectives of the present study involve identification of key technological constraints of candidate tritium-breeding-blanket design concepts, establishment of a basis for assessment and comparison of the critical problem areas and design features of each concept, and development of optimized

first-wall/blanket designs for STARFIRE. The major emphasis has been placed on the development of a blanket design that is safe and environmentally acceptable. The primary guidelines established to meet these criteria are low tritium inventory in the blanket, minimal long-lived activation products and minimal stored energy.

Since breeding of tritium is considered essential, and since lithium is the only viable tritium-breeding medium, lithium in some form is required in the blanket. On the basis of engineering and design considerations, liquid lithium provides many advantages for the tritium breeder; however, because of perceived safety problems associated with a liquid lithium system, the focus of the present study has been on the use of solid lithium compounds for breeding. The primary objective has been to assess the viability of a blanket design based on solid breeders. Technical evaluation of the safety problems associated with the liquid lithium system was not performed in the present study. Instead, reliance was placed on input from the Safety Advisory Committee for STARFIRE, based on limited safety analysis work performed previously. Likewise, the use of helium coolant has been the major focus of the present study because of its perceived safety advantages over other candidate coolants, viz., water and lithium. A major consideration in the selection of structural materials is the residual activation and the potential for reprocessing the material within one human generation, i.e. $\sim$ 20-50 years. This problem area impacts both radioactive storage and materials resource requirements.

2.3.1 First-Wall/Blanket Materials Options

Based on properties of the candidate materials (see Table 2-4), several combinations of coolant/breeder/structural materials result in potentially viable blanket design options. Lithium is the only breeding material considered with lithium coolant since there is no reason to use another breeding material if lithium is present in the system. Helium can be used with all of the breeding materials considered; however, Li_7Pb_2 is the least likely candidate because of the conflicting temperature requirements of this coolant/breeder system. Water coolant is not acceptable with lithium or Li_7Pb_2 because of safety considerations related to the high reactivity and the emission of hydrogen.

The most viable combinations of coolant/breeder/structure/neutron multiplier are given in Table 2-5. A design flexibility of different coolant and structure is considered acceptable for the first-wall and blanket if desirable. The reference blanket system is selected on the basis of perceived safety advantages associated with helium coolant and the solid breeding materials. Helium is selected only for the blanket coolant since water provides several advantages as the first-wall coolant. The ceramic breeding materials with their high temperature properties are most appropriate for the helium coolant. Lithium oxide is proposed as the breeding material since it is the only ceramic with potential for breeding without a neutron multiplier. The ferritic steels are compatible with both helium and water coolant and are selected for both first-wall and blanket structure. A low pressure helium purge stream over the Li_2O is used for tritium processing since direct contact of high pressure helium coolant and Li_2O is not acceptable.

Table 2-4. Candidate First-Wall/Blanket Materials

Coolants:	Helium, Water* (steam), and Lithium
Breeding Materials:	Lithium (liquid), Li-Pb (liquid), Li_7Pb_2, LiAl, Li_2O, Li_2SiO_3, and $LiAlO_2$
Structural** Materials:	Austenitic stainless steel (316), High nickel alloy (INCO-625), Titanium (Ti-6242), Vanadium (V-15Cr-5Ti), Niobium (FS-85), and Ferritic steel (HT-9)
Neutron Multipliers:	Beryllium, BeO, Lead, PbO, and Zirconium

* Water coolant considered is D_2O.

** Representative alloys used for property data base.

Table 2-5. Selected First-Wall/Blanket Materials Options

	Coolant			Structure*		
Coolant	FW	Blanket	Breeder	FW	Blanket	Neutron Multiplier
Reference	D_2O	He	Li_2O	FS	FS	PbO**
Alternate	D_2O	D_2O	Li_2O	FS	FS	PbO**
Backup	Li	Li	Li	V	V	NR***

* Austenitic stainless steel is an alternate selection for the first-wall structure and both austenitic stainless steel and titanium alloys are possible alternatives for the blanket structure.

** If required.

*** Not required.

Since the thermal-hydraulic characteristics of pressurized water are superior to those of helium in temperature-limited systems, an alternate first-wall/blanket materials option is proposed. The alternate concept utilizes D_2O coolant in both the first wall and the blanket. Lithium oxide is retained as the breeding material and ferritic steel as the first-wall/blanket structure.

Liquid lithium, which can be used as both coolant and breeder, provides a unique blanket option. However, the inherent safety of this system has been questioned and maintenance-related problems have been identified. An intermediate coolant loop may also be desirable. However, because the thermal-hydraulics, neutronics, radiation behavior, and design simplicity of this system are generally regarded as superior to other blanket materials options, this system is suggested as a backup. Selected vanadium alloys, which are proposed for the structural material, are believed to be the most resistant to radiation damage of the candidate structural materials, produce low long-term activation products, are compatible with lithium, and possess adequate elevated temperature mechanical properties. Long blanket lifetime may be attainable since the liquid lithium is not sensitive to radiation damage and tritium-release from the liquid also does not present a problem. The key problem of this option is to alleviate the safety concerns by appropriate design.

2.3.2 Neutronics

Tritium breeding and induced activation are important neutronics considerations for STARFIRE. The feasibility of adequate tritium breeding in an actual engineering design must be carefully assessed, especially for solid breeders. Important aspects of tritium breeding and the characteristics of induced radioactivity in various structural and breeding materials are summarized below.

Tritium Breeding

A wide variety of blanket options have been considered for the STARFIRE reactor. The primary neutronics considerations are to achieve an adequate tritium breeding ratio and to maximize the energy production. The former is a requirement that must be satisfied. Enhancing the energy multiplication in the blanket is economically beneficial.

Previous studies have clearly shown that blankets employing liquid lithium as the breeding medium have an excellent tritium production capability sufficient to achieve an adequate tritium breeding ratio with a comfortable margin to offset uncertainties in design and nuclear data. The tritium breeding potential in lithium compounds is lower because the additional elements will: a) increase the effective slowing down power; thus causing a reduction in the $^{7}Li(n,n'\alpha)t$ reaction rate, and b) absorb some of the neutrons that otherwise would be available for inducing the tritium-producing reactions in ^{6}Li and ^{7}Li. It should be noted, however, that maximizing the tritium breeding ratio is not a goal for reactors in a mature fusion economy. For a doubling time of $\sim$ 7 years with a low tritium inventory of $\sim$ 3 kg as in the present STARFIRE design, the tritium breeding ratio required is $\sim$ 1.01. A higher breeding ratio will result in more tritium than can be used, which is not desirable.

The tritium breeding ratio is strongly influenced by the amount of the structural material in the blanket. Furthermore, it is sensitive to the heterogenity of the system, the presence of penetrations, the coolant choice and the spatial distribution of the plasma neutron source. Therefore, the exact tritium breeding ratio can be determined only from three-dimensional calculations that incorporate all the geometrical details of the system. This makes the assessment of the tritium breeding ratio for different breeder materials difficult during the scoping stage of the reactor study when reliance has to be made on one-dimensional neutronics calculations.

Table 2-6 shows the blanket design options examined in the neutronics survey for STARFIRE. Liquid lithium and Li_7Pb_2 have excellent tritium production capability and achieving the required breeding ratio can be assured for a wide range of design conditions and the variety of structural materials considered in this study. For the lithium compounds in which the number of non-lithium atoms is much larger than the number of lithium atoms, the required tritium breeding ratio cannot be realized without the use of a neutron multiplier. Beryllium is the best neutron multiplier as it substantially enhances both the tritium breeding and energy multiplication. Unfortunately, beryllium is resource-limited. Lead is a good neutron multiplier. Adequate tritium breeding ratios appear to be obtainable with Li_2SiO_3 and $LiAlO_2$ provided that large amounts of lead (in the oxide form for reasons discussed earlier are used.

Results indicate that an adequate tritium breeding ratio can be obtained with Li_2O without the use of neutron multiplier. Three-dimensional neutron transport calculations are presently underway to accurately determine the breeding ratio for the reference design. From the overall reactor economics standpoint, there is a strong incentive to reduce the blanket/shield thickness on the inner side of the torus. One important means of achieving this is to replace part or all of the tritium breeding medium in the inner blanket with more efficient radiation attenuators. The trade-offs involved here are being investigated.

Table 2-6. Blanket Design Options Used for STARFIRE Neutronic Study

Breeder	Neutron Multiplier	Structural Material	Coolant
Li_2O	none	Ferritic, titanium	He, D_2O
Li_2O	PbO, BeO, Pb, Be, Zr	Ferritic, titanium	He, D_2O
Li_2SiO_3	PbO, Pb, Zr	Ferritic, titanium	D_2O, He
$LiAlO_2$	PbO, Pb, Zr	Ferritic, titanium	D_2O, He
Li_7Pb_2	none	Ferritic, titanium	D_2O, He
Li	none	Vanadium, ferritic	Li, He

Reactor Activation

The requirement of achieving an environmentally acceptable reactor concept must be taken into account early in the design effort. The major safety and environmental impacts of fusion power reactors, as envisioned today, are associated with the inventories of radioactive tritium and neutron induced activation of reactor components. In order to incorporate such safety and radiological issues into the design considerations, a careful consideration has been devoted to a prudent selection of breeding material, coolant and structural material.

The computation for the radioactivity and radioactivity-related parameters such as biological hazard potential (BHP), and decay β/γ spectrum has been performed by using the RACC[8] code in conjunction with the RACCDLIB/RACCXLIB[9] data libraries.

Effect of Structural Materials on Reactor Activation

Figure 2-5 shows a comparison of the candidate structural materials in terms of biological hazard on inhalation (BHP air) as a function of time after reactor shutdown following a two year reactor operation. Over the time period from 5 years to 50 years after shutdown, the two different ferritic steel systems (FS-CE and FS-X) show a factor of 10-50 lower BHP than the 316 stainless steel alloy. Over the same time period, the BHP in the Ti4381 system is further reduced by approximately one to two orders of magnitude from those for the FS systems. Because of the similarity of the isotope contents in the Ti4381 and V15CrTi alloys, the general trend of BHP variation in the both systems is almost identical, keeping about a factor of 10 difference in their absolute magnitudes over the entire time span under consideration.

A comparison of BHP's in each reactor component for the candidate breeder systems has been made. The structural material is assumed to be ferritic stainless steel (FS-X) throughout the reactor systems. With regard to the coolant, a helium gas is used in all cases except for the liquid lithium blanket which is also cooled by the lithium fluid. It is found that the BHP's in the whole system, as well as in each component, do not vary to any appreciable degree from one breeder system to another. The total BHP's for all the systems are bracketed within a maximum difference of a factor of ~ 2 at each time point over the time span of 0-100 yr. However, it should be noted that the results obtained here are very dependent upon the structural material chosen. In the case of FS-X, the effect of spectrum change (resulting from use of a different breeder material and/or PbO multiplier) on the BHP's tends to be less significant simply due to the large BHP of the structural material itself.

2.3.3 Tritium and Safety Considerations for the First Wall and Blanket

A comprehensive study of various structure/breeder/coolant systems has recently been completed wherein details of experiments investigating potential fusion breeders and coolants are discussed,[10] and hence, will not be

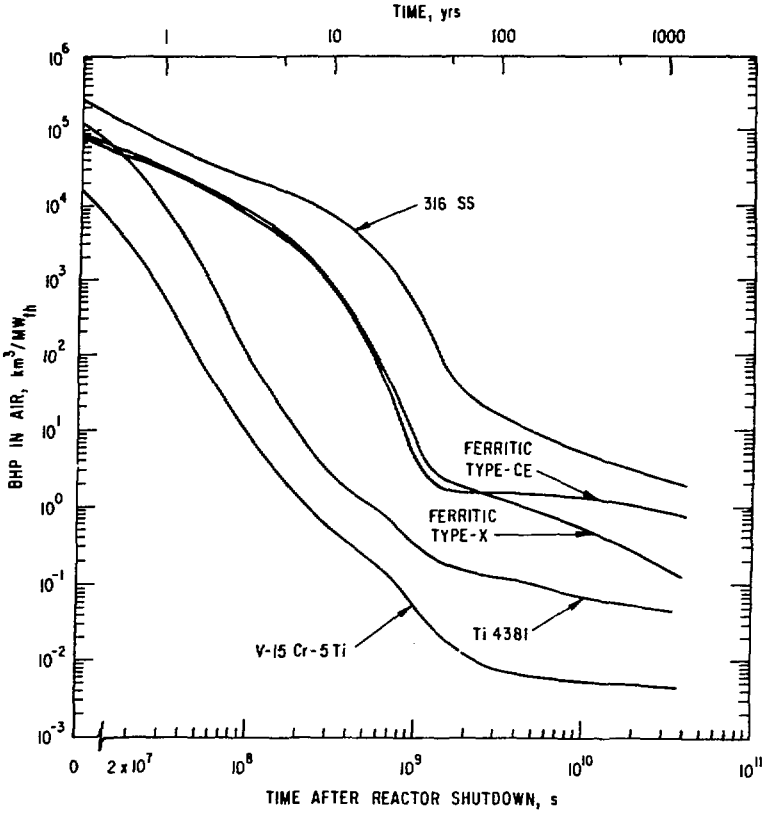

Figure 2-5. Effect of structural materials on biological hazard potential. The results are based on the following system: first wall: 10 mm structural material; blanket: 0.6 m (90% Li + 10% structure); shield: 0.9 m (50% B_4C + 50% structure).

reiterated here. This section addresses the key conclusions of assessments of tritium and safety issues pertaining to three specific areas, namely:

1. The implications of water (or D_2O) as a first wall coolant;
2. Assessment of tritium recovery and temperature limits for candidate breeder materials; and
3. Coolant/breeder/tritium safety considerations.

Implications of the Choice of Water (D_2O) as a First-Wall Coolant

During the course of reactor operation, significant amounts of tritium will pass from the plasma chamber into the first wall coolant (water). The tritium is essentially all converted to HTO, in which form permeation rates

are very small (<< 0.1 Ci/day) and tritium is not lost only to the extent that the coolant water itself is physically lost. Thus, water is a sink for tritium. Permeation rates for tritium passing from the plasma chamber through the ferritic steel tube wall into the first wall coolant have been calculated for various conditions.

For conditions anticipated in systems with a water-cooled first wall and/or blanket, tritium levels are estimated to be 2 to 100 Ci/ℓ. As a point of reference, 20 Ci/ℓ is typical of the level in the moderator of a heavy water reactor (HWR) after many years of operation, however, some control is implemented to maintain this level. This level gives H/T ratios on the order of 10^5 in the water and requires an enrichment of at least six orders of magnitude before one can consider returning the tritium to the fuel cycle.

The use of D_2O as a coolant offers a significant advantage over H_2O because deuterium is a fuel, and therefore, isotopic enrichment requirements are relaxed. For example, the tritium could be recovered in a 99% deuterium mixture, requiring enrichment factors of $\sim 10^3$, which is three orders of magnitude lower than required for light water. Separation factors will be somewhat lower for D_2O, but this is a comparatively small effect. Also, for STARFIRE, 2000 Ci/yr will be generated in the D_2O coolant from neutron activation of the deuterium. This amount is less than that for inleakage from the plasma. Although hydrogen permeation from the coolant through the first wall could affect the plasma performance, deuterium permeation will present no problem. All factors considered, it appears that D_2O is much preferred over H_2O as a coolant.

There are three potential operating scenarios for a water coolant circuit on STARFIRE: (i) allow tritium to build up until the decay rate equals the migration rate, providing the steady-state level is $\sim$ 20 Ci/ℓ; (ii) provide sufficient in plant enrichment capacity to maintain the level at $\sim$ 20 Ci/ℓ (if the migration rate is too high) and dispose of the tritium-rich fraction; and (iii) provide sufficient in-plant enrichment to recover all migrating tritium for recycle to the reactor fueling systems. Clearly, the last of these options is to be preferred.

Assessment of Tritium Recovery and Temperature Limits for Candidate Breeder Materials

In a fusion blanket, the concentration in the solid breeder will build up until the rate of diffusion out of the solid is equal to the tritium generation rate, and steady state is achieved.

The calculated tritium inventories for candidate solid breeders are shown in Fig. 2-6. In view of the very strong temperature dependence and the fact that the inventory is extremely sensitive to the diffusion path length r ($I \propto r^2$), it is not surprising that some analyses conclude that solids will have very low tritium inventories, while others conclude that solids may have very high inventories.

The design solution to this dilemma is proper temperature control. The minimum temperature must be sufficiently high that tritium will diffuse out

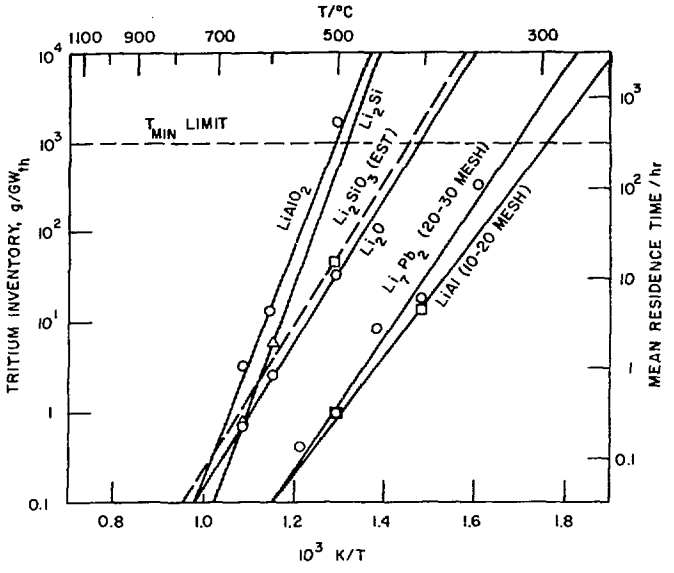

Figure 2-6. Predicted tritium inventory in candidate solid breeding materials (20 mesh) as a function of temperature after low-fluence irradiations.

at an adequate rate, and the maximum temperature must not permit excessive agglomeration and sintering, which could increase the diffusion path length and thereby reduce diffusion rates. It is suggested that, as a design criterion, the inventory of any 5% of the blanket not exceed 500 g per GWth. Therefore, not more than 5% of the blanket can be below the minimum temperatures indicated in Table 2-7 for each candidate breeding material. Therefore, a minimum temperature is established for each solid breeder (Fig. 2-6). The maximum temperature for ceramics may be determined by analogy to oxide fuels for fission reactors, wherein radiation enhanced sintering occurs at $\sim$ 0.6 of the absolute melting point. For alloys, the radiation sintering temperature is estimated to be 2/3 the-absolute melting point.

Coolant/Breeder/Tritium Safety Considerations

In the absence of a detailed design, safety considerations cannot be quantitatively assessed. Therefore, generic safety considerations associated with blanket design are discussed.

Chemical reactivity of breeder or coolant is a significant concern. Helium coolant is not inherently reactive with air or breeder and structural materials, and it is the best choice from reactivity considerations. Water coolant has vigorous exothermic reactions with lithium and lithium alloys

Table 2-7. Temperature Limits (°C) for Solid Breeders

Breeder	m.p. °C	Thermal Effects		Radiation Effects	
		T_{min} [1]	T_{max} [2]	T_{min} [3]	T_{max} [4]
Li_2O	1700[5]	410	1000	460	910
$LiAlO_2$	1610	500	1000	550	850
Li_2SiO_3	1200[6]	420	900	470	610
Li_2Si	760	480	550	530	420
LiAl	700	300	500	350	380
Li_7Pb_2	726	320	530	370	390

[1] Diffusion limited.

[2] Thermal sintering.

[3] Radiation-induced trapping (factor of 10 degradation in tritium release estimated).

[4] Radiation enhanced sintering (0.6 T_m for oxides and 0.67 T for other compounds).

[5] Li_2O reportedly sublimes at temperatures below the melting point.

[6] Li_2SiO_3 is a line compound with a solidus temperature of $\sim$ 1030°C for slightly hypo- or hyperstoichiometric compositions.

to the extent that these breeder/coolant combinations are not considered viable. Water coolant should have only modest reactions with Li_2O (or other oxides) at elevated temperatures. Cleanup of reaction products and corrosion of the structural materials by LiOH pose the major problems with this system. The reactivity of lithium with water, air, and concrete and the associated accident scenarios and cleanup problems are matters of significant concern.

Coolant pressure is a significant safety concern. Pressurized water and helium would both have pressures considerably higher than liquid lithium.

Tritium safety implications are concerned with tritium inventories and the chemical form of tritium. Because tritium is not a radiation hazard, but is an assimilation hazard, the more absorbing oxidized form (T_2O or HTO) has a significantly higher biological hazard than does T_2. Coolant inventories will be lower ($\sim$ 1 g) for He or water, but the tritium will be in

the oxidized form. In the liquid lithium case, the tritium inventory in the coolant will be the blanket inventory, i.e., ∿ 100 g.

2.3.4 Mechanical Design of First Wall/Blanket

First-wall/blanket mechanical design concepts are being developed for the selected reference and alternate materials options. This section discusses rationale for the selection of the design concepts for the reference helium-cooled and alternate water-cooled blanket choices, presents the concepts and discusses their relative merits. The design concept for the backup lithium-cooled blanket is also described briefly.

The reference and alternate design concepts are presently being developed and analyzed further to assure that design requirements are satisfied in the areas of thermal hydraulics, power cycle efficiency, tritium breeding, tritium recovery, fabricability, and structural integrity, and to determine how well they satisfy the design objectives. The concepts will subsequently be compared and the final choice made for the reference first wall/blanket materials combination and mechanical design concept.

The overall approach to mechanical design of the first wall/blanket system is similar for both the reference and alternate materials options. The most important objectives for the designs were to:

- minimize probability/consequences of accidental contact of incompatible materials;
- maximize reliability of system and components, to increase availability;
- maximize maintainability by minimizing need for, and time required for, standard maintenance operations;
- minimize inboard wall and blanket thickness, to reduce reactor size and maximum magnetic field; and
- minimize outboard wall and blanket thickness, to minimize TF and EF coil size.

Selection of the mechanical design concept for the reference helium cooled blanket and the alternate water cooled blanket is strongly dependent on the individual and combined characteristics of the selected structural material, coolant and breeder. Of critical importance is assuring satisfactory adherence to minimum and maximum temperature constraints placed on the solid breeders. For the helium cooled design, minimizing the blanket thickness, manifold and header size were also of major importance, in order to minimize required reactor size.

Both the reference and alternate designs use the concept of individual blanket modules of similar shape and size which are built up into first wall wedge-shaped blanket circumferential sectors. This approach has several advantages. It permits more accurate tailoring of the blanket to match neutron wall load values at specific positions around the plasma cross section.

Accommodation of local discontinuities such as vacuum ports and rf ducts is simplified. Replacement of individual modules can be performed in the hot cell, while the reactor is returned to normal operation following installation of a replacement sector. The reactor is thus shut down only for the time needed to remove the sector containing a faulty first wall or blanket component and to install the replacement sector.

A water-cooled first wall, mechanically and structurally separate from the blanket, was selected for both the reference and alternate concepts. First wall design life is expected to be significantly less than that of the blanket. The separate first-wall concept permits simple replacement (in the hot cell) of a failed first-wall panel without also requiring replacement of the more expensive and longer lived blanket module behind it. The use of water coolant for the first wall in the reference design permits accommodation of the selected neutron wall load (P_{nw}) value of 3.5 MW/m^2 with negligible pumping losses. The two additional disconnect/reconnect operations for the first wall water coolant headers, necessary for removal of a reference blanket sector, are not considered a major addition to the time required for that operation.

The reference first wall/blanket design features a helium cooled blanket. Lithium oxide (Li_2O) is used to breed tritium, which is removed continuously from the breeder through a helium purge gas system. The breeder is sealed to prevent contact with the helium coolant stream. Ferritic steel alloy is the baseline structural material for the blanket and the first wall. The first wall is water cooled and separate from the blanket.

Two mechanical design concepts are being considered for the reference blanket. In the first concept, the module walls are pressurized to the coolant static pressure. The solid breeder is held in sealed tubes, arranged in a staggered rod bank pattern, which are cooled by cross-flowing the helium over them. In the second concept, the helium coolant flows inside tubes each of which is surrounded by solid breeder throughout the module. The two concepts will be compared in the near future after further evaluation to determine which is superior from an overall reactor design standpoint.

The first wall concept for the reference design is essentially a water cooled flat panel. The basic concept is common to both the reference and alternate blanket concepts. Details of the design will be developed later in the study. For the present, the mechanical design concept used is that adopted previously in the ANL-EPR study.[11] In this design, cooling is accomplished by circulating pressurized water in a network of channels that line the plasma side of the panel. The channels are formed by bonding a preformed steel sheet to a second, flat steel sheet. Each panel section spans several blanket modules, and has one inlet and one outlet coolant line which connect to manifolds at the rear of the blanket module. These manifolds connect all first wall panels and the water cooled inboard blanket within a single blanket sector. The manifolds terminate in headers in the vicinity of the helium blanket coolant headers, and are in turn attached mechanically to inlet and outlet feed pipes which remain in the reactor when the sector is removed.

2.4 Maintenance of STARFIRE

Maintenance Approach

The ability to maintain the STARFIRE reactor rapidly with a minimum of radiation exposure to maintenance personnel the key to its acceptance by the utilities and public.

The remote maintenance approach was chosen for in-reactor operations because of the likelihood that current regulatory radiation limits will be significantly reduced and because the reactor hall will be exposed to tritium by permeation and releases during maintenance of the coolant, fueling, vacuum and tritium systems. Some activation may also result from neutron streaming. Use of remote equipment will permit maintenance with a minimal cool-down or clean-up period.

The design philosophy being followed is to minimize the radiation levels within the reactor building; to design all components for complete remote maintenance, and to identify contact maintenance operations where personnel can safely be used with significant economic savings.

All components within the reactor building are replaceable. Some are replaced on a scheduled maintenance basis while others are designed for the life of the plant and are replaced only in the event of failure. Items designed for the life of the plant include the overhead crane, TF coils, EF coils, coolant piping, reactor support structure and radiation shielding. The blanket assembly, impurity control components, rf launchers, pumps, valves, fueling mechanism, power supplies, etc. are replaced on a scheduled basis. Spares are provided for all components with expected high failure rates, so that as one part is removed a pretested replacement is available so reactor operation can commence while repairs to the damaged components are being made. The spares for the superconducting EF coils trapped below the TF coils are stored in place so reactor disassembly is unnecessary in event of a failure. These coils are designed for life of plant but the consequence of their failure suggests in place spares are prudent.

The number of different maintenance operations planned in the reactor building are minimized by using a component "remove and replace" approach. This permits each maintenance action to be preplanned and designed for use with simple push, pull, etc., operations. This approach increases the confidence in the speed of maintenance operations and simplifies maintenance equipment design requirements. Once the damaged or end-of-life components are removed from the reactor, they are transported to a hot cell where more time is available for checkout, repair or disposal. The hot cell will have extensive maintenance capability for testing, component replacement, cutting, welding, machining, pinpoint leak location, and low-Z coating repair.

Redundancy is planned for reactor auxiliary subsystems to permit continued operation of the plant until a scheduled maintenance period or until

the component can be replaced in-service. The particular components where redundancy is planned will be defined as the design progresses; however, current plans include redundant power supplies, vacuum pumps, rf launchers, some valves, pumps and fueling mechanisms.

Availability goals have been established as 85% for the reactor and 75% for the complete plant including the reactor. Allocations of permissible time-to-repair and time-between-failures have been made for major subsystems to serve as a basis for design of the components and maintenance equipment. The maintenance scenario incorporates the current utility practice of shutting down annually for one month of maintenance and a 4 to 5 month shutdown every 5 to 10 years for turbine repair. The resultant permissible downtime goal per calendar year has been allocated as 30 days for scheduled maintenance of the entire plant, 21 days for unscheduled maintenance of the balance-of-plant and 40 days for unscheduled maintenance of the reactor, auxiliary subsystems and maintenance equipment. Convenient preventative maintenance and repair of redundant components is included as part of the maintenance scenario during these unscheduled outages.

Maintenance Features

The design is being developed to keep the top and sides of the reactor clear for access by maintenance equipment. Components are also being combined where practical to minimize the number of subassemblies and improve access. Examples of combined components include; the TF coil room-temperature dewar and shield provides the EF and TF magnet structural support system; and the rf system provides startup and plasma current drive functions.

The blanket is replaceable as a 1/24 sector of the torus. Each 1/24 sector incorporates an integral first wall, limiter, rf duct and air bearing pad that is removed with the blanket. The coolant is manifolded through separate loops for each 1/24th of the reactor to permit leak isolation to individual sectors. The helium coolant lines and the water coolant lines to the rf duct and limiter utilize mechanical disconnects. The life goal for limiter and rf duct is 4 years and the blanket life goal is 8 years. After four years the blanket sector is replaced. The used sector is refurbished in the hot cell by replacing the limiter, rf duct and low-Z coating. Periodic in-situ replacement of the low-Z coating may also be required.

Blanket module leak detection will be accomplished by sequentially reducing the pressure in individual blanket sectors and monitoring the change of the partial pressure of helium in the plasma chamber with a gas analyzer. This technique requires valves that isolate sectors from the primary coolant loop. Leak detection of the limiter first wall and rf launcher water system will also rely on reducing the system pressure of each sector sequentially and denoting changes in the detected leak rate. Leak detection of the shield system to the plasma chamber system will be accomplished by injecting helium into a cavity between redundant seals. The blanket leak detection system is dependent on the particular design that is developed and will be modified as necessary.

The shield is designed to last the life-of-plant and will be replaced only in event of unscheduled failures. A shield door is provided that permits access to the blanket. The door is sealed with redundant seals that are shielded locally to reduce the radiation damage. The seals are replaced each time the door is opened. The basic shield consists of sectors welded together to form the vacuum boundary. Cutting and rewelding the poloidal seals is required if shield sector replacement is required.

The TF coils are also life-of-plant components. They utilize a common welded dewar in the center post region. Coil replacement time is not significantly impacted by the welded dewar. Annealing of the TF coil is planned every 10 years to reduce the effects of radiation damage in the stabilizer.

The EF coils are also life-of-plant. EF coils inside the TF coil are copper and are segmented to permit removal. An elevation system is provided to raise and lower the outer coils for access to the blanket. The external EF coils are superconducting. Those on the top and sides of the reactor can be removed for replacement. Spare EF coils are provided for those trapped below the TF coils. In event of failure the coil is cut out and the spare raised into position.

The vacuum system utilizes redundancy to improve the probability of continuous operation between scheduled maintenance periods. Twenty-four cryosorption pumps with isolation valves are provided of which approximately 20 are required for operation. External valves and pumps leading to the tritium processing system utilize redundancy.

The power supplies are assumed fully redundant and include a replacement capability during operation. The power supply systems are located outside the primary confinement building and can be repaired during plant operation.

Maintenance Time Allocations

A preliminary listing of the scheduled maintenance actions is shown in Table 2-8. The assumed critical path is shown with the presumption that all other maintenance actions can be accomplished in parallel operations. This listing will be updated as the program progresses.

The unscheduled maintenance item listing is shown in Table 2-9. The values shown for Mean-Time-To-Replace (MTTR) are assumed values based on past studies. The average downtime per year is then assigned to each subsystem based on the perceived relative reliability and complexity of each subsystem. The result is a permissible failure rate per calendar year. These values can then be used by subsystem designers to define the redundancy and design margin requirements for the subsystems. An accurate assessment of the actual failure rates can only be derived after subsystems are defined as to the number of components, redundancy provisions, the types of failure modes and failure rate per failure mode have been established. Our program will utilize historical data where possible to assess feasibility of meeting the requirements of Table 2-9.

Table 2-8. Scheduled Maintenance

Action	Frequency (yr)	Replaced/ Outage (%)	Time-to-Replace (days)	Critical Path
Reactor shutdown and startup	Annual	N/A	2	*
Shield door seal replacement	Annual	25	2	*
RF wave guide window replacement	4	25	6	*
Blanket replacement	Annual	25	20	*
Vacuum pump replacement	Annual	16	6	
Fueling system replacement	Annual	25	6	
TF coil anneal	10	100	120	(1)
Coolant loop component replacement	Annual	25	14	
Power system component replacement	Annual	50	14	
Maintenance equipment repair	Annual	N/A	N/A	

* These operations must be done sequentially, other operations are assumed to be performed during the critical path time frame.

(1) Compatible with 10-yr shutdown for 16 to 20 weeks for turbine repair.

Table 2-9. Unscheduled Maintenance (Forced Outage)

Subsystem	MTTR[a]	Average Downtime per Year (days)	Permissible Failure Rate per Year[b]	Availability (%)
Shield sector	30	2	0.04	5
RF system	30	3	0.1	7.5
Blanket system	30	15	0.5	37.5
Vacuum system	6	2	0.3	5
Fueling system	4	2	0.5	5
Magnet system - TF	350	2	0.006	5
Magnet system - EF	60	1	0.016	2.5
Primary coolant	4	2	0.03	5
Auxiliary coolant - H_2O	4	2	0.5	5
Auxiliary coolant - GHe	4	2	0.5	5
Auxiliary coolant - LN_2	4	2	0.5	5
Power supplies	4	2	0.5	5
Maintenance equipment	2[c]	1	0.5	2.5
Total:		40		100%

[a]Includes startup and shutdown.

[b]Failure resulting in an outage.

[c]Occurs during outage only.

3.0 FUSION SYSTEMS ENGINEERING

3.1 Systems Studies

3.1.1 Technology Development Impact on the Choice of Fusion Fuel Cycles

C. C. Baker, A. Bolon,* R. Clemmer, K. Evans, Jr., J. Jung, L. Turner, Fusion Power Program, and T. Blue,** D. Driemeyer,** J. Metzger,** and C. Miley**

General considerations for the study of the technology considerations of alternate fuel cycles are described below. Basic considerations regarding tokamaks and field-reversed mirrors are also included. Further considerations regarding neutronics, fuel processing systems and safety considerations are also reported. Additional results are also reported regarding the application of neutronic computer codes to cyclotron radiation transport.

3.1.1.1 Fuel Cycles and Confinement Concepts

In order to study "representative" combinations that are illustrative of a wide variety of possible combinations, we have selected for study a matrix of alternate fuels along with a modest and high β confinement systems. Since catalyzed-D is the only "self-sufficient" (only requires naturally available deuterium) low-temperature fuel, it is selected as the base fuel. However, due to its potential attractiveness, D-^{3}He is also considered despite the complication of ^{3}He breeding. Since tokamaks are presently the most highly developed confinement system, and since they (or at least modest β versions) can burn these low temperature fuels, they are selected as a representative modest β (10-20%) confinement system. (These β values are about a factor of two larger than predicted by most current theories, but are considered to be reasonable extrapolations for purpose of the study.) Concurrently, the Field-Reversed Mirror (FRM) is selected as a representative high-β (> 70%) device. This is acceptable for the low-temperature fuels, but may not be adequate for the higher temperature fuels where even more innovative confinement approaches such as Surmac may be necessary.

3.1.1.2 Typical Power Splits

Table 3-1 presents the power splits for the reference semi-catalyzed D, fully catalyzed D, and D-^{3}He tokamaks. Note that the fraction of power in neutrons is less by almost an order of magnitude for D-^{3}He than for semi-catalyzed D. The fraction of power in neutrons is less by about 10% for fully-catalyzed D than for semi-catalyzed D. This is, of course, because the fusion product ^{3}He is burned in the fully-catalyzed D reactor.

For purposes of technology considerations discussed in the next section, the most important parameter is the fraction of total power carried by neutrons. This is relatively constant for the various cases discussed above,

---

* On leave from the University of Missouri - Rolla.

** University of Illinois, Urbana, Illinois.

Table 3-1. Power Splits for Tokamaks and FRMs

Power Splits (%)	Power Splits for Tokamaks		
	Semi-cat-D	Cat-D	D-^{3}He
Leaking Particles	.20	.26	.33
Bremsstrahlung	.26	.25	.46
Cyclotron Radiation	.11	.11	.16
Neutrons	.43	.38	.05

Power Splits (%)	Power Splits for Tokamaks	
	Cat-D	D-^{3}He
Leaking Particles	.25	.24
Charged Fusion Products	.19	.39
Bremsstrahlung	.18	.26
Cyclotron Radiation	.03	.08
Neutrons	.35	.03

thus it is possible to examine certain first wall/blanket/shield problems without specifying a particular type of device. This is the general approach taken in the next section when the fuel cycles are characterized in terms of neutron power fractions by the following representative values:

D-T	$\sim$ 80%
D-D	$\sim$ 40%
cat D-D	$\sim$ 40%
D-^{3}He	$\sim$ 1%

In the previous progress report, the possibility of calculating cyclotron radiation transport with ANISN was discussed.[1] The problems noted there have been solved, and a reliable system of codes is now available. These codes pertain to reactors which can be modeled as long circular cylinders. The input consists of the plasma profiles and the reflectivity matrix of the wall, and the output is the spectral distribution of the cyclotron power loss. An individual run, consuming about a minute of machine time, is required at each frequency. This appears to be the first system of deterministic codes for cyclotron radiation transport. An alternative approach uses Monte Carlo methods.[2]

As a byproduct, it was possible to assess the accuracy of an approximate power-loss formula derived by Trubnikov,[3] in the regime of the plasma parameters appropriate to D-D reactors. The assessment was done with uniform profiles, since these are also assumed by Trubnikov. In the cases studied (typically

$n_e = 5.5 \times 10^{20}$ m^{-3}, $T_e = 45$ keV, B = 10 T, radius = 2 m), it was found that the Trubnikov formula overestimates the power loss by a factor of about 3 or 4. Details of this and the profile-dependent calculations appear in Ref. 4 and were reported in a recent meeting.[5]

3.1.1.3 Neutronics Analysis

The nuclear analysis is oriented toward identifying the design impact of alternate fuel cycles in terms of reactor shielding performance and environmental effect.

Figure 3-1 shows the variation of the nuclear dose in an epoxy-base magnet insulator as a function of the bulk shield thickness for the four candidate fuel systems. The dose variation is represented as a plant lifetime in terms of MW-yr/m^2 of the total integral wall load. The dose limit criterion assumed is 5×10^9 rad in the insulator. As an example, for a total wall loading of 1 MW/m^2 and a 30 year lifetime, D-^{3}He case would require about 70 cm of shielding compared to about 1 meter for the cat-D and nonbreeding D-T case. A D-T breeding blanket with shield sould be about 1.5 meters thick.

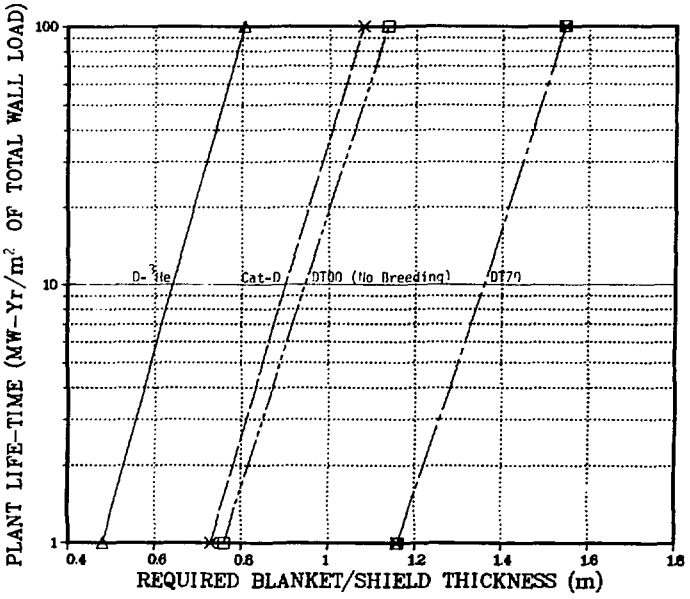

Figure 3-1. Blanket/shield thickness for fusion fuels.

Figure 3-2 represents another aspect of the design impact of the different fuel cycle systems. Shown in the figure is the biological hazard due to inhalation (BHP_{air}) associated with the blanket/shield designs based on use of stainless steel structural material. One finds that beyond 30 yr, after reactor shutdown, the BHP_{air} in the cat-D systems, which have softer neutron spectra than the D-T system, exceed that of D-T. This is due to the fact that many of long-term radioactive isotopes, ^{63}Ni for instance in this case, are induced to an appreciable degree through (n,γ) reactions which are favored by low-energy neutrons. The results presented in Fig. 3-2 indicate how one has to reduce the $d(d,^3He)n[2.45\ MeV]$ from the fuel cycles involving deuterium, in order to fully exploit "clean" advanced fuel reactor designs.

3.1.1.4 Fuel Cycle Considerations

The fuel reprocessing parameters and costs for D-T, cat-DD and D-^{3}He cases for a reference 2500 MWth reactor are shown in Table 3-2. The D-T and cat-DD cases have comparable vacuum pumping requirements, which is a major cost item in the fuel cycle system. The D-^{3}He case has reduced hydrogen pumping requirements but significantly increased He pumping requirements resulting in higher vacuum system costs. The total fuel cycle system costs are very similar for all cases.

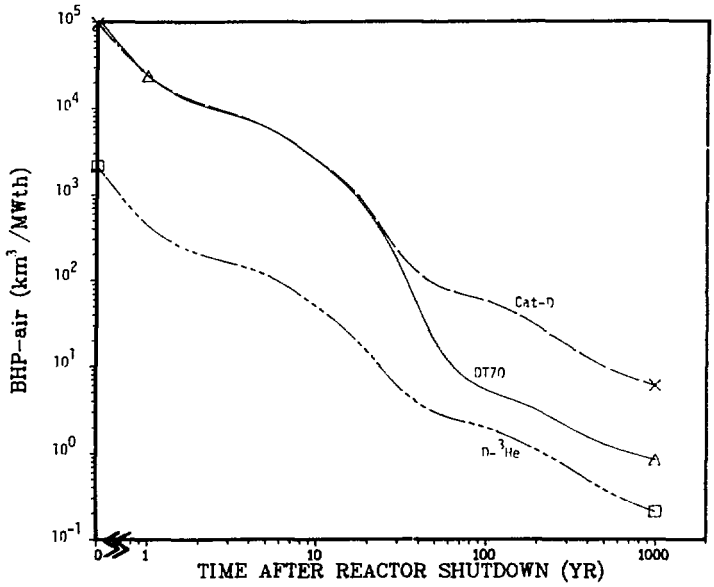

Figure 3-2. Biological hazard potential in air for fusion fuels for stainless steel structure.

Table 3-2. Fuel Processing Requirements for Alternate Fusion Fuel Cycles

Thermal Power - 2500 MWth

	Fractional Burnup		Fuel Burned Per day (g)			Required Pumping Speed (m^3/s)		Cost ($M)				
	D	^3He	D	T	^3He	HDT	He	Tritium Recovery	Vacuum System	Fuel Processing	Emergency Air Detritiation	Total
Reference D-T	.05	-	230	345	-	1.8×10^4	9.5×10^2	2.0	13.3	14.8	7.1	37.2
Cat-DD (burn 1/2 of ^3He)	.05	.50	654	*	89.2	2.6×10^4	9.8×10^2	0.0	31.4	4.8	4.9	40.9
D-^3He (lean D)	.10	.05	221	-	331	4.6×10^3	1.8×10^4	0.0	27.9	4.0	3.9	35.8

* Recycled.

As noted previously, deuterium is abundant while ^3He is not. Potentially available U.S. resources of ^3He are estimated to be 200-500 kg.[6] A 2500 MWth D-^3He reactor would burn 330 g/day or 120 kg/yr. Since natural resources of ^3He are not sufficient, the fuel must be supplied either from a D-D reactor or from decay of tritium.

A 2500 MWth reactor burning no ^3He will produce 244 g of ^3He per day. This is not sufficient to supply one comparable D-^3He reactor. Further, since some ^3He will be burned in the cat-DD reactor, the support ratio will be less than ~ 0.5.

Another potential source is tritium decay. To produce 120 kg/yr of ^3He, a tritium inventory of 2150 kg is required. A storage facility for this amount of tritium is estimated to cost 200 million dollars. Such large inventories of tritium are clearly a major concern. The source of tritium production could be from D-T reactors. Assuming the excess tritium breeding ratio is 0.1, it would require about 170 D-T reactors to produce enough ^3He by tritium decay for one D-^3He reactor of the same power level. This obviously is too low a ratio of D-^3He to D-T reactors to be of any interest. It is clear that utilization of D-^3He requires the use of D-D reactors as a source of ^3He, and even then one will probably require at least two D-D reactors for every D-^3He reactor of the same power level.

3.1.1.5 Safety Considerations

The presence of tritium is one of the safety hazards under consideration. The total tritium inventory varies depending on the fuel combination involved.

A typical 2500 MWth D-T system would require 8000 g of tritium inventory, cat-DD 100 g, and D-^{3}He only 10 g. Of those totals the amount of tritium considered to be vulnerable is 2000 g for D-T, about 20 g for cat-DD and about 2 g for D-^{3}He. The vulnerable positions are that part of the tritium which could conceivably be released in the case of an accident. Even with inventories as low as a few grams, some type of emergency tritium cleanup system will be required.

The induced radioactivities in the first wall and the structural materials in the blanket and shield are the other major sources of radioactivity presently being considered. Several candidate materials have been considered for all three fuel systems. The candidate materials considered are 316 stainless steel, Ti-4381 and V-15Cr-5Ti alloys. The normalized activities (Ci/MWth) of these alloys have been calculated for preliminary alternate fuels design conditions both during reactor operation (from 1 second to 2 years) and following reactor shutdown (from time zero to 1000 years).

The amospheric (χ/Q) dispersion of tritium and of structural material was examined for a hypothetical accident based on a short-term uniform release from a point source. A simple model is utilized in order to compare the relative external dose from the candidate alloys dispersed in a Gaussian plume. The impact of tritium leaking from the reactor building following a hypothetical accident was also calculated using the same methodology.

The relative external doses due to a given structural material in different advanced fuel systems being volatized by a hypothetical reactor accident and its leaking out of containment is shown for 316 stainless steel in Fig. 3-3. The same information could have been plotted for the other candidate materials, but they are generally similar, except the values are approximately an order of magnitude lower for the vanadium alloy.

Based on the results, the cat-DD system produces higher total external doses following a hypothetical accident than does a D-T system; while the D-^{3}He system produces much lower doses. The relative doses for D-T compared to D-^{3}He are about 10 times as great for 316 SS, 35 times for the vanadium alloy and about 60 times for the titanium alloy. The impact of the absolute value of these doses relates to the size of exclusion boundary that would be required around a fusion power plant.

The relative effect of the vulnerable tritium inventory in the reactor building was also calculated for each of the advanced fuels systems. The normalized activities of tritium would be 7.7×10^3 Ci/MWth for D-T, 77 Ci/MWth for cat-DD, and 7.7 Ci/MWth for D-^{3}He. The activity of tritium when compared to the activity of structural material is generally quite small. The external whole body tritium doses from the plume at 200 meters from the reactor and at one hour following an accident would be 1.9×10^{-9} rem/s-MWth for D-T, 1.9×10^{-11} for cat-DD, and 1.9×10^{-12} for D-^{3}He. The whole body doses due to tritium compared to the doses due to structural materials are small (on the order of 0.10 percent).

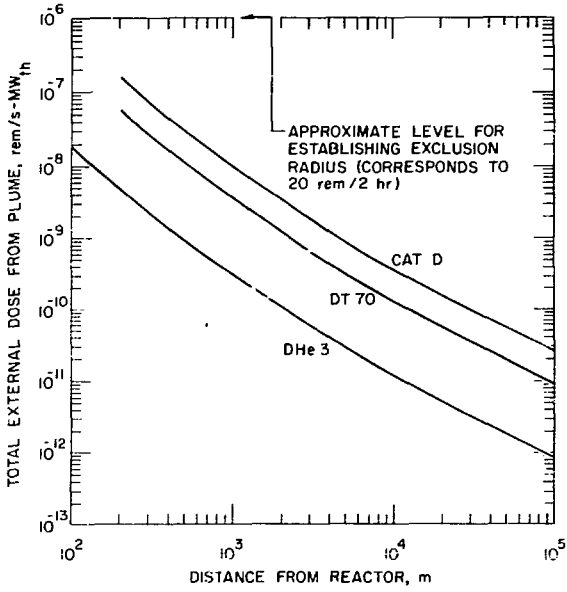

Figure 3-3. Relative external doses for alternate fuel system.

3.2 Tritium Processing and Control

3.2.1 Development of Processing Technology for D-T Fusion Reactor Breeder Blankets

The program underway in the Chemical Engineering Division to develop processing technology for D-T fusion reactor breeder blankets is continuing. Progress during spring to fall calendar 1979 is summarized below:

3.2.1.1 Liquid Lithium Processing Studies

J. R. Weston, W. F. Calaway and V. A. Maroni, Chemical Engineering Division

The Lithium Processing Test Loop (LPTL) was shut down for scheduled maintenance in late August, 1979 after ∿ 9500 hours of operation. During the shutdown several heaters on the reservoir tank were replaced. Also, the valve leading to the getter trap (which had previously developed a bellows leak) was cut out and a pipe section was welded in its place. On October 4, 1979, the LPTL was restarted. Following the initiation of flow, there was evidence of some increased resistance to liquid movement in the piping system, but a stable temperature profile was achieved. On the following day (October 5, 1979) at 12:40 p.m., a pipe rupture developed in the center of the EM-pump channel, which caused a spray-type release of lithium. The

lithium ignited immediately, but was extinguished with the prescribed fire suppressants. Relatively little damage was done to the LPTL system and enclosure, but a fine particulate dust (lithium compounds and fire extinguishant) settled on many surfaces in the cell and in most of the adjacent laboratories. Cleanup of the LPTL facility and adjacent areas was reasonably well completed in about a week. An investigation of the incident is underway to determine the cause, the adequacy of safety systems response, and important lessons to be learned. The results of this investigation will appear in subsequent progress reports.

Prior to the LPTL shutdown in late August, two successful on-line metering experiments were completed. In one of these experiments, a thin-walled Nb-1%Zr tube, plugged at one end and connected to a high vacuum mass spectrometer system on the other end, was immersed in the LPTL reservoir tank below the liquid surface and operated as a permeation-type hydrogen meter. Although the background hydrogen signal in the vacuum system was too large to permit measurement of permeating H_2, it was possible to monitor the permeation of deuterium following controlled LiD additions to the lithium in the reservoir tank. In these tests (see Fig. 3-4), the ^{+}HD and $^{+}D_2$ signals from the mass spectrometer were recorded as a function of time following the closure of a standard D_2 leak and the main valve to the membrane assembly. The permeability of Nb-1%Zr calculated from these data (at 375°C) was in very good agreement with existing data for pure niobium at the same temperature.

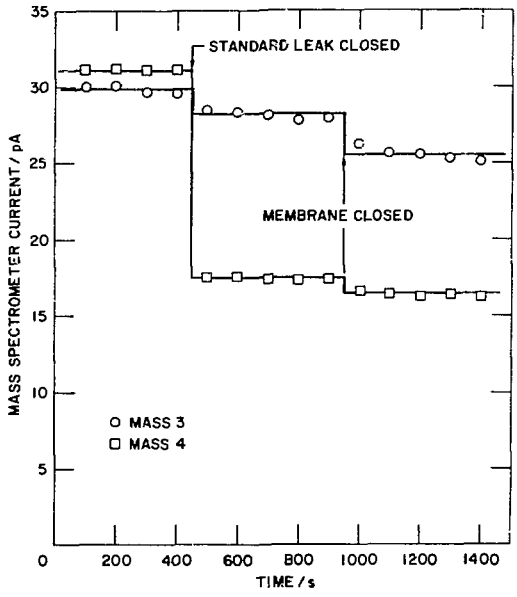

Figure 3-4. Lithium Processing Test Loop (LPTL) Nb-1%Zr hydrogen meter test.

In the other monitoring experiment, a specially-designed four-point electrical resistance probe (see Fig. 3-5) was inserted in the reservoir tank and changes in the concentration of total impurity (mainly hydrogen isotopes in the tests conducted) were monitored during cold trap performance tests. The expected response of the meter to LiD additions was achieved, and the removal of hydrogen isotopes by the cold trap was verified on-line, by maintaining the LPTL lithium in the hydrogen-saturated mode. Cold trap efficiencies of $\sim$ 50% per pass for LiH (LiD) removal were recorded in one run, but as is shown in Fig. 3-6, an appreciable sensitivity of efficiency to flow rate was observed. This apparent sensitivity will be investigated further in subsequent tests.

In yet another impurity monitor-related study, a sample of a ThO_2-Y_2O_3 oxygen meter tube that had been subjected to $\sim$ 1500 hours of service in liquid lithium by M. Down, et al., at the Westinghouse Research and Development Center, Pittsburgh, PA, was examined using the ion microprobe mass analyzer (IMMA). This was from the same type of tube and meter arrangement that was developed by Westinghouse for use in liquid sodium systems. (The performance of the particular meter from which the subject tube came has been described by Down and Whitlow [Proc. First Topical Meeting on Fusion Reactor Materials, 1979 -- to be published in J. Nucl. Mater.)]. The results of the IMMA study are shown in Fig. 3-7. Approximately 0.6 mm of the $\sim$ 1.6 mm thick tube has been penetrated by the lithium. The shape of the distribution profile indicates that the lithium is moving not by bulk diffusion but rather through

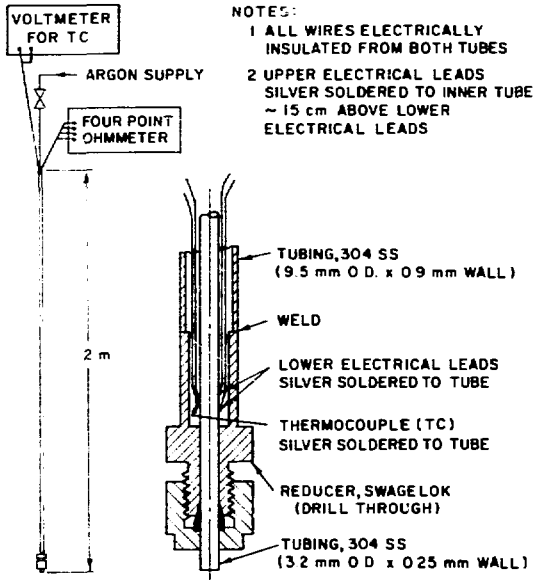

Figure 3-5. Schematic diagram of the electrical resistance-type impurity probe installed in the LPTL.

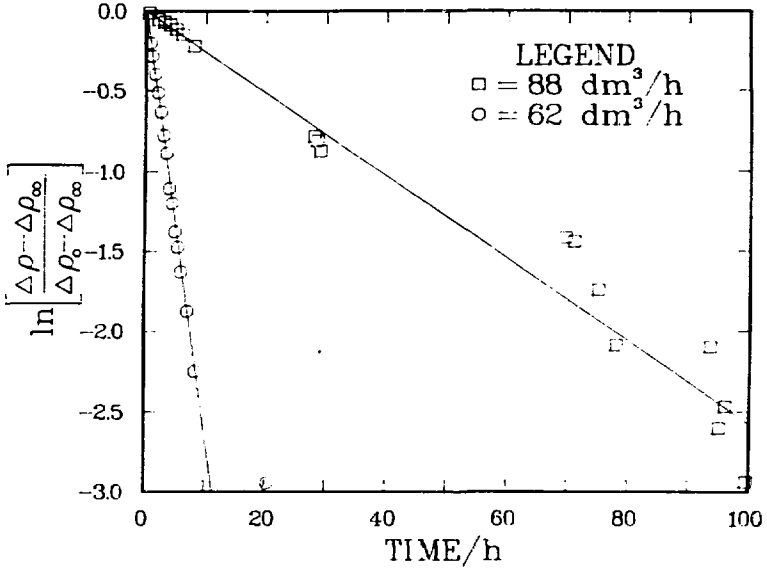

Figure 3-6. The rate of impurity removal in the LPTL by cold trapping as measured resistometrically, where ρ_o is the electrical resistivity of the lithium solution, ρ_o is the resistivity before cold trapping, and ρ_∞ is the resitivity after cold trapping.

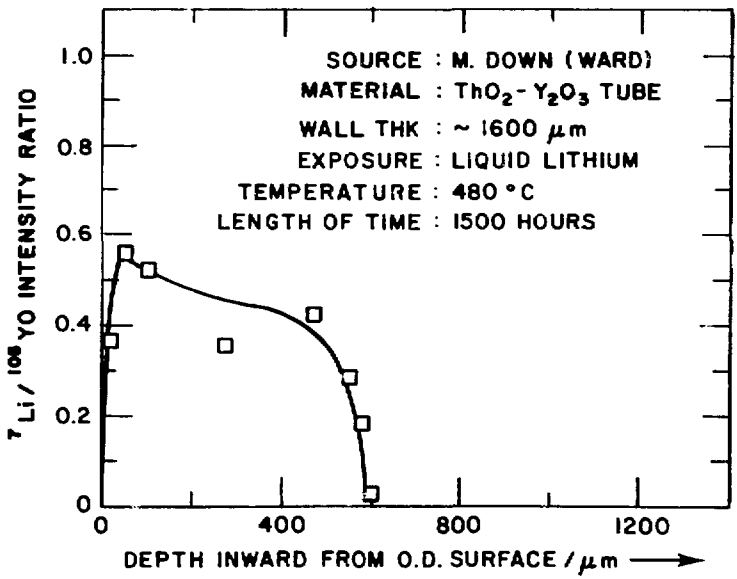

Figure 3-7. Ion microprobe mass analyzer scan of ThO_2-Y_2O_3 oxygen meter tube exposed to lithium at 480°C for ∿ 1500 hours.

interconnected pores at a rate of ∿ 3.5 mm/year. At this rate, the lifetime of a given tube, before electrolyte shorting occurred, would be something less than 6 months. The results of this examination of the lithium-exposed ThO_2-Y_2O_3 tube point out one of the major difficulties in using ceramic-type materials in a lithium environment. Any ceramic materials developed for use in electrolytic lithium metering systems would, in addition to being inert to lithium, have to have a very high density (near 100%) with no interconnected porosity.

3.2.1.2 Alternative Breeder Material Studies

R. G. Clemmer, P. A. Finn, N. R. Chellew and V. A. Maroni, Chemical Engineering Division

An experimental program has been initiated to evaluate various aspects of the tritium recovery and impurity control questions facing tritium breeding materials that represent alternatives to liquid lithium. Prime candidates in this regard are lithium-lead alloys (solid and liquid) and lithium-containing ceramics. A number of experiments are either underway or in the planning stages. The scope and objectives of these experiments are summarized below:

- A Li_7Pb_2 loaded Zircaloy capsule has been fabricated and loaded into the Oak Ridge Reactor (ORR) in the poolside position. The purposes of this experiment are to examine the tritium distribution profile following irradiation to a dose sufficient to generate ∿ 30 Curies of tritium and to set up a postirradiation examination program that can be used in subsequent in-pile tritium-breeder tests.

- An in-pile solid breeder experiment with capability for in-situ tritium recovery and breeder temperature control, is currently being planned. The purposes of this experiment are to determine tritium-holdup characteristics of solid breeder materials under steady-state recovery conditions, to examine breeder material morphology changes in a radiation environment, and to investigate breeder/structure compatibility under irradiation.

- The applicability of the all-lithium-halide molten salt extraction method for recovering tritium and impurities from liquid lithium is being tested on lead-rich lithium-lead alloys in the liquid state. If cross contamination of the lead alloy (with halogen) and the salt (with lead) presents no problems, the method should be even better suited to the lead-lithium alloys than it has already proven to be with liquid lithium.

The in-pile experiments described above are being carried out cooperatively with R. L. Senn of Oak Ridge National Laboratory, E. R. Ebersole of EBR-II, Idaho, and A. G. Hins of the ANL Materials Science Division.

3.3 Engineering Test Facility Studies

P. A. Finn, R. G. Clemmer and V. A. Maroni, Chemical Engineering Division

The DOE design activities for a near-term tokamak power reactor have been consolidated in a single design center under the direction of D. Steiner

at the Oak Ridge National Laboratory. The reactor, the Engineering Test Facility (ETF) will be the next fusion device after TFTR currently being built at PPPL. The ANL contribution to this effort involves primary responsibility for the design of ETF fuel processing and tritium containment systems. During FY 1979, the work centered primarily on scoping studies and R&D assessments which are now complete. In FY 1980, a detailed design of the ETF tritium systems is being carried out, with updating as necessitated by changes in the basic ETF reactor design. Specific tasks completed during the second of FY 1979 are summarized below.

A three-dimensional neutronic calculation of experimental breeder-test-module size effects was conducted in collaboration with Y. Gohar of ANL/AP. The model used in the calculation was based on inserting various-size test-modules into ETF at the out-board horizontal mid-plane position. The remainder of the blanket was assumed to be non-breeding. The principal conclusions of this study are summarized in Table 3-3.

Table 3-3. Conclusions from the Study of Experimental Breeder/Energy Conversion Module Size Effects

• Modules with front face dimensions in the range 0.5 m x 0.5 m to 1.0 m x 1.0 m and with thickness of 0.5 to 1.0 would be relatively free of boundary effects from a neutronic viewpoint.
• Single module studies would yield meaningful breeder/energy conversion system test data.
• Tests of blanket system integration and the production of meaningful quantities of sensible heat would require several test modules.
• If module size becomes an issue, considerable useful information could probably be gained from small, reflector-shrouded test modules.
• The maingfulness of breeder/energy conversion experiments on ETF is probably more sensitive to duty factor and repetitive pulsing characteristics than to module size considerations.

A computer subroutine was developed to simulate the processing step of the lithium-droplet-type divertor concept being considered for use on ETF. Lithium flow rates, mean processing residence times, and tritium removal efficiencies are adjustable in the program. The processing model is based

on the molten-salt-extraction method using data developed at ANL. Typical results of calculations employing the new ETF divertor-subroutine are presented in Table 3-4. The flow of lithium to the processing unit was adjusted to be 100%, 50%, and 10% of the full divertor flow for cases (1), (2), and (3), respectively. The tritium level in the lithium-divertor circuit constitutes 1 to 6% of the total ETF tritium inventory of which the largest fraction is in the fuel storage system.

Table 3-4. Parametric Analysis of Lithium Processing Requirements for the ETF Lithium Divertor Design

Divertor Cleanup System Parametered	Flow Parameter[a]		
	Full Flow	Half Flow	One-Tenth Flow
Primary lithium flow (kg/day)	9.42E 06	9.42E 06	9.42E 06
Secondary lithium flow (kg/day)[b]	9.42E 06	4.71E 06	9.42E 05
Molten salt flow (kg/day)	3.01E 07	1.51E 07	3.01E 06
Mass - primary lithium (kg)	9.42E 04	9.42E 04	9.42E 04
Mass - secondary lithium (kg)	9.42E 04	4.71E 04	9.42E 03
Mass - molten salt (kg)	3.01E 05	1.51E 05	3.01E 04
*Residence time Li-primary (day)	1.00E-02	1.00E-02	1.00E-02
*Residence time Li-secondary (day)	1.00E-02	1.00E-02	1.00E-02
*Residence time salt (day)	1.00E-02	1.00E-02	1.00E-02
Tritium in Li (kg/kg)	4.13E-07	7.26E-07	3.23E-06
Tritium in salt (kg/kg)	3.10E-08	5.44E-08	2.42E-07
Tritium pressure (Pa)	8.02E-09	2.48E-08	4.91E-07
Number of passes/day	1.11E 02	1.27E 02	1.42E 02
Number of contactors	6.82E 01	3.41E 01	6.82E 00
Size of electrolytic zone (M3)	4.72E 01	5.37E 01	6.04E 01
Cost - divertor cleanup ($)	2.15E 06	1.88E 06	1.67E 06
Tritium in divertor (g)	38.9	68.4	304.1
Tritium in Li loop (g)	20.7	18.2	16.2
Tritium in salt loop (g)	9.3	8.2	7.3
Total tritium inventory	5143.7	5169.5	5402.4

[a] Fraction of the total divertor-lithium flow distributed to the molten salt processing system.

[b] The parameter being varied.

A preliminary fuel recycle and purification system layout has been scoped out for ETF as shown in Fig. 3-8. A complete parameter list for the ETF tritium and vacuum systems has been computed (using TCODE) and transmitted to the ETF Design Center. A fractional burnup of ∿ 10% is achieved with a particle confinement time of 1 s and a reflection coefficient of 0.85. The total tritium inventory is ∿ 5.5 kg, most of which (∿ 4.8 kg) is in storage. The total tritium inventory could be reduced considerably by relaxing the storage requirements.

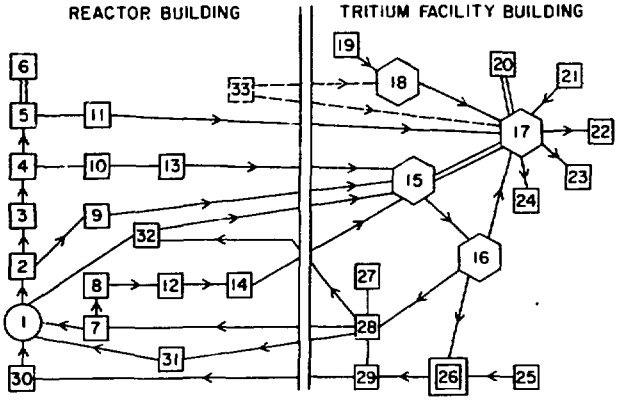

1 PLASMA CHAMBER
2 DIVERTOR
3 DEBRIS SEPARATOR
4, 8 DT CRYOCONDENSATION PUMPS
5 HELIUM PUMP
6 SURGE TANK
7 NEUTRAL BEAM INJECTOR
9 TRITIUM RECOVERY, DIVERTOR
10, 11, 12 REGENERATION PUMPS
13, 14 METAL BELLOWS PUMPS
15 FUEL CLEANUP UNIT
16 ISOTOPIC SEPARATION UNIT
17 TRITIATED WASTE TREATMENT
18 EMERGENCY AIR DETRITIATION SYSTEM
19 TERTIARY ENCLOSURE
20 WATER - TRITIUM RECOVERY UNIT
21 SECONDARY ENCLOSURE
22 DETRITIATED GASES: N_2, O_2, CO_2
23 HELIUM (TRITIUM - FREE)
24 TRITIUM WASTES
25 T_2 - SHIPMENT/RECEIVING
26 T_2 AND DT STORAGE
27 D_2 SUPPLY
28 D_2 STORAGE
29 FUEL BLENDER
30 PELLET FUELER
31 D_2 - GAS FUELER
32 D_2 - COVER GAS VACUUM SYSTEM
33 EVACUATED BUILDING VACUUM SYSTEM

Figure 3-8. Fuel cycle scenario for ETF.

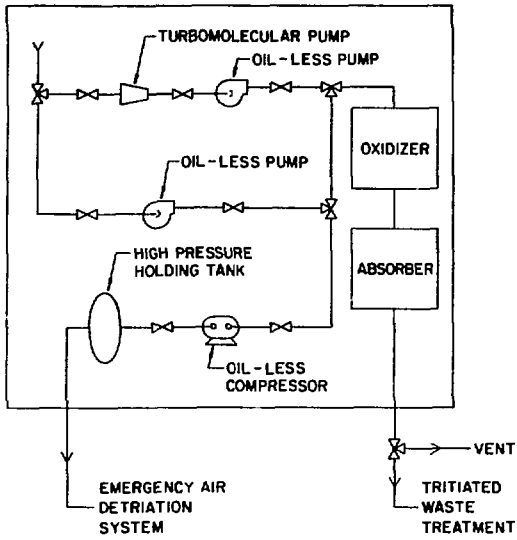

Figure 3-9. Processing system for evacuated building.

Table 3-5. Comparative Assessment of Vacuum Versus Inert Atmosphere Building: Tritium Containment Implications

Considerations	Vacuum Building	Inert/Ambient Building
Building structural failure	*(?)	X,+
Time average residual tritium level	X,+	X
HTO formation (moisture assisted)	X,+	*
HTO soaking/desoaking (surfaces)	X,+	X
Post-accident release cleanup	X	X,+
Post-shutdown access	X,+	X
Scrubber system size/cost impact	- - - - - Toss Up - - - - - - - -	
Ex-building space impact	X	X,+
Overall tritium-related cost impact	(?)	+
Design-connected R&D requirements	*	X,+
Overall impact on design decision	0	0,+

+ Favored approach.

X Some problems that appear resolvable.

* Some critical problems that need resolution.

0 Seems not to be a high-level design choice drive.

An analysis was made of the limits of anticipated tritium leakage rates from the plasma chamber to the reactor building for ETF. The ETF building and vacuum parameters upon which the analysis was based were supplied by the General Atomic Company; a major co-participant in ETF. An optimistic analysis employing simple steady-state leakage and flushing considerations resulted in an allowable leak rate of $\leq 4 \times 10^{-5}$ Pa-m^3/s of DT to avoid exceeding the maximum permissible tritium (as HTO) concentration (MPC) in a controlled area, 5 $\mu Ci/m^3$. A more pessimistic but perhaps more realistic analysis which included adsorption of HTO (formed from leaked DT) on building surfaces and its subsequent release, indicated that for any reasonably achievable leak rate, a normal-operating building base pressure of 10^{-6} Pa would be necessary to assure that the up-to-air level would not exceed the MPC. The conclusions drawn from this analysis are (1) that bubble suits may have to be specified for routine maintenance, (2) that the plasma chamber can tolerate a pressure of 1.33 E-2 Pa in the reactor building if the leakage rate associated with this is $\leq$ 1.33 E-3 Pa$\cdot m^3$/s, and (3) that the allowable out leakage of DT from the torus to the reactor building is probably considerably less than 4 E-5 Pa$\cdot m^3$/s (3 E-4 torr$\cdot \ell$/s).

An analysis of the impact of the ETF vacuum boundary location from the tritium containment viewpoint was done. Alternate scenarios to the fuel recycle and purification system layout for ETF were developed to handle the different boundary locations. The boundaries considered were (1) a vacuum building containing either a welded torus or a mechanically-sealed torus, and (2) a sealed building with an inert atmosphere containing either a welded torus or a mechanically-sealed torus with a vacuum boundary at the TF coil. The major result was that any of the vacuum boundary locations could be handled from the tritium viewpoint with none having a clear decisive advantage.

The major impact of the use of a vacuum building would be the need for developing oil-less, doubly contained high vacuum and fare pumping equipment, and large separative gate valves to facilitate removal of pump assemblies. In the event of an accident, the on-line scrubbing system employed during normal operation would be bypassed to eliminate large impedances. An example of the type of pumping system for this scenario is shown in Fig. 3-9. In using a building with an inert atmosphere, no change would be needed in the basic ETF layout if the vacuum boundary was a welded torus; however, tritium would probably be released each time access into the welded torus was required for maintenance. If the vacuum boundary were at the TF coil, the space between the mechanical-seal and the boundary could be swept with a low pressure D_2 gas stream which would reduce T_2 permeation into the boundary area. The exhaust gas could be handled by a conventional cryocondensation pumping system which would trap D_2,DT,DT in a regenerable form. A comparative assessment of the two cases is shown in Table 3-5.

The data base and requirements for ETF tritium handling technology have been reviewed. There are a number of features unique to ETF that will have a considerable impact upon tritium handling considerations. For the first time, a fusion reactor will have a complete, integrated fuel recycling system in which substantial quantities (up to 10 kg/yr) of tritium will be consumed. The reactor will be surrounded by a large evacuated enclosure having a heterogeneity of surfaces which could contain substantial amounts of sorbed tritium. The divertor collector will use liquid lithium and will require tritium

recovery rates that are in excess of those for a full-scale commercial fusion reactor blanket. The first wall and blanket will be water-cooled (probably D_2O) and there is the potential for excessive ingress of tritium into the coolant. Components exposed to the plasma chamber will experience a significant flux of 14 MeV neutrons along with continuous tritium infiltration. In order to test the viability of various blanket concepts, full-scale blanket modules will be tested. These features require significant advances in the state of tritium technology.

References

1. C. D. Boley, "Fusion Power Program Quarterly Progress Report," January-March, 1979, Argonne National Laboratory, ANL/FPP-79-2, (1979).

2. S. Tamor and A. Engebretson, Science Applications, Inc., LAPS-9, SAI-75-6101J (1975); S. Tamor, Science Applications, Inc., LAPS-21, SAI-76-773LJ (1976).

3. B. A. Trubnikov, in Reviews of Plasma Physics, edited by M. A. Leontovich (Consultanta Bureau, N.Y., 1979), Vol. VII, p. 345.

4. C. C. Baker, *et al.*, "The Impact of Alternate Fusion Fuels on Fusion Reactor Technology," Argonne National Laboratory, ANL/FPP/TM-128, (1979).

5. C. D. Boley, Bull. Am. Phys. Soc. 24, 939 (1979).

4.0 FUSION ENERGY APPLICATIONS

4.1 Development of Fusion Energy for Alternate Applications

J. F. de Paz, Y. Gohar, H. S. Schreyer, H. C. Stevens, Fusion Power Program

Work continuing in the thermal-hydraulic analysis of a high-temperature falling bed blanket for the generation of process heat. In addition, the structural analysis of the blanket, an experimental program, and the neutronics study of the implications of using a D-D driver in these alternate applications were initiated.

The previous program report showed the advantage of adjusting the pebble velocity distribution to the internal heat generation rate in terms of reduced temperatures and lower heat losses by conduction and radiation through the composite liner-shield-steel panel walls. Two additional heat loss mechanisms have now been analyzed: free convection currents inside the gap, and heat lost to the stand-off spacers, which must be actively cooled. General simplifying assumptions were adopted in the calculations, but these seemed justified in view of the small heat flows that were found. Thus, assuming the gap to be bounded by surfaces at constant temperatures, and choosing conservative values for those temperatures, the resulting values of Grashof number were less than 500, indicating that the free convection heat transfer would be much smaller than the heat conduction. The presence of intense heat radiation effects would make free convection even less important.

The heat loss to the coolant circulating through the stand-off spacers was computed using the THTB code. Calculations were performed at three different axial positions and the average total losses computed from these. The spacers were approximated by straps of rectangular cross-section with one face taken to have a temperature determined by the coolant conditions, the opposite face assumed to be in contact with the liner through a 0.01 cm gap, and the other two faces exchanging heat by radiation with the ceramic liner and the radiation shield. The maximum strap temperature, occuring at its contact with the liner, was kept below 740°C by adjusting the coolant conditions. The THTB runs yielded a temperature distribution in the strap and liner, and from this the heat losses were calculated as approximately 1% of the power deposited in the pebble bed. This result indicates the feasibility of the cooled spacer concept.

As part of an experimental program to support and verify the analysis, tests are being devised to study the behavior of a falling pebble bed under static and dynamic conditions. These include the measuring of characteristics of the material (such as angle of repose and friction), observation of velocity profiles, mass flow measurements, and pressure loads on the containing walls.

The structural analysis is addressing the problems associated with the mechanical behavior of both ceramic components and metal structure; buckling calculations have been performed that leave yielded minimum values for the ceramic liner thickness that ensure avoidance of buckling conditions.

The possibility of using a D-D driver is being considered; the calculations show the advantage of this driver in terms of maximizing the amount of power released as high temperature heat and lessening the problems associated with the induced activity of the material. Also, a higher power density is obtained with this driver; this is expected to result in more favorable conditions for removal of the heat with a falling bed blanket.

5.0 ENVIRONMENT AND SAFETY

5.1 Fusion Reactor Safety Studies

5.1.1 Studies of Air-Detritiation Operations

R. H. Land and V. A. Maroni, Chemical Engineering Division, and
M. Minkoff, Applied Mathematics Division

Work on the modified version of TSOAK (supported during FY 1979 by a contract with EG&G, Idaho) is now essentially complete. During the second half of 1979, the modified code (TSOAK-M1) was run against previously obtained enclosure detritiation data with quite good results.[1] Six out of eight data sets gave convergence to a reasonable set of reaction/adsorption/release parameters (see Fig. 5-1). The relative differences in value for each parameter from one data set to another are consistent with expectations based on differing experimental conditions. For example, referring to Fig. 5-1, the enclosure tests run by flushing moist, tritium free, room air through the enclosure resulted in higher reaction rate parameters, but lower adsorption and release rate parameters than obtained for enclosure tests done using a closed cycle detritiation unit based on conversion of molecular tritium to HTO followed by molecular sieve drying. The higher average relative humidity in the enclosure during the once through flushing tests is believed to account for the observed variations in parameter values when compared to the closed cycle detritiation tests. The significance of the differences in the instrument correction factors is not clear at this time.

The principal conclusions and recommendations drawn from this study may be summarized as follows: (1) The simplified reaction/adsorption/release model[1] employed in TSOAK-M1 appears to be capable of predicting the observations of experimental detritiation tests, but should be subjected to further examination using results from large enclosures and, if possible, from actual facility buildings. Only through extend utilization for a wide range of test conditions will it be possible to validate the credibility of the model. (2) Pseudo-second-order reaction-rate parameters (for $T_2 + H_2O \rightleftarrows HTO + HT$) derived from previous small cubicle detritiation experiments conducted at ANL are considerably greater (10^3 to 10^7 times) than comparable parameters derived from isostatic kinetics studies done in well-characterized glass bulbs. This is believed to be related, more than anything else, to the heterogeneity of surface conditions in typical enclosures and the convective environments that result from recycling of the enclosure atmosphere. (3) The projected consequences of the effects incorporated in the TSOAK-M1 model, when extropolated to anticipated fusion reactor facilities, seem to be less serious[1] than was previously suggested, at least to the extent that parameter values from the ANL cubicle experiments are close to being representative of conditions in such facilities.

References

1. R. H. Land, V. A. Maroni and M. Miwkoff, "TSOAK-M1: A Computer Code to Determine Tritium Reaction/Adsorption/Release Parameters from Experimental Air Detritiation Tests," Argonne National Laboratory Report ANL-79-84 (1979).

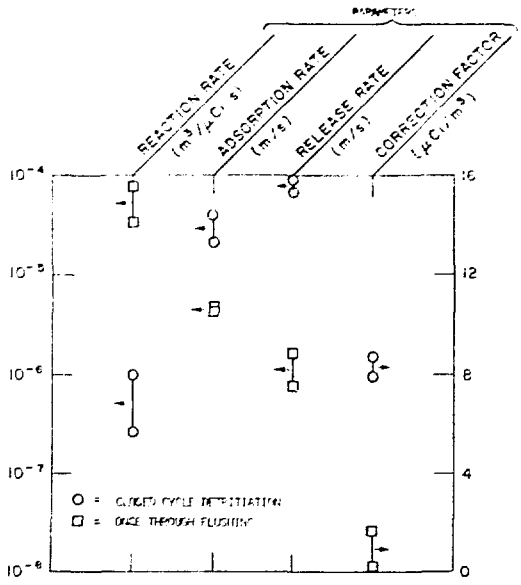

Figure 5-1. TSOAK-M1 analysis of duplicate detritiation test data sets obtained with the 0.050 m^3 enclosure at ANL.

6.0 MAGNETIC SYSTEMS

6.1 Energy Storage and Transfer

R. Fuja, Accelerator Research Facilities Division

The switched resistors mentioned in the last quarterly report were installed. The resistor circuits were placed across the two coils of the ICB and wired to the microprocessor for control. A resistor is switched across a coil when the current in the coil falls below 1.5 amperes, otherwise it is switched out of the circuit. This modification caused the energy transfer efficiency to increase from 81% to 91%.

The two parameters available for controlling the rate of energy transfer through the IBC are phase angle and frequency. All the previous experiments concerned themselves with phase angle control. Frequency control of the ICB is more complicated than phase angle control. However, a combination of both methods of control are needed to transfer energy. The amount the frequency can be made to vary, during a transfer cycle, is dependent on the operating phase angle and the ratio of the current in the coils. These limitations can be overcome by decreasing the response time of the control system.

The circuits required to change frequency during ICB operation are being built and will be installed before the end of the year. An operating scenario for the control of the ICB using frequency and phase control has to be developed and programmed for the microprocessor. The system should be ready for testing during January 1980.

References

1. R. Fuja, R. Kustom and M. Ehsani, "Three Phase Energy Transfer Circuit with Superconducting Energy Transfer Coils," Conference Report IAS-IEEE (1979).

2. R. Fuja, "Conceptual Design of a Superconductive Energy and Transfer System for a Commercial Tokamak EF Coil, International Symposium on Superconducting Energy Storage and Transfer," Osaka, Japan (October 1979).

3. M. Ehsani, R. Kustom and R. Fuja, "General Phase-Frequency Shift in a Multiphase Inductor Converter Bridge," 8th Symposium on Engineering Problems of Fusion Research, San Francisco, California (November 1979).

7.0 APPLIED PLASMA PHYSICS

7.1 Atomic Theory

7.1.1 The Bethe Cross Sections for the Ionization of Li-Like Ions by Electron Impact

K. Cheng and Y-K. Kim, Radiological and Environmental Research Division

The Bethe cross section for an excitation to a discrete state $|n\rangle$ is given by

$$\sigma_n = 4\pi a_0^2 R/T \; [A_n \ln(T/R) + B_n + C_n \, R/T], \tag{1}$$

where $a_0 = 0.529$ Å, $R = 13.6$ eV, T = incident electron energy, and A_n, B_n, and C_n are Bethe parameters derived from the properties of the target atom. We list in Table 7-1 the values of the Bethe parameters for a few excited states, calculated from the Hartree-Fock wavefunctions. A sum rule exists for the Bethe cross sections (including continuum transitions):

$$\sigma_t = \sum_{\text{all } n} \sigma_n = 4\pi a_0^2 R/T \; [A_t \ln(T/R) + B_t + C_t \, R/T] \; . \tag{2}$$

The sum of discrete excitations only,

$$\sigma_d = \sum \text{(discrete n only)} \; \sigma_n = 4\pi a_0^2 R/T \; [A_d \ln(T/R) + B_d + C_d \, R/T] \tag{3}$$

can be calculated by summing the Bethe parameters in Eq. (1) for all discrete excited states (including forbidden transitions). The difference between σ_t and σ_d is the ionization cross section, σ_i:

$$\sigma_i = 4\pi a_0^2 R/T \; [A_i \ln(T/R) + B_i + C_i \, R/T] \; . \tag{4}$$

The Mott exchange correction is given by[1]

$$\sigma_x = 4\pi a_0^2 R^2/T^2 \sum_j [\ln(I_j/T) + 1] \, N_j \; , \tag{5}$$

where I_j and N_j are the ionization potential and occupation number, respectively, of the jth orbital. In Table 7-2, we list the Bethe parameters for σ_t, σ_d, σ_i, and I_j.

Table 7-1. Bethe Parameters for Discrete Transitions of Li-Like Ions

Ion	2s-2p	2s-3p	2s-4p	2s-3s	2s-3d
C^{3+}					
A_n	0.493	0.0684	0.0162	0	0
B_n	1.27	-0.135	-0.0310	0.0604	0.158
C_n	0.124	0.179	0.027	-0.103	-0.266
N^{4+}					
A_n	0.323	0.00540	0.0121	0	0
B_n	0.820	-0.126	-0.0275	0.0408	0.110
C_n	-0.105	0.192	0.0210	-0.105	-0.273
O^{5+}					
A_n	0.228	0.0431	0.0093	0	0
B_n	0.574	-0.114	-0.0239	0.0294	0.0817
C_n	-0.091	0.201	0.0189	-0.107	-0.278

Table 7-2. Bethe Parameters for Li-Like Ions

Ion	A	B	C	I_{1s}(Ry)	I_{2s}(Ry)
C^{3+}					
σ_t	0.701	1.422	-5.30	--	--
σ_d	0.594	1.387	-0.369	--	--
σ_i	0.107	0.035	-4.93	--	--
σ_x	--	--	--	26.96	4.730
N^{4+}					
σ_t	0.476	0.838	-5.30	--	--
σ_d	0.401	0.857	-0.349	--	--
σ_i	0.075	-0.019	-4.95	-	--
σ_x	--	--	--	38.31	7.[illegible]2
O^{5+}					
σ_t	0.345	0.541	-5.30	--	--
σ_d	0.290	0.572	-0.335	--	--
σ_i	0.055	-0.031	-4.97	--	--
σ_x	--	--	--	51.[illegible]	10.13

In Figs. 7-1 through 7-3, we compare our theoretical result[2] with a recent experimental and theoretical data.[3-5] The Fano plot (σT vs ln T) used in Figs. 7-1 through 7-3 emphasizes the high-energy region and is a powerful tool to elucidate asymptotic trends. It is clear from Fig. 7-3, for instance, that the last three experimental data do not show expected asymptotic shape. It is more difficult by our method to determine the heights of the curves than the slopes. Further theoretical work is in progress to obtain more reliable heights. The kinks in the experimental data signify the onset of the ionization of K electrons.

The sum rule method has the advantage that the excitation and ionization of K electrons are automatically included, whereas conventional theories,[4,5] require separate calculation for each possible mode of ionization. Our results were presented at an international conference.[2]

7.1.2 Transitions Between Low-Lying States of the First-Row Atoms

Computer codes to calculate all E1, E2, and M1 transition probabilities among L-shell excited states ($2s^j 2p^k$) of isoelectronic sequences of the first-row atoms (Li through F) have been completed. Production runs will be made for a large number of ions in the sequences as soon as sample results are tested against known experimental and theoretical data for reliability. This will complete the first phase of our project, i.e., calculation of all spectroscopic data for simple electronic configurations. Simple adaptations will also allow us to calculate spectra for the isoelectronic sequences of the second-row atoms (Ne through Cl) in the near future.

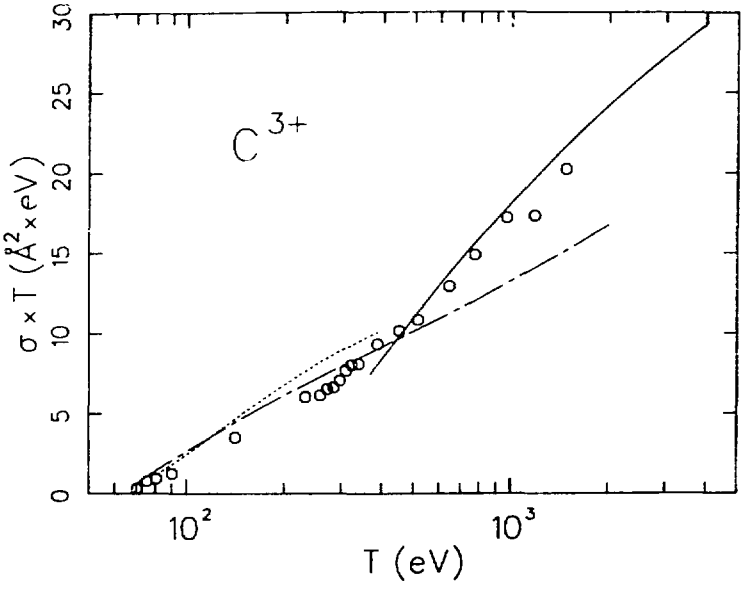

Figure 7-1. Fano plot for the ionization of C^{3+} by electron impact. T is the incident energy and σ is the cross section. Solid curve represents the present work, the circles are the experimental data from Ref. 3, dotted and dot-dashed curves stand for theoretical results from Refs. 4 and 5, respectively.

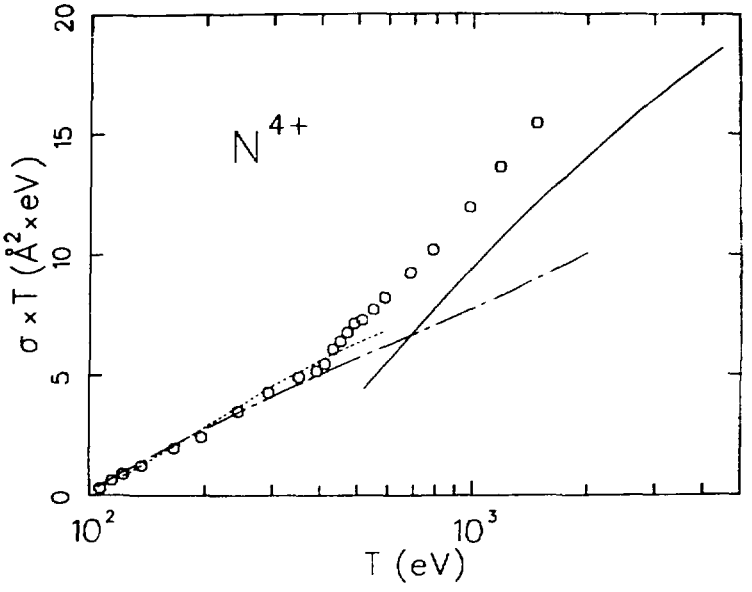

Figure 7-2. Fano plot for ionization of N^{4+} by electron impact. T is the incident energy and σ is the cross section. Solid curve represents the present work, the squares are the experimental data from Ref. 3, dotted and dot-dashed curves stand for theoretical results from Refs. 4 and 5, respectively.

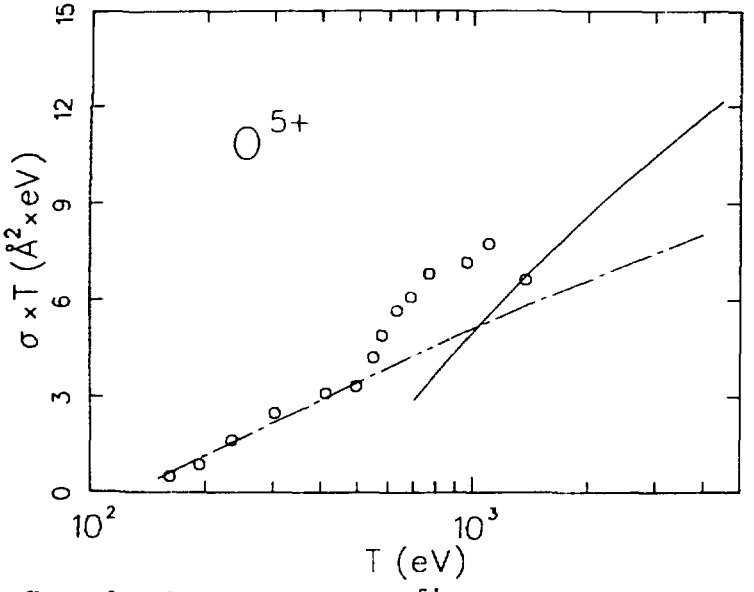

Figure 7-3. Fano plot for ionization of O^{5+} by electron impact. T is the incident energy and σ is the cross section. Solid curve represents the present work, the squares are the experimental data from Ref. 3, dotted and dot-dashed curves stand for theoretical results from Refs. 4 and 5, respectively.

References

1. Y.-K. Kim and M. Inokuti, Phys. Rev. A 3, 665 (1971).

2. Y.-K. Kim and K. T. Cheng, Abstracts of the YIth International Conference on the Physics of Electronic and Atomic Collisions (Kyoto, Japan, August 28 - September 3, 1979), p. 218.

3. D. H. Crandall, R. H. Phaneuf, B. E. Hasselquist, and D. C. Gregory, J. Phys. B 12, L249 (1979).

4. D. L. Moores, J. Phys. B 11, L1 (1978).

5. L. B. Golden and D. H. Sampson, J. Phys. B10, 2229 (1977).

FPP AND FPP-RELATED DOCUMENTS AUTHORED BY ARGONNE PERSONNEL

G. AYRAULT

"Microstructure of Single-and Dual-Ion Irradiated V-15Cr-5Ti"
J. Met. Vol. 31 p. F49 (1979).

"Precipitation in Single-and Dual-Ion Irradiated Ti-6Al-4V"
J. Met. Vol. 31 p. F60 (1979).

C. D. BOLEY, E. M. GELBARD AND S. P. HIRSHMAN

"Neoclassical Transport in Plasmas Containing Ions with Multiple Charge States"
Physics of Fluids 22, 1280 (1979).

KOSTA BURBA

"Cost Algorithms and Estimating Data",
Argonne National Laboratory, ANL/FPP/TM-123 (May, 1979).

K. T. CHENG & T.-K. KIM

"Energy Levels, Wavelengths, and Transition Probabilities of Cu-Like Ions"
Atom. Data Nucl. Data Tables 22, 1280 (1979).

S. K. DAS, M. KAMINSKY, R. TISHLER AND J. CECCHI

"Surface Damage and Sputtering of ATJ Graphite as Candidate Armor Plate Material for TFTR Under D^+ Bombardment"
Accepted for publication in *Jour. of Nucl. Mater.* (1979).

G. FENSKE, S. K. DAS, M. KAMINSKY AND G. H. MILEY

"The Effect of Dose on the Evolution of Cavities in 500-keV $^4He^+$-Ion Irradiated Nickel"
Accepted for publication in *Jour. of Nucl. Mater.* (1979).

L. R. GREENWOOD, R. R. HEINRICH, M. J. SALTMARSH AND C. B. FULMER

"Integral Tests of Neutron Activation Cross Sections in a $^9Be(d,n)$ Field at E_d = 40 MeV"
Nuclear Science and Engineering, 72, 175 (1979).

D. M. GRUEN, S. VEPREK AND R. B. WRIGHT

"Plasm-Materials Interactions and Impurity Control in Magnetically-Confined Thermonuclear Fusion Machines"
Topics in Current Chemistry 8, (1979).

S. HARKNESS

"Fusion Energy for Alternate Applications: Development of a High Temperature Blanket for Synthetic Fuel Production"
Argonne National Laboratory, ANL/FPP/TM-117 (1979).

JUNGCHUNG JUNG
"Theory and Use of the Radioactivity Code RACC" (code manual)
Argonne National Laboratory, ANL/FPP/TM-122 (May, 1979).

T.-K. KIM & K. T. CHENG
"Beth Cross Sections for Ionization of C^{3+}, N^{4+}, and O^{5+}"
Abstracts of XIth Int. Conf. on the Physics of Electronic & Atomic Collisions August 28-September 3, 1979, Kyoto, Japan, pp. 218-219.

M. A. KIRK AND L. R. GREENWOOD
"Determination of the Fast Neutron Flux and Energy Spectrum in the Low-Temperature Fast-Neutron Facility in CP-5"
J. Nucl. Mat. 80, 159 (1979).

A. R. KRAUSS & D. M. GRUEN
"Secondary Ion Emission from Clean and Oxygen-Covered Beryllium Surfaces-II: Energy Dependence"
Surface Science (in press).

A. R. KRAUSS AND R. B. WRIGHT
"Energy and Mass Distributions of Sputtered Particles"
J. Nucl. Mat. (December 1979).

V. A. MARONI
"Control of Tritium Permeation Through Fusion Reactor Structural Materials"
Proc. U.S. DOE Environmental Control Symposium, U.S. DOE Report DOE/EV-0046 (1979) Vol. 2, pp. 39-52 (1979).

V. A. MARONI AND E. H. VAN DEVENTER
"Materials Considerations in Tritium Handling Systems"
J. Nucl. Mater. 85 & 86, 257 (1979).

F. V. NOLFI AND A. P. L. TURNER
"Effects of Irradiation on Fusion Reactor Materials"
Damage Analysis and Fundamental Studies Quarterly Progress Reports. (January-March 1979 and April -June 1979).
U. S. DOE Report (1979).

F. V. NOLFI AND G. AYRAULT
"Microstructural Evolution During Dual-Ion Irradiation of Candidate Fusion Reactor Materials"
Presented at Intl. Conf. on Irradiation Behavior of Metallic Materials for Fast Reactor Core Components, Ajaccio, Corsica, France, (June 5-7, 1979).

F. V. NOLFI, R. O. SCATTERGOOD AND A. P. L. TURNER
"Stress and Irradiation Induced Mass Transport"
Scripta Met. Vol. 13 pp. 231-236 (1979).

"Stress and Irradiation Induced Mass Transport"
J. Met. Vol. 31 p. F-31 (1979).

F. V. NOLFI AND R. E. GOLD
"Vanadium Alloys and Their Application to Fusion Reactor Development"
J. Met. Vol. 31 p. F-49 (1979).

LARRY TURNER
"Safety of Fusion Magnets: Twelve Problem Areas,"
Argonne National Laboratory, ANL/FPP/TM-121 (April, 1979).

R. B. WRIGHT AND D. M. GRUEN
"Discussion of the Origin of Secondary Photon and Secondary Ion Emission During Energetic Particle Irradiation of Solids: I. The Collison Cascade"
J. Chem. Phys. (December 1979).

"Secondary Photon Emission Studies of Ion Bombardment Beryllium"
Proc. VIII Int. Conf. Atomic Collisions in Solids, Hamilton, Ontario, (August 1970).

R. B. WRIGHT, M. J. PELLIN, D. M. GRUEN AND C. E. YOUNG
"Laser Fluorescence Spectroscopy of Sputtered Uranium Atoms"
Ibid.